ELECTRON-POSITRON PAIR-PRODUCTION AND NEUTRINO ENERGY-LOSS FROM THE INSTABILITY REGIONS OF VERY-MASSIVE STARS

LURWAN GARBA GAYA

FACULTY OF SCIENCE
UNIVERSITY OF MALAYA
KUALA LUMPUR

2019

ELECTRON-POSITRON PAIR-PRODUCTION AND NEUTRINO ENERGY-LOSS FROM THE INSTABILITY REGIONS OF VERY-MASSIVE STARS

LURWAN GARBA GAYA

THESIS SUBMITTED IN FULFILMENT OF THE REQUIREMENTS FOR THE DEGREE OF DOCTOR OF PHILOSOPHY

DEPARTMENT OF PHYSICS
FACULTY OF SCIENCE
UNIVERSITY OF MALAYA
KUALA LUMPUR

2019

UNIVERSITY OF MALAYA

ORIGINAL LITERARY WORK DECLARATION

Name of Candidate**: LURWAN GARBA GAYA**

Matric No: **SHC140036**

Name of Degree: **DOCTOR OF PHILOSOPHY**

Title of Thesis: **ELECTRON-POSITRON PAIR-PRODUCTION AND NEUTRINO ENERGY-LOSS FROM THE INSTABILITY REGIONS OF VERY-MASSIVE STARS**

Field of Study: **THEORETICAL PHYSICS**

I do solemnly and sincerely declare that:

(1) I am the sole author/writer of this Work;
(2) This Work is original;
(3) Any use of any work in which copyright exists was done by way of fair dealing and for permitted purposes and any excerpt or extract from, or reference to or reproduction of any copyright work has been disclosed expressly and sufficiently and the title of the Work and its authorship have been acknowledged in this Work;
(4) I do not have any actual knowledge nor do I ought reasonably to know that the making of this work constitutes an infringement of any copyright work;
(5) I hereby assign all and every rights in the copyright to this Work to the University of Malaya ("UM"), who henceforth shall be owner of the copyright in this Work and that any reproduction or use in any form or by any means whatsoever is prohibited without the written consent of UM having been first had and obtained;
(6) I am fully aware that if in the course of making this Work I have infringed any copyright whether intentionally or otherwise, I may be subject to legal action or any other action as may be determined by UM.

Candidate's Signature   Date:

Subscribed and solemnly declared before,

Witness's Signature   Date:

Name:

Designation:

ELECTRON-POSITRON PAIR-PRODUCTION AND NEUTRINO ENERGY-LOSS FROM THE INSTABILITY REGIONS OF VERY-MASSIVE STARS

ABSTRACT

Understanding the end fates of very-massive stars has been very exciting and essential in Astrophysics. Electron-positron pairs and neutrinos are very critical on this important astrophysical process. Neutrinos are produced in large numbers from exploding massive stars and are extremely important probes of processes involve in supernovae before its explosion. In spite of tremendous developments recorded in recent times, state-of-the-art stellar evolution models would provide many information about instability of very-massive stars arising from eminent production of electron-positron pairs. The ambient photons in the interior of very-massive stars are sufficiently energetic to create electron-positron pairs just before ignition of any element heavier than oxygen during evolution of the stars. Realising importance of pair-production and neutrino energy-loss in determining end fates of very-massive stars, this work investigate adiabatic effects of pair-production on dynamical instability of very-massive stars with carbon-oxygen cores, within the range of 60 $M_{\odot} < M_{CO} < 133\ M_{\odot}$. Thermal energy, pressure, and entropy of pair-production from instability regions of these stars are also evaluated. Models with rotation in Small Magellanic Cloud (SMC) as well as those with and without rotation in Large Magellanic Cloud (LMC) are considered. Similarly, pair-neutrino emission which is the dominant cooling process in the instability regions of these stars is computed. On the other hand, the neutrino energy-loss through thermal processes is calculated from stellar models of 120, 150, 200, 300, 500 $M_{\odot}$, with rotation and 120, 150 and 500 $M_{\odot}$ without rotation at LMC with metallicity $Z = 0.006$. The results of this work showed that adiabatic index of pair-productions, which create disturbance in the instability region, is fundamentally positive with central temperature and density for all models under consideration. The non-rotating model may not be suitable for inducing instability due to large mass-loss. On the other hand, effects of rotation to reduce mass of oxygen core has increased the thermal energy of pairs within the threshold of instability regions, and non-rotating model in LMC has low electron-positron thermal energy, which almost die before reaching the region. In rotating models, electron-positron pairs are annihilated and rate of pair neutrino energy-loss increases within the instability region. The neutrino energy-loss in the instability regions will continue to increase until density rises when the neutrino emission began to decline. The thermal energy of electron-positron pairs and neutrino energy-loss are fundamentally responsible to overcome contraction of massive star and cool its core. The significance of these results on the end fates of very-massive stars, especially on stars' explosion as Pair-Instability Supernova (PISN), is discussed and most of the results showed reasonable agreement with existing predictions. This study would help in improving the literature for better understanding of end fates of very-massive stars.

Keywords: energy-loss, instabilities, neutrinos, pair-production, very-massive stars

PENGELUARAN PASANGAN ELEKTRON-POSITRON DAN KEHILANGAN TENAGA NEUTRINO DARIPADA KAWASAN KETIDAKSTABILAN BINTANG-BINTANG BERJISIM BESAR

ABSTRAK

Model evolusi cemeelang bintang-bintang nenek moyank yang sangat besar memberikan maklumat kualitatif tentang ketidakstabilan bintang-bintang. Pada suhu yang sangat tinggi dan ketumpatan rendah; pengeluaran pasangan di pusat bintang besar membawa indeks adiabatik di bawah 4/3. Penghasilan pasangan dan neutrino yang unik dari kawasan ketidakstabilan bintang bermetaliti yang sangat besar dipercayai pada dasarnya mencetuskan nasib akhir mereka sama ada Pair-Ketidakstabilan Supernova (PISN) atau sebaliknya. Kerja ini menyiasat kesan adiabatik pasangan elektron-positron pada ketidakstabilan dinamik bintang-bintang yang sangat besar dengan teras karbon-oksigen, dalam lingkungan 60 $M_\odot < M_{CO} < 133\ M_\odot$, untuk model berputar dan tidak berputar. Tenaga terma elektron-positron, tekanan dan entropi dari kawasan ketidakstabilan bintang-bintang ini juga dinilai. Kedua-dua objektif ini dicapai dengan membina satu model ke dalam persamaan elektron-positron termodinamik (Helmholtz EoS) jadual persamaan. Di bahagian terakhir kerja ini, kehilangan tenaga neutrino dari bintang-bintang yang sangat besar itu dikira. Pelepasan pasangan-neutrino menguasai proses penyejukan di kawasan ketidakstabilan bintang-bintang. Kehilangan tenaga neutrino dikira melalui model yang dibina ke dalam kod SNEUT4. Adalah diperhatikan bahawa indeks adiabatik yang menimbulkan gangguan di kawasan pasangan-pengeluaran pada dasarnya positif dengan suhu dan ketumpatan pusat untuk semua model yang dipertimbangkan. Begitu juga, dalam model berputar; jisim teras oksigen dalam rantau ketidakstabilan telah mempercepatkan indeks adiabatik untuk memampatkan bintang, manakala untuk model tidak berputar dengan cepat mengurangkan indeks adiabatik. Pengurangan kehilangan jisim dalam model berputar juga mengurangkan jumlah haba di rantau ini dan hanya haba kecil, yang bebas dari kelimpahan kimia, diperlukan untuk meningkatkan suhu pusat untuk letupan atau keruntuhan bintang besar-besaran. Dinamik kebanyakan kuantiti adiabatik menunjukkan corak yang sama untuk semua model berputar. Model tidak berputar mungkin tidak sesuai untuk mendorong ketidakstabilan disebabkan oleh kehilangan jisim yang tinggi ke haba. Sebaliknya, kesan putaran untuk mengurangkan jisim teras oksigen akan meningkatkan tenaga haba pasangan dalam ambang kawasan ketidakstabilan, dan model tidak berputar dalam Large Magellanic Cloud (LMC) mempunyai haba elektron-positron rendah tenaga dan hampir mati sebelum sampai ke kawasan ketidakstabilan. Dalam model berputar, pasangan elektron-positron dihapuskan dan kehilangan tenaga neutrino meningkat di dalam kawasan ketidakstabilan. Peningkatan dalam kehilangan tenaga neutrino ini berterusan sehingga ketumpatan meningkat apabila pelepasan neutrino pasangan mula menurun. Tenaga terma pasangan elektron-positron dan kehilangan tenaga neutrino diperlukan untuk mengatasi penguncupan bintang besar dan menyejukkan teras masing-masing. Kesan adiabatik yang dinilai dari pengeluaran elektron-positron-pasangan pada ketidakstabilan dinamik bintang-bintang ini, dan tenaga termal, tekanan dan entropi berpasangan yang dihasilkan, serta pasangan tenaga neutrino yang dihasilkan dari bintang-bintang ini akan membantu lebih baik pemahaman mengenai nasib akhir bintang-bintang yang sangat besar.

Kata kunci: persamaan keadaan, ketidakstabilan, neutrinos, pasangan-pengeluaran, bintang-bintang berjisim besar

ACKNOWLEDGEMENT

I begin in the name of Allaah, the beneficent, the merciful. Peace and blessings of Allaah be upon Prophet Muhammad ﷺ, his households, and companions. I thank Allaah; the creator of stars and universe, for sparing my life to witness this milestone achievement.

I would like to thank my supervisors Prof. Dr. Hasan A. Kassim and Dr. Norhasliza Yusof, for their continuous support of my PhD. study. Their guidance helped me in time of the research and writing of this thesis. Their keen support in carrying out this research is acknowledged.

I am indebted to my parents Alhaji Garba Tafida and Hajiya Rabi Swaleh, for their moral upbringing, prayers, and exceptional parental care throughout my lifetime. I thank them and pray that Allaah give them more health and wisdom in their lifetime. My sincere gratitude also goes to my lovely wife; Hafsat Isa Yahya, for her unconditional love, prayers and for taking care of our children in my absence. Let me also appreciate my handsome children; Ahmed Ridwan and Abubakar Ridwan. I am equally thankful to my brothers, sisters and entire members of my family and friends, who assisted me in one way or the other during the time of carrying out this research.

Members of Theoretical Physics Lab. have contributed to my personal and professional time at University of Malaya (UM). The Lab. has been a source of friendships as well as good advice and collaborations. Special mention goes to Samer Kamal Issa Ali, Firas Abed Ahmed, and Nor Sofiah Ahmad. While Dr. Ahmed Rufa’i Usman and Dr. Isa Baba Koki are friends both in UM and home.

Finally, this work would not have been possible without support accorded me from Northwest University, Kano, Nigeria.

TABLE OF CONTENTS

LIST OF FIGURES

LIST OF TABLES

LIST OF SYMBOLS AND ABBREVIATIONS

L_S	:	Luminosity of a star
M_S	:	Mass of a star
$M_\odot$	:	Mass of the Sun
$L_\odot$	:	Solar luminosity
BB	:	Big Bang
BH	:	Black Hole
BSG	:	Blue Supergiant
C	:	Carbon
CCSN	:	Carbon-Core Supernova
CNO	:	Carbon-Nitrogen-Oxygen
EoS	:	Equation of State
G	:	Gravitational constant
He	:	Helium
Helm-EoS	:	Helmholtz Equation of State
HR	:	Hertzsprung-Russel
H	:	Hydrogen
ISM	:	Interstellar Medium
KeV	:	Kilo-electron Volt
LMC	:	Large Magellanic Cloud
LBV	:	Luminous Blue Variable
M_{CO}	:	Mass of Carbon-Oxygen core
MeV	:	Mega-electron Volt
Z	:	Metallicity
MW	:	Milky Way
Ne	:	Neon
NS	:	Neutron Star
N	:	Nitrogen
NACRE	:	Nuclear Astrophysics Compilation of Reaction Rates
NSE	;	Nuclear Statistical Equilibrium
O	:	Oxygen
PISN	:	Pair-Instability Supernova
PISNe	:	Pair-Instability Supernovae

PP	:	Proton-Proton
PPISN	:	Pulsational Pair-Instability Supernova
R_S	:	Radius of star
RS	:	Red Supergiant
Si	:	Silicon
SMC	:	Small Magellanic Cloud
SLSN	:	Super-Luminous Supernova
SN	:	Supernova
SNe	:	Supernovae
UV	:	Ultra-Violet
WR	:	Wolf-Rayet
ZAMS	:	Zero-age Main-Sequence

CHAPTER 1: INTRODUCTION

1.1 Introduction

The production of electron-positron pairs in the cores of massive stars at high temperature and relatively low density is vital in the evolution, collapse, death and end fates of not only massive stars but many Astrophysical objects, such as in mass-loss from black hole mergers (Belczynski et al., 2016) and in some models of the Universe which predicted that first stars at Dark Ages might form massive stars and become subject to pair-instability (Abel et al., 1998; Abel et al., 2000; Bromm et al., 2002; Bromm & Larson, 2004; Chatzopoulos & Wheeler, 2012a). Very-massive stars that have carbon-oxygen core within the range of 60 $M_\odot < M_{CO} < 133\ M_\odot$ are expected to end their lives as either PISN or other type of supernova. This is achieved through production of electron-positron pairs and neutrino emission from their instability regions. It is fascinating to say that most of the heavier elements in human bodies were created in thermonuclear burning of massive stars. During the lifetime of a star, starting from hydrogen gas until it reached a point in its evolution, at about 10^7 years, an iron core is evolve, which begin to collapse in seconds time scale, such that the gravitational energy released ignites an enormous explosion and the overlying layers explode very quickly and completely. The importance of massive stars cannot be over quantified because they are very fundamental to sequence of processes after Big Bang (BB) which as a result, life become possible on Earth. The immense abundance of heavy elements and Ultra-Violet (UV) radiation are principally originated from massive stars. Through supernova explosions, massive stars provide a significant source of energy balance and turbulence in Interstellar Medium (ISM) of galaxies (Yorke, 2004). In Milky Way galaxy (our galaxy), for example, stars ranges in mass from hundredth mass of the Sun to about a thousand solar masses. The least massive stars have lifetimes as long as age of the

Universe: which is tens of billions of years, after which they slowly fade to become cold cinders. Whereas, very massive stars have lifetimes of only a few million, to tens of millions of years, after which they catastrophically explode as supernova. Despite prominent and outstanding contribution of these relatively short-lived stars to properties and evolution of galaxies, our understanding of their evolution and final fate is still not complete. This is because they are low in number and are theoretically very complex to deal with. And therefore, improving our understanding of massive stars is crucial for addressing fundamental questions such as:

I. Since the first stars were massive of about ~30 - 300 $M_{\odot}$ and contribute to re-ionization in interstellar medium, a question comes; when did first stars in the Universe forms and how did they influence their environments?

II. The massive stars produced most cosmic elements like Oxygen O, Carbon C, Iron Fe, Calcium Ca etcetera, as such, we need to know the cosmic origins of all chemical elements, especially those fundamental to life on earth?

III. How the exchanges of mass and momentum between massive stars and environment configured the origin and evolution of galaxies?

In evolution of very-massive stars; pressure-supporting photons are converted into electron-positron pairs before ignition of oxygen, which leads to violent contraction that induces a catastrophic nuclear explosion (Barkat et al., 1967; Heger & Woosley, 2002; Rakavy & Shaviv, 1967). As a result of the explosion, energies are emitted, which completely unbind the star in pair-instability supernova without any remnant (Gal-Yam et al., 2009). The central cores of these stars become dynamically unstable as a result of production of electron-positron pairs which occur immediately after the central carbon burning (Fraley, 1968; Rakavy & Shaviv, 1967; Rakavy et al., 1967). When pairs of free electrons and positrons are produced during a high energy photons' collision with atomic nuclei in a massive star, the internal pressure of the massive star, which supports against its gravitational collapse, reduces temporarily and leads to its partial collapse. The energy absorbed in creating the rest mass of electron-positron pairs also reduce the value of adiabatic index at low densities. However, this energy become significantly less at high temperature, while, pair density increases at low temperature (Fraley, 1968). The pair-production instability resembles ionization since a fraction of energy is spent not to increase the temperature, but to create pairs. The result should be development of dynamical instability and consequent implosion because the pressure gradient is not able to compensate the gravitational attraction. The dynamical collapse of oxygen core occurs if large fraction of the core enter the instability region, and according to (Kippenhahn et al., 1990), 40% of the star mass will enter the instability region in the density-temperature-diagram. Thus, the fundamental property for this region of instability in the star evolution is the oxygen-core mass.

1.2 Problem Statement

Inside cores of massive stars, the absorption of energy to create rest mass of electron-positron pairs lowers the adiabatic index to below 4/3, at low densities. The pair-production and neutrino cooling are paramount in determining end fates of these stars. Figure 1.1, showed the instability region in which pairs are produced and adiabatic index is less than 4/3. In this region, number of pairs decreases exponentially at low temperature. At high temperature, the energy absorbed in creating rest mass become less significant. This shows that the boundary of the unstable area where adiabatic index is below 4/3 reached a maximum density of about $7x10^5$ g/cm^3 at a temperature of about $2.85x10^9$ K. This instability will basically trigger the end fate of the star involved. Even though the fundamental mechanisms involved in the end fates of very-massive stars is still not fully understood (Kotake et al., 2006), owing to insufficient information pertaining to; how a star attains a state of explosion (Wright et al., 2017), at what mass a stellar progenitor encounter the instability regime and its corresponding zero-age main sequence (ZAMS) mass (Woosley, 2017). Similarly, the metallicity at which a stellar progenitor explode as PISN is still under debate (Langer et al., 2007). The current understanding of physics responsible for these exotic processes have drawn the attention of many researchers in astrophysics community.

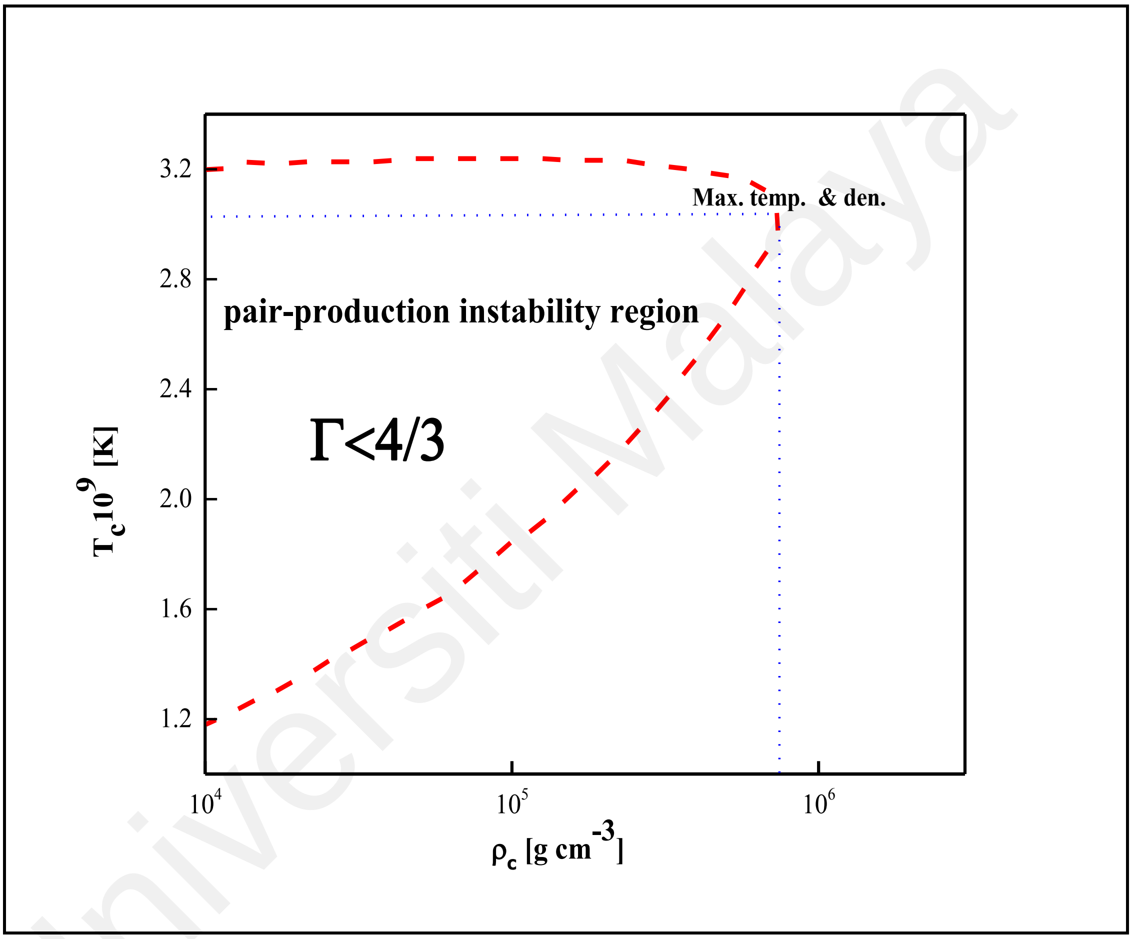

Figure 1.1: The electron-positron pair-instability region. Adiabatic index is below 4/3 only within this unstable area (the red-dashed area) at maximum central density and temperature of about 7×10^5 g cm^{-3} and 2.85×10^9 K respectively.

In recent times, many authors have computed realistic light curves for PISNe models at very near-solar metallicities (Kasen et al., 2011; Kozyreva et al., 2016; Whalen et al., 2013; Whalen et al., 2014a; Whalen et al., 2014b), and most of these studies have discovered that the luminosity of already observed super-luminous supernovae can be compared to maximum luminosity in their models. Certainly, this might be true, because a few of detected super-luminous supernovae are considered to originate from PISN (Cooke et al., 2012; Gal-Yam et al., 2009; Lunnan et al., 2016; Smith et al., 2007), due to production of substantial amounts of radioactive nuclei in them (Wright et al., 2017). Therefore, the prevalent models of very-massive stellar evolutions would provide qualitative information about this important astrophysical phenomenon. In 2013, Yusof et al. (2013), find that 150 $M_{\odot}$ and 200 $M_{\odot}$ rotating stellar progenitor models in SMC metallicities and 500 $M_{\odot}$ rotating and non-rotating models in LMC metallicities, are expected to undergo a gigantic explosions known as PISN. While those predictions were made based on estimate of carbon-oxygen core in the range of 60 $M_{\odot} < M_{CO} < 130$ $M_{\odot}$, they do not consider effects of electron-positron pair productions (at least in equation of state) and the dominant pair neutrino cooling from the instability regions of the stars involved. In massive stars, however, very energetic photons are converted into electron-positron pairs just before ignition of any element heavier than oxygen and the star will enter a region (Figure 1.1) in which the energy needed to create rest mass of electron-positron pairs (at high entropy) softens the equation of state and reduce adiabatic index to below 4/3 (Fraley, 1968). This will subsequently leads to a violent contraction that activates a nuclear explosion (Barkat et al., 1967; Bond et al., 1984; Carr et al., 1984; Chatzopoulos & Wheeler, 2012a; El Eid & Hilf, 1977; El Eid et al., 1983; Fraley, 1968; Ober et al., 1983; Rakavy & Shaviv, 1967; Stringfellow & Woosley, 1988; Wheeler, 1977). The thermal concentration of these pairs occur during the advanced burning phase of the stars' evolution and causes a dynamic instability in the star (Woosley & Heger, 2015). This instability results in explosion of the massive star as PISN. However, the pair-instability is a vital process in explosion and collapse, of not only massive stars but also in many astrophysical objects, such as in mass-loss from black hole mergers (Belczynski et al., 2016) and in some models of the Universe which predicted that first stars at Dark Ages might form massive stars and become subject to pair-instability (Abel et al., 1998;

Abel et al., 2000; Bromm et al., 2002; Bromm & Larson, 2004; Chatzopoulos & Wheeler, 2012a). On the other hand, since neutrino emission process in PISN is similar to the one in Type Ia supernovae (Kunugise & Iwamoto, 2007; Odrzywolek & Plewa, 2011; Seitenzahl et al., 2015; Wright et al., 2017; Wright et al., 2016), the best method to differentiate different types of stellar explosions from others is by neutrino emission signal (Wright et al., 2017). Thus, we can say that neutrino emission and its energy-loss are equally important quantities in determining various types of supernova explosion (Odrzywolek & Plewa, 2011). For example, most of energy emitted from long detected LMC supernovae are neutrinos (Spergel et al., 1987).

1.3 Research Objectives

Very-massive stars with carbon-oxygen core within the range of 60 $M_{\odot} < M_{CO} < 133$ $M_{\odot}$ become dynamically unstable due to pair-production when their central temperature is high. In line with lack of adequate knowledge about the pair-production and neutrino cooling in the instability regions of very-massive stars, this work is aimed at investigating three important aspects that strongly influence the end fates of very-massive stars as a results of pair-production and neutrino cooling from the stars. Specifically, progenitor models with carbon-oxygen cores, within the range of 60 $M_{\odot} < M_{CO} < 133$ $M_{\odot}$ are considered as well as models for 120, 150, 200, 300, 500 $M_{\odot}$, with rotation and 120, 150 and 500 $M_{\odot}$ without rotation at LMC that has a metallicity $Z = 0.006$.

The main objectives of this research work can be itemise as follows:

I. To investigate adiabatic effects of electron-positron pair-production on dynamical instability of very-massive stars with carbon-oxygen cores, within the range of 60 $M_{\odot} < M_{CO} < 133$ $M_{\odot}$.

II. To compute thermal energy, pressure, and entropy due to electron-positron pair-production from the instability regions of very massive stars with carbon-oxygen cores, within the range of 60 $M_{\odot} < M_{CO} < 133$ $M_{\odot}$.

III. To evaluate neutrino energy-loss from instability regions of very massive stars with carbon-oxygen cores, within the range of 60 $M_\odot < M_{CO} < 133\ M_\odot$.

IV. To calculate neutrino energy-loss from stellar models of 120, 150, 200, 300, 500 $M_\odot$, with rotation and 120, 150 and 500 $M_\odot$ without rotation at LMC that has a metallicity $Z = 0.006$.

1.4 Thesis Organization

This thesis is divided into six chapters. Chapter 1 (this chapter) provides background of the research work. A general introduction, statement of problems intended to solve and objectives of research are also presented in this chapter. Chapter 2, is for Literature review relating to very-massive stars, their evolution and end fates. Nuclear reactions involved in massive stars, production of electron-positron pairs in massive stars, neutrinos in massive stars and mass of progenitor star expected to reach instability region and explode as PISN. Discussions on methodology employed in carrying out this work is provided in Chapter 3. While Chapter 4 presents results and discussions; this include; adiabatic effects of pair-production on dynamical instability of very-massive stars. Thermal energy, pressure, and entropy of electron-positron pairs in the instability regions, and results of numerical calculations for neutrino-energy loss from the instability regions of the progenitor models, and thermal neutrino processes from selected stellar models. Chapter 5 is recommendation for future work, which described kinetics of non-equilibrium electron-positron pair plasma. And finally, Chapter 6 summarizes and conclude findings of the research. Recommendations for future work are fully provided in Chapter 5 & 6.

1.5 Chapter Summary

This chapter discusses background of this research work. General introduction of the thesis and problems intended to address are clearly defined. Similarly, objectives of the research are outlined.

CHAPTER 2: LITERATURE REVIEW

2.1 Introduction

Very long ago, Barkat et al. (1967) postulates that dynamical instability caused by pair-production occur in massive star prior to formation of any elements heavier than oxygen. In 2012; Chatzopoulos and Wheeler (2012a) found that the criteria for any star to enter instability regime in density- temperature region; is dependent on mass of oxygen cores, main sequence mass that produce a given oxygen core mass which in turn is dependent on; metallicity, mass loss, convective and rotationally induced mixing. Woosley and Heger (2015), believed that only very-massive stars that have sufficient entropy would encounter this instability. However, in another development, observations revealed that there is greater energy release from oxygen burning, and so explosion of stars after collapse is of greater intensity (Takahashi et al., 2016). In this chapter, we review the phenomenology of massive stars; their formation, evolution, and death etc. We similarly review nuclear reaction processes involved in the evolution of massive stars, and neutrinos in massive stars.

2.2 Massive Stars

Stars are gravitationally confined thermonuclear reactors whose composition evolves as energy is emitted into radiation (as photons), and neutrinos, in hydrostatic equilibrium. During a clear night, several stars in the sky are seeing, for example; in the northern hemisphere, the brightest stars includes Sirius, Vega, Betelguese, Caopus, Arcturus, Rigel, Altair, Antares, Polaris, Achemar, and Cotar etc., which are all seeing with our naked eyes. Massive stars are stars that reached or will reach a mass greater than ~10 $M_\odot$ (Martins, 2015) which are scattered in Galactic plane and confined within a disk subtending an angle below 0.8^o with mid-plane. The term massive star and very-massive star may be used in this work interchangeably. However, in many works, very massive stars are stars in the mass range of $100\ M_{\odot} \leq M_S \leq 1000\ M_{\odot}$. They typically have high luminosity $10^4 - 10^6\ L_{\odot}$, and are essentially the major producers of alpha particles, since they go beyond carbon burning phase, and produces several elements heavier than oxygen. Due to their high luminosity, they released a material as fresh wind in their cores, and transport it to its surface which is subsequently released to the immediate surroundings. They are massive enough to explode as supernova and are primordially central to evolution of the Universe. Massive stars spends about 90% of their life burning hydrogen and most of the rest burning helium. They have very complex nuclear network, which generally ends their lives after silicon burning. Their interiors are unique physical laboratories for nuclear physics, magnetohydrodynamics, particle physics, and general relativity, conditionally not found elsewhere in the Universe. They are excited by radiation which stir the ISM and may even affect evolution of galaxies. Their explosions teach astronomers a great information about the origins of much of the materials that makes up our Universe. In fact, many Astrophysicists believe that, a supernova explosion might be the agent that triggered formation of our own solar system. However, about 75% of these supernova explosions results from massive stars (Kozyreva, 2014). Massive stars are not many in number but they make a large impact to the properties of galaxies. They are essential in the heavy elements productions and to the energy balance in the interstellar medium. They are also vital in regulating rate of star formation on large scales through intense winds, radiation and supernova explosions. One important role of massive stars is that they are progenitors of blue supergiant (BSG), red supergiant (RSG), Wolf-Rayet (WR) and luminous blue variable (LBV) stars. The cores of massive stars also become neutron stars (NS) or black holes (BH) after their collapse. They are major sites for nucleosynthesis, which takes place during pre-supernova (hydrostatic) burnings as well as during explosive burnings. Many numerical simulation results show that the first generation stars were predominantly massive or very massive (Bromm, 2005). It is important to note that, on main sequence, and due to strong ionizing fluxes that produce HII regions, massive stars have high effective temperature that exceeds 2.5×10^4 K and they are very cool (3500 K) in their latest phase of evolution which is the red supergiant phase. However, depending on their initial mass, they also become hot (10^5 K) in Wolf-Rayet stars. In the main sequence stars, the nuclear energy is provided by the remaining hydrogen over a timescale of $\tau_N \sim 7 \times 10^9$yr ($M_S$/ $M_\odot$)($L_\odot$/L_S), which means that all massive stars have short lives, spanning only $\sim 2 - 20$ million years and ends their lives as supernova (Martins, 2015). This, can be visualise when thermal (Kelvin-Helmholtz) timescale τ_{KH}, which is the ratio of thermal energy to luminosity, is considered and after applying Virial theorem, we get the lifetime as given in Equation 2.1 below:

$$t_{KH} = \frac{GM_S{}^2}{(R_S L_S)} \tag{2.1}$$

where G is the gravitational constant, M_S the mass of the star, R_S radius of the star and its luminosity is L_S. This equation quantifies the time of the collapse of massive star in the absence of a nuclear energy which is about 3×10^7 yr for the Sun.

2.2.1 Formation of Massive Stars

Although they are key in astrophysics, the physical processes responsible for the birth of massive stars still remain a mystery. Some people argued that massive stars should not even exist based on basic theory. And how do/long a massive star is formed? Are questions afflicted by confusion. The simple reason for this is that they are formed in a distant and highly obscured regions, and exists in dense clusters which hinders the understanding of their properties individually. Generally, a star formation is kick-start by condensation of a collapsing gas inside a large compact mass of molecular cloud, then a proto-star is form, which increase the mass from the neighbouring gas, while at the same time mass is loss through an escape and paralleled atmospheric burst. The many processes acting simultaneously in massive stars make them difficult to be theoretically analysed. Hot molecular core observation suggested a formation time of about 100, 000 years, due to their formation in rich clusters emitting copious amounts of photon ionization which alter the neighbouring environment. It is almost not possible to resolve the forming cluster with current telescopes. This, however, make it difficult to deduce the primordial configuration of the molecular cloud which represents the initial conditions for massive star formation. However, with modern observational techniques, such as modern telescopes which are powerful enough, a number of very massive stars have been observed. The following Table 2.1, lists few of the observed very massive stars with an estimated initial mass. The majority of stars thought to be 150 $M_{\odot}$ or greater are shown. The method used to determine the mass is included in order to give idea about the uncertainty. Most of these stars that have higher masses greater than 100 $M_{\odot}$ are located in the Magellanic Clouds (Martins, 2015). For example, all the R136 stars are in the LMC where the metallicity is almost half the solar metallicity and is located at about 163,000*ly* from the Earth. Because luminosity is the first criterion to distinguish very-massive stars; various examples of very-massive stars based on luminosity in the Magellanic Cloud are postulated. For example, in 1983 Humphreys (1983), reported the brightest blue and red supergiant of six galaxies (MW, SMC, LMC, M33, NGC6822, and IC1613) in the local group. The atmosphere/luminosity method of stellar mass determination is the most often quoted and it compares the predictions of evolutionary method simply by Hertzsprung-Russel diagram.

2.2.2 Evolution and Fate of Massive Stars

The life of a massive star is governed by a simple principle. A pressure, which is a combination of an ideal gas, radiation, and in the end, partially degenerate electrons, keep up the star against gravitational force. However, the star still evolves due to radiation (Woosley et al., 2002).

Table 2.1: List of some observed very-massive stars with current-evolved mass, name of star, method of mass estimate, and location based on references in last column. Only stars greater than or equal to 150 $M_\odot$ are given.

Evolved mass [$M_\odot$]	**Name**	**Method of mass estimate**	**Location-(Distance from earth)**	**Reference**
150	VFTS 682 (WR)	Atmosphere/Luminosity	LMC	Bestenlehner et al. (2011)
150	R136a6	Evolutionary	LMC	Crowther et al. (2016)
150	HD269810	Evolutionary	LMC	Walborn et al. (2004)
152±51	HD15558	Binary	MW	De Becker et al. (2006); (Garmany & Massey, 1981)
175	Peony star (WR 102ka)	Atmosphere/Luminosity	MW	Barniske et al. (2008)
179	Melnick 34	Atmosphere/Luminosity	LMC	Zwart et al. (2002)
180	R136a3	Evolutionary	LMC	Crowther et al. (2016)
189	Melnick 42	Atmosphere/Luminosity	LMC	Bestenlehner et al. (2014)
195	R136a2	Evolutionary	LMC	Crowther et al. (2010)
226	BAT99-98	Atmosphere/Luminosity	LMC	Hainich et al. (2014)
230	R136c	Evolutionary	LMC	Crowther et al. (2016)
315	R136a1	Evolutionary	LMC	Crowther et al. (2016)

Massive stars evolve very quickly, and most of the important evolutionary phases lived very shortly, in order to immensely contribute to the chemical evolution of the Universe. The convective cores of the massive stars is powered by Carbon-Nitrogen-Oxygen (CNO) cycle. While their surface is not convective, in the end of hydrogen burning, the helium burning is ignited, beyond which, the evolution is accelerated by thermal neutrino losses, especially from electron-positron pair annihilation. Furthermore, the final fate of very massive stars differs according to their mass. The hydrogen burning process ends only within million years, and the star continuously evolve far beyond helium burning. In their evolutionary trends, massive stars follow similar events to those in lower-mass stars; first a hydrogen shell, then a core burning helium to carbon, surrounded by helium-and hydrogen burning shells. After exhausting the hydrogen fuel in the cores, they leave the main sequence. In the late stages of the evolution of the massive stars, and when the core passes carbon burning stage, the temperature becomes high to about 10^9 K, and photons are emitted in accordance to Planck's law, such that high energy photons in the end of energy distribution exceeds the rest-mass energy of an electron-positron pair $(m_e c^2 \sim 0.5 MeV)$ (Kozyreva, 2014). And the structural adiabatic index $\gamma = \frac{d(lnp)}{d(ln\rho)}$ falls below dynamical stability threshold of 4/3, which leads to dynamical instability in the core. In Blinnikov et al. (1996), it is demonstrated how the photon gas at 10^9 K kick-starts the creation of pairs and the adiabatic index sharply drops below 4/3.

2.2.3 Death of Massive Stars

Massive stars are very fascinating when they die. Their death is marked by either black hole production or encountering pair instability, for helium cores heavier than 35 $M_\odot$. There are many other possible outcomes depending on the initial compositions of the star, rotation, and the models' physical parameters used during the evolution. In essence, the product of the death of a massive star is associated with four physical quantities- the mass, metallicity, and rate of mass loss and rotation. For further details on this, Woosley and Heger (2015) defined five outcomes and give approximate mass ranges for which each result falls. The pair-instability is within the helium core mass range of 63 to 133 $M_\odot$. The dynamical instability that lead to collapse of oxygen cores also results to explosion when temperature increases. This produces more energy from nuclear burnings, and then the collapse of stars terminates and reversed into explosion. The results of these explosions is PISN.

2.2.4 Rotation in Massive Stellar Models

Stellar evolution is strongly affected by rotation, which is why it is included in most of the stellar evolution codes. Stars rotate, because it is actually quite hard for them not to, and in practical terms, all-stars rotate around their axis. In particular, the chemical evolution of stars and, in general, galaxies are interestingly affected by rotational effects. One of the most important effects of rotating stellar models is the output of the models, such as their evolutionary tracks and lifetimes, the nature of supernova explosions and of other stellar remnants. As a consequence, the output of many rotating models have shown different properties from the non-rotating models. For a detail review about effect of rotation in massive stars, see Maeder and Meynet (2012). Massive stars are often rapid rotators, with a different equatorial velocities of about 200 km s^{-1} in main sequence, which is a very significant fraction of their breakup rotational velocity (Woosley et al., 2002). In the review work by Maeder and Meynet (2011), the consequence of rotational effects in stellar models are broadly classified into four groups, these are;

I. The equilibrium configuration of rotating stars resulting from the centrifugal force acting on the stellar equilibrium
II. The rotational effects on mass loss or accretion
III. The rotational mixing
IV. The interactions with magnetic field

Figures 2.1 & 2.2, illustrates change in HR diagram due to rotation effect in the evolution of very massive stars of 120, 150, 200, 300 and 500 $M_\odot$ models with solar metallicities of 0.006 respectively. In both figures, the track of the models including rotation effects is shifted to slightly lower effective temperature and luminosity and the nucleosynthesis altered the rotation occurring in the stars. These changes is due to reduction in effective gravity of centrifugal force during the rotation and also due to hydrogen burning core when the main sequence becomes enlarged with rotationally-induced chemical mixing.

The increase in rotation brings about a chemically homogeneous evolution and produce higher oxygen core mass, which is necessary for pair-production in the core of massive stars. Thus higher degrees of rotation in massive stars brings the star much closer to density-temperature plane, where the adiabatic index is below 4/3.

2.2.5 Mass-Loss from Massive Stars

Massive stars loses mass through different triggering processes. For example, in post-main-sequence evolution, the mass of a star is lost through ejection of stellar winds. The mass loss in massive stars is an important process that cannot be disregarded and is mostly efficient during hydrogen burning phase. It increases substantially with luminosity of a massive star (Andriesse, 2000). It also lead to a significant reduction of total mass of a star. The mass loss does not only affects the star's luminosity but also He-core mass and its entire burning lifetime which consequently, has impact on the end fate of a star. Smith (2014), provides complete review about effects of mass loss on the evolution and fate of massive stars. During most of the lifetimes of massive stars; mass loss is essential in finding the resulting supernova explosions. As such, mass loss is adamantly associated with evolution and end fate of massive stars.

2.2.6 Evolution Equations

The fundamental physical quantities that describe stellar structure, in general, are radius and time(r, t). Other variables of particular importance are density ρ, temperature T, and chemical composition X_i or abundances of elements in stellar medium. The hydrostatic pressure P which balances gravitational force towards centre of stars and prevents it from collapse is given from;

$$\frac{d^2\vec{r}}{dt^2} = -\left(\frac{1}{\rho}\nabla P + \nabla V\right) \tag{2.2}$$

And the gravitational potential satisfies Poisson's equation given by;

$$\nabla^2 V = 4\pi G\rho \tag{2.3}$$

where G is gravitational constant.

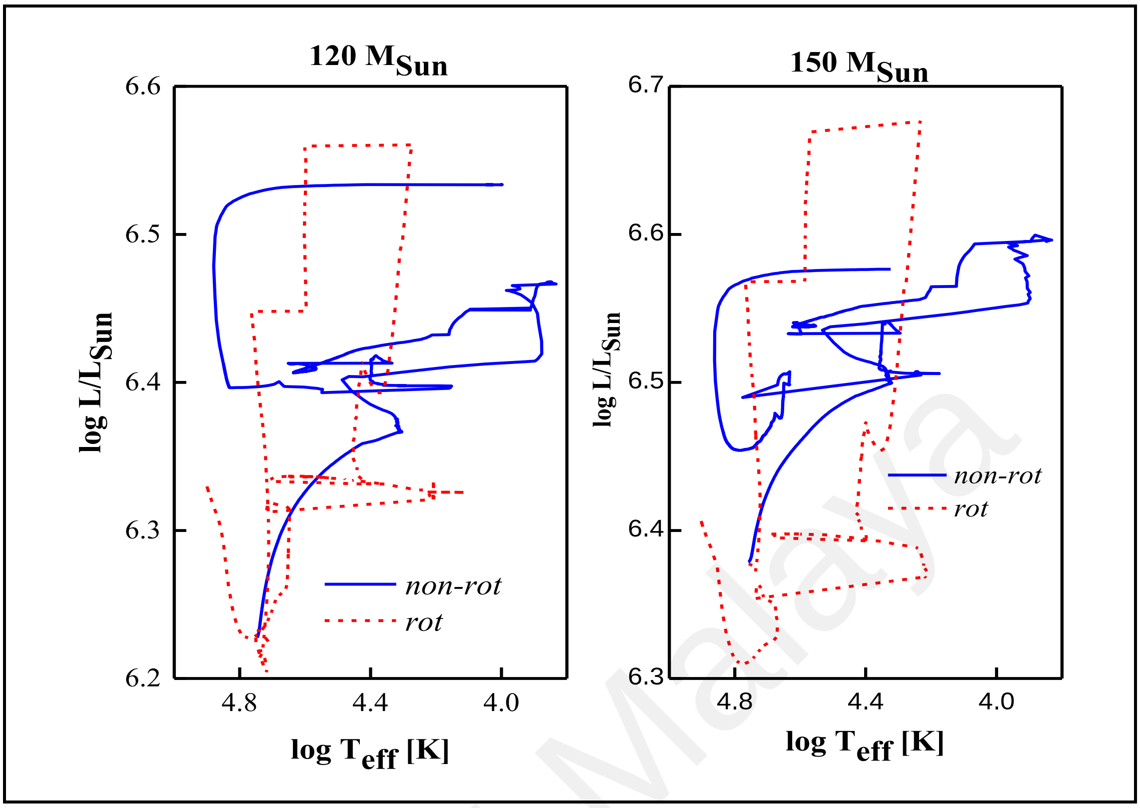

Figure 2.1: Evolution of 120, 150 M⊙ massive stars in Hertzsprung-Russel (HR) diagram. Data taken from Yusof et al. (2013).

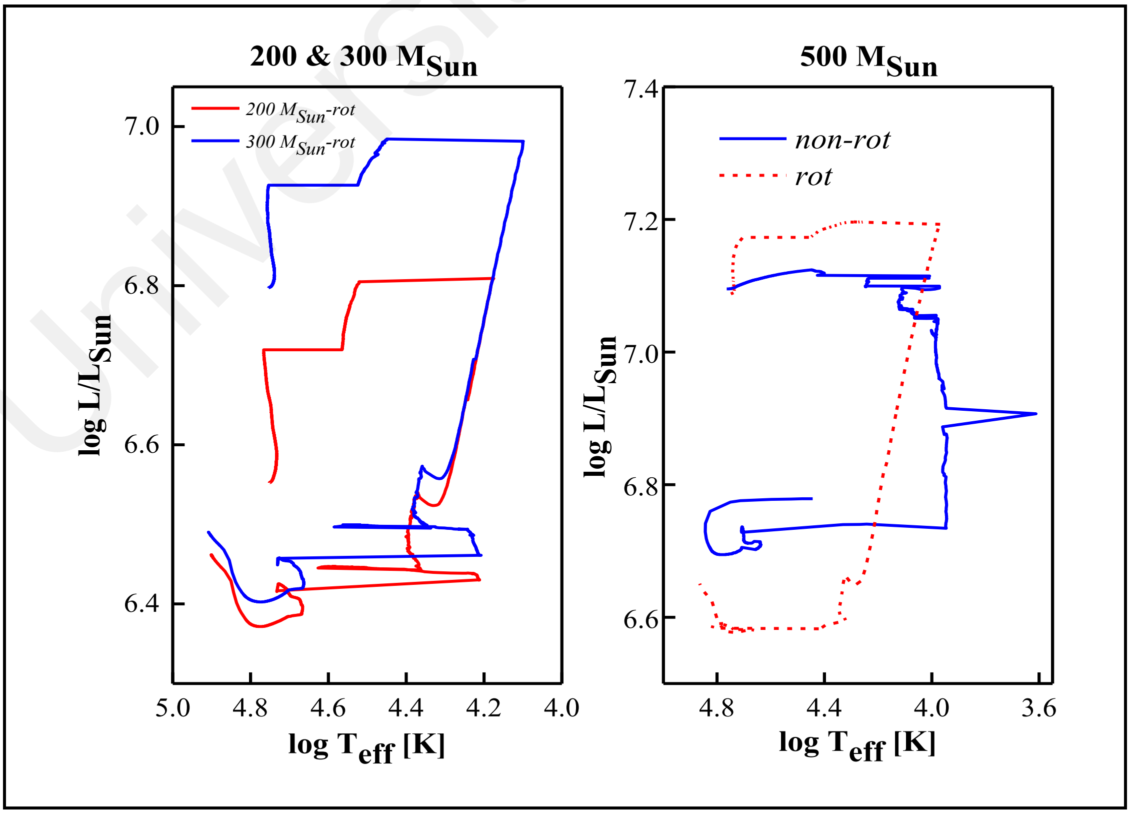

Figure 2.2: Evolution of 200, 300 & 500 M⊙ massive stars in Hertzsprung-Russel (HR) diagram. Data taken from Yusof et al. (2013).

Assuming the star is spherical, the star will depend only on distance r from centre and the gravitational potential $\nabla V = \frac{\partial V}{\partial r} = \frac{GM_r}{r^2}$, M_r is the mass conservation within stellar radius and can be given by;

$$M_r = 4\pi\rho \int_0^r \vec{r}^2 d\vec{r} \tag{2.4}$$

By differentiating this equation with respect to distance from centre gives "continuity of mass equation" given by;

$$\frac{dM_r}{dr} = 4\pi r^2 \rho \ or \ \frac{dr}{dM_r} = \frac{1}{4\pi r^2 \rho} \tag{2.5}$$

From these equations, we can rewrite Equation 2.2, as

$$\frac{dP}{dr} = -\rho(r)\left[\frac{GM_S}{r^2} + \frac{d^2 r}{dt^2}\right] \tag{2.6}$$

However, the time derivative in Equation 2.6, is negligible for a hydrostatic equilibrium ($\frac{d^2r}{dt^2} = 0$). As thermonuclear reactions begins, the star loses energy through radiation, and total heat flux (luminosity) flowing the star is given by;

$$\frac{dL(r)}{dr} = 4\pi\rho r^2 \varepsilon(r) \tag{2.7}$$

where $\varepsilon(r)$ is heat flux which is proportional to temperature gradient:

$$\varepsilon(r) = -\sigma \frac{dT(r)}{dr} \tag{2.8}$$

σ is Stefan-Boltzmann constant. Equation 2.7 can be rewritten in terms of M_r as;

$$\frac{dL(r)}{dM_r} = \varepsilon(r) \tag{2.9}$$

which is the conservation of energy equation. When heat transport is through radiation, the local thermodynamics equilibrium provides $P_{rad} = a\frac{T^4}{3}$ and hence;

$$\frac{dT(r)}{dr} = -\frac{3\kappa_{rad}\rho}{4acT^3} F_{rad} \tag{2.10}$$

This is radiative transport equation in the interior of stars when energy is carried by photons. κ_{rad} is radiative opacity (Rosseland opacity) per unit mass in stellar interiors, and can be defined by

$$\kappa_{rad} = \frac{4acT^3}{3\rho\sigma} \tag{2.11}$$

where c is speed of light and a is radiation constant. It can be seen from Equation 2.10 that for every temperature gradient, there is a radiative flux F_{rad}, which may not be total outgoing flux. However, when total energy flux is transported by photons, then Equation 2.10, becomes;

$$\frac{dT(r)}{dr} = -\frac{3\kappa_{rad}\rho}{4acT^3}\frac{L_r}{4\pi r^2} \tag{2.12}$$

Which represent processes of absorption and re-emission of photons in the interior of stars through a mean opacity coefficient κ_{rad}. Meanwhile, for conductive transport, i.e. when energy is transported by constituent of the stellar matter (free non-degenerate electrons), the energy flux is approximately given by;

$$F_e \cong -N_e\bar{v}l\frac{dE}{dr} \tag{2.13}$$

where N_e is electron number per unit volume, l and $\bar{v}$ are mean free path and average velocity of electrons respectively and $E \propto k_BT$ is electrons average kinetic energy. This equation can be written as;

$$F_e \cong -N_e k_B \bar{v} l \frac{dT}{dr} \tag{2.14}$$

This equation represent the approximate relation for energy transport due to heavier constituents of stellar gas. However, studies on processes of interaction between constituents of stellar gas shows that radiation transport dominate over electron (conduction) transport. Perhaps, heavy particles energy transport is by far less efficient, because ions are mainly outnumbered by electrons and at a given temperature, the ions move very slowly. On the other hand, when electrons are degenerate, they can transport energy efficiently due to their long mean free path (contrary to non-degenerate case). In this later case, the total energy flux is, therefore,

$$F = F_{rad} + F_e \tag{2.15}$$

Hence, the general equation of radiative and conductive energy transports in stellar interior is given from Equation 2.12;

$$\frac{dT}{dr} = -\frac{3\kappa\rho}{4acT^3}\frac{L_r}{4\pi r^2} \tag{2.16}$$

It is worth to note that, the opacity here, κ is given by;

$$\frac{1}{\kappa} = \frac{1}{\kappa_{rad}} + \frac{1}{\kappa_e} \tag{2.17}$$

where κ_e is electron opacity, such that for an effective electron conduction $\kappa_e \ll \kappa_{rad}$, and hence, Equation 2.16, becomes

$$\frac{dT}{dM_r} = -\frac{3\kappa}{64\pi^2 acT^3}\frac{L_r}{r^4} \tag{2.18}$$

The next energy transport in the stellar interior, which serves as a process of energy and chemical elements transport, is convection. In the interior of stars, matter are dynamic, such that the gas elements are in small random motion around their equilibrium positions. This motion may trigger large-scale motions involving total stellar mass, just like water motion in a container heated from its underneath. In the stellar interior, hot gas elements are rise up, such that energy is transported from high temperature to low temperature regions and then cool and fall down as cold material. However, this process is extremely complicated to be treated in stellar interiors and therefore needs many physical assumptions. Detail discussion about convection transport in the stellar interior can be found in chapter three of the book authored by Maurizio and Santi (2005). The convective energy flux at a given layer within the convective region can be defined as total flux energy minus flux carried by radiation

$$F_{conv} = F - F_{rad} \tag{2.19}$$

where $F = \frac{L_r}{4\pi r^2}$ is the total energy flux and F_{rad} is given by Equation 2.10. Whence, the energy flux transported by matter elements in terms of average speed v of the convective elements, can be given, after imposing various conditions, as

$$F_{conv} = \frac{1}{2}\rho v c_p T \propto_{ml} (\nabla - \nabla_{ad}) \tag{2.20}$$

where $\propto_{ml} = \Lambda/_{H_P}$ is a constant free parameter, and Λ is the mean free path (or the mixing length), H_P is a multiple of local pressure scale height defined by $(H_P)^{-1} = -{}^{dlnP}/_{dlnr}$, ∇_{ad} is an adiabatic gradient and ∇ is an unknown temperature gradient in the convective region, while, c_p is a specific heat per unit mass at constant pressure. Similarly, the term $\frac{1}{2}\rho v$ provides the flux of mass per square centimetre per second. While the factor (1/2) takes into account the fact that at each layer approximately half of the matter is rising and half is moving downwards. It is interesting here to note that the convective flux depends on free parameter $\propto_{ml}$. Finally, the total flux from Equation 2.19, is equal to sum of the radiative plus the convective fluxes, given by;

$$F = \frac{L_r}{4\pi r^2} = F_{rad} + F_{conv} = \frac{4acgT^4}{3\kappa P}\nabla + \frac{1}{2}\rho v c_p T \propto_{ml} (\nabla - \nabla_{ad}) \tag{2.21}$$

where $\frac{dT}{dr} = -\frac{T}{H_P}\nabla$ and for hydrostatic equilibrium with g been local acceleration of gravity, $H_P = \frac{P}{g\rho}$.[1]. These Equations 2.2 - 2.21, described the time evolution of a star with a chemical composition of $X_i(M_r)$, under specified boundary conditions.

2.3 Nuclear Reactions in Massive Stars

The source of most of the elements heavier than helium in todays' Universe is believed to originate from nuclear processes occurring in massive stars. In general, different nuclear processes take place simultaneously in stellar plasma and nuclides created by fusion reactions are destroyed by another reaction. Meanwhile, the nuclear burning phases that are important in massive stars, are Carbon (C), to Neon (Ne), Oxygen (O), and finally Silicon (Si) burnings. In a typical main sequence stars, the chemical compositions are given by $X + Y + Z = 1$, such that $X = 0.7$ is the hydrogen mass fraction, $Y = 0.28$ is the helium mass fraction and $Z = 0.002$ is the fraction of mass in elements heavier than hydrogen and helium, which are misleadingly called "metals" in astrophysics, with most of the elements being C, N, and O. However, the Z is usually called metallicity of the star. Figure 2.3, is a temperature-density evolution for centres of massive stars showing different compositions of massive stars with initial masses of 120,

[1] The equation for the convective velocity is given by $v^2 = \frac{1}{8} g \frac{\Lambda^2}{H_P} Q(\nabla - \nabla_{ad})$, where in special case of perfect gas with negligible radiation $Q = 1 - \left({}^{dln\mu}/_{dlnT}\right)_P$

150, 200, 300 and 500 M⊙ and metallicity $Z = 0.006$. Different representations of particular burning stage in the core is shown. These nuclear burning stages have different influence on the structure and evolution of the star. They are, for example, responsible for internal pressure preventing the stars from collapsing gravitationally. Only less than 10% of massive stars' life is spent for helium burning and rest, while mostly 90% of its life is use for burning hydrogen, and this is only because reactions with smallest Coulomb barriers will proceed most rapidly and account for most of the nuclear energy generation. Massive stars are the ultimate recyclers; they use the ashes of the previous stage as fuel for the next. The exhaustion of one fuel leads to ignition of the next until finally an inert core of iron is formed, from which no further energy can be gained by the nuclear burning (Woosley et al., 2002). These nuclear burning phases are basically classified into two; Major nuclear burning and advanced nuclear burning.

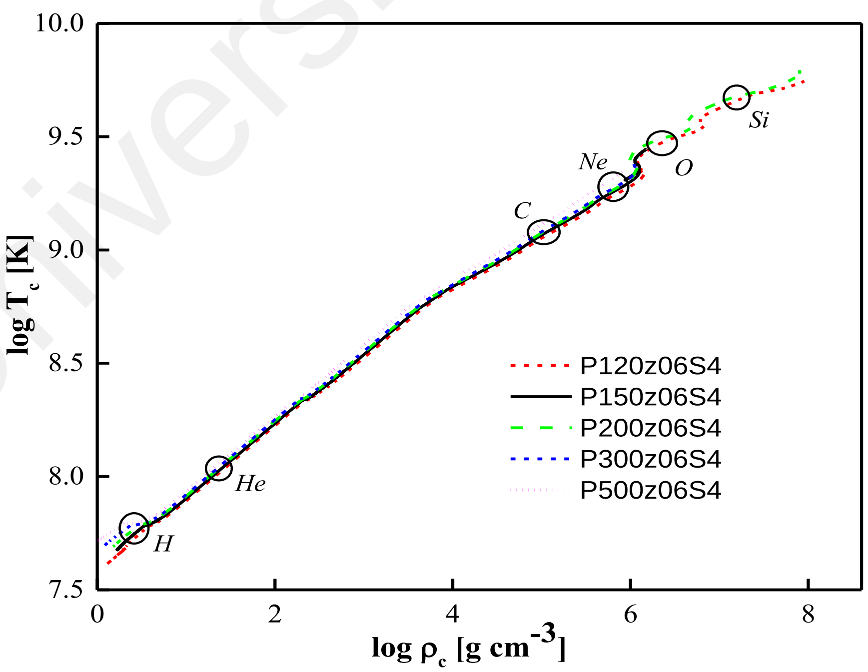

Figure 2.3: Evolution of the core of 120, 150, 200 300, and 500 M⊙ rotating models showing central temperature-density plane at Z = 0.006. Hydrogen-burning until silicon-burning phases are shown in circles. Data taken from Yusof et al (2013).

2.3.1 Major Nuclear Burnings

The hydrogen and helium burnings are referred to major burnings. These two phases of burning contribute almost entire nuclear reactions in massive stars. The hydrogen burning releases more energy per unit fuel consumed -about 10^{19} erg g^{-1}- compared to helium burning -of about 10^{18} erg g^{-1}- and also of advanced burning stages, which is about 5×10^{17} erg g^{-1} for carbon and oxygen burnings. This signifies that the hydrogen fuel is mostly consumed by a star more slowly than the other fuels in order to balance both gravity and energy radiated from its surface. Moreover, the nuclear energy released from hydrogen and helium burnings is mostly radiated as photons. In the following subsections, details of these burning stages is discussed.

2.3.1.1 Hydrogen Burning

This is the most important burning phase in any stellar evolution, as it is the longest nuclear burning phase occurring in the evolution of any star. The energy released by this burning process depends upon the initial composition; while for a 70% hydrogen by mass, the energy is about 26.731 MeV (4.51×10^{18} erg g^{-1}) (Woosley et al., 2002). Perhaps, this makes H-burning stars mostly observed than in any other phase. Nuclear fusion reaction of 4 protons into one ^{4}He nucleus is essentially the mechanism involve in the H-burning phase. This fusion reaction of H nucleus is achieved in two different but simultaneous chain reactions; namely the proton-proton (pp-chain) and the carbon-nitrogen-oxygen (CNO)-cycle. However, the relative efficiencies of these reactions is dependent on mass of the star.

(a) ***The CNO Cycle***

This combine two independent cycles; carbon-nitrogen (CN)-cycle and nitrogen-oxygen (NO)-cycle. There must be some isotopes of C, N or O in either of these cycles. The elements here are just acting as catalyst because they are both produced and destroyed during the same cycle. Table 2.2, shows nuclear burning reactions involve in CNO-cycle. In the CN, the cycle begins from any reaction provided the isotope responsible is found, and at a complete round of cycle, the isotope is consumed and reproduced again. The isotopes are abundantly equal when the temperature is high (about $15 \times 10^6\ K$), such that production rate is equal to rate of destruction. On the other hand, the NO cycle, is significant when temperature is higher to about approximately $20 \times 10^6\ K$. This clearly shows that, the temperature sensitivity of the CNO cycle is larger than that of the PP chain. Because of small dependence on temperature during the P-P chain, the H-burning involves a relatively large fraction of the stellar mass. In low main sequence, the lifetimes, which is a function of stellar mass during central H-burning phase, are very long and decrease as stellar mass increases. The effect of the stellar mass increase, is that the temperature significantly increase, which also make CNO cycle the dominant energy producer. This eventually ensures that the nuclear burning process is concentrated in the centre such that the energy production causes a steep increase of radiative gradient towards the centre. The core contracts much faster for massive stars, and the temperature required for He-burning is reached sooner. Furthermore, the core of the stars expands due to energy input as the CNO cycle activates, and in consequence, the central density decreases. The development and evolution of convective core during H-burning phase is also as result of activation of the CNO cycle. As can be seen in Figure 2.4, the convective cores, in the case of low mass star, appears temporarily with H-burning occurrence in radiative region but when the CNO cycle becomes dominant H-burning, the complete convective core appears. This is in contrary to more massive stars in which the transition from convective and radiative and back again, does not occur.

Table 2.2: CNO-cycle for H-burning phase in stars. The half- life for ^{13}N, ^{15}O, ^{17}F and ^{18}F are respectively 9.965 min, 122.24 s, 64.49 s and 109.77 min.

Cycles	Reactions					
CNO I	$^{12}C(p,\gamma)^{13}N$	$^{13}N(\beta^+\nu)^{13}C$	$^{13}C(p,\gamma)^{14}N$	$^{14}N(p,\gamma)^{15}O$	$^{15}O(\beta^+\nu)^{15}N$	$^{15}N(p,\alpha)^{12}C$
CNO II	$^{14}N(p,\gamma)^{15}O$	$^{15}O(\beta^+\nu)^{15}N$	$^{15}N(p,\gamma)^{16}O$	$^{16}O(p,\gamma)^{17}F$	$^{17}F(\beta^+\nu)^{17}O$	$^{17}O(p,\alpha)^{14}N$
CNO III	$^{15}N(p,\gamma)^{16}O$	$^{16}O(p,\gamma)^{17}F$	$^{17}F(\beta^+\nu)^{17}O$	$^{17}O(p,\gamma)^{18}F$	$^{18}F(\beta^+\nu)^{18}O$	$^{18}O(p,\alpha)^{15}N$
CNO IV	$^{16}O(p,\gamma)^{17}F$	$^{17}F(\beta^+\nu)^{17}O$	$^{17}O(p,\gamma)^{18}F$	$^{18}F(\beta^+\nu)^{18}O$	$^{18}O(p,\gamma)^{19}F$	$^{19}F(p,\alpha)^{16}O$

2.3.1.2 Helium Burning

The most abundant isotope produced after H-burning by a star is helium. When all hydrogen is consumed in the core, the star will contract and the central temperature increases. The helium burning, which is strong and under a partially relativistic electron degeneracy, is kick-started when central density and temperature are around 10^6 g cm^{-3} and $8\times 10^6\ K$ respectively, which is appreciably higher than those for hydrogen burning due to higher Coulomb barriers. The electron degeneracy is only removed with help of initial temperature rise at constant density during the ignition of He-burning. The physical process working during main core He-burning stage is almost similar irrespective of the stellar mass. The helium in the core of the star undergoes a nuclear transformation at a certain point of ignition and the end products of the He-burning process is transformation of *He* nucleus into a mixture of ^{12}C and ^{16}O and some traces of ^{20}Ne, which are respectively the third and fourth most abundant nuclides in the universe. In massive stars, the helium burning is main source of ^{16}O and ^{18}O and amounts to the cosmic ^{12}C abundance. The density-temperature range during this burning, in massive stars, is 10^2 – 10^5 g cm^{-3} and $1-4\times 10^8\ K$ respectively. The nuclear reactions taken place in He-burning are given in Table 2.3. The first and fundamental reaction is formation of ^{12}C from alpha-nucleus, which is called triple alpha reaction (3α). The 3α reaction involves a two sequential steps. The first step is for two alpha-particles interaction to temporarily produce ^8Be in an endothermic process and within a very short time (~ 10^{-16} s), the ^8Be disintegrates back into two alpha-particles.

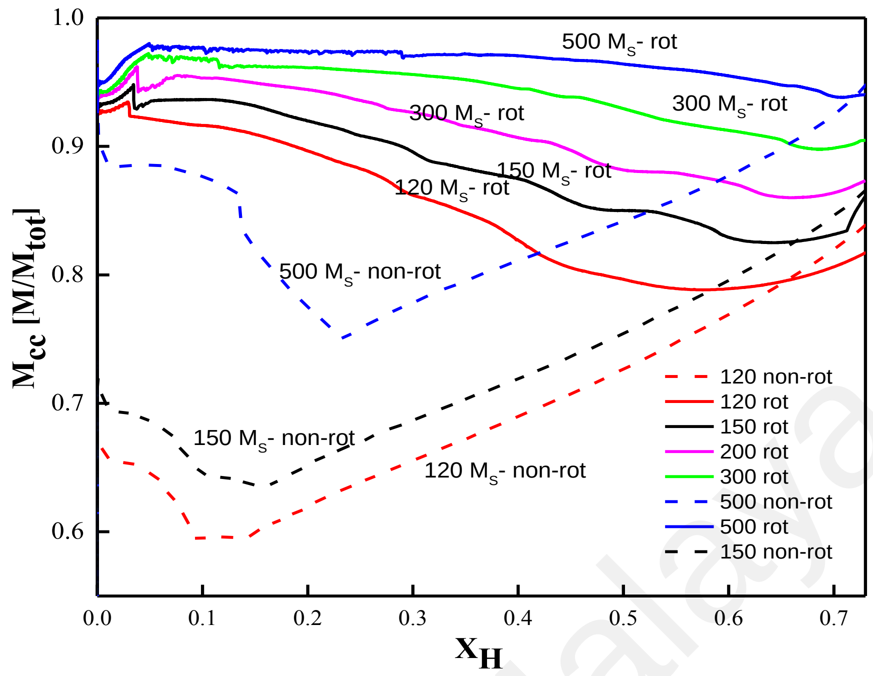

Figure 2.4: Mass of convective core as function of central abundance of *H* for various stellar masses and with metallicity z = 0.006. M represent solar mass $M_{\odot}$. Data taken from Yusof et al. (2013).

However, as the interior temperature increases, the probability of the second reaction to occur is enhanced, and over time, small concentration of ^{8}Be is sufficiently builds up to about 10^{-9} in the stellar matter, until the formation rate of ^{8}Be is equal to its decay rate. The increase in density then ensures a third-alpha interaction with the ^{8}Be to form ^{12}C nuclei via the second reaction. However, a temperature of the order of $\sim\ 1.2 \times 10^{8}\ K$ is required before 3α reactions produce a sizeable amount of energy. The amount of energy released per ^{12}C nucleus production is about 7.275 MeV, as can be seen in Table 2.3. It is shown that, for a given stellar mass, the life time of a core He-burning is almost 100 times less than that of H-burning. Similarly, it is expected that, during the core He-burning phase, the stars have extended convective cores. After the build-up of a sufficient ^{12}C abundance by 3α reaction, the other nuclear reactions proceeds, and the energy release per $^{12}C(\alpha, \gamma)^{16}O$ reaction is 7.162 MeV.

Table 2.3: Nuclear reactions of He-burning phase in stars with Q values. The Q value contain all available energy by a particular reaction in stellar matter.

Reactions	**Q-value [MeV]**
$^{4}He(\alpha)^{8}Be$	+7.275
$^{8}Be(\alpha, \gamma)^{12}C$	+7.275
$^{12}C(\alpha, \gamma)^{16}O$	+7.162
$^{16}O(\alpha, \gamma)^{20}Ne$	+4.730
$^{20}Ne(\alpha, \gamma)^{24}Mg$	+9.317
$^{24}Mg(\alpha, \gamma)^{28}Si$	Not available

In the end, only 3α and subsequent first two reactions are really relevant in the computations of stellar evolutions. Therefore, the final end products of helium burning are mainly ^{12}C and ^{16}O, and their abundance ratio depends on the He-burning conditions (i.e. temperature-density), which in turn, are determined by the stellar mass. The more massive a star is, the more ^{16}O is produced relative to ^{12}C. Overall, the outcome of helium burning is C / O ≈ 1:1 to 1:2. This precise abundance ratio ($^{12}C/^{16}O$) is influenced by rate of $^{12}C(\alpha, \gamma)^{16}O$ reaction. The Neon, Magnesium and Silicon productions are comparably less important in this burning stage.

2.3.2 Advanced Nuclear Burning

Although the star's life is mostly spent in the hydrogen and helium burning stages, it is the later burning stages that account for synthesis of the majority of heavy nuclides. Low and massive stars undergo different evolution scenarios and end their lives very differently. Due to inadequate temperature to overcome Coulomb repulsion in low mass stars, the thermonuclear reactions stops after He-burning. However, this is contrary to massive stars, where nuclear network is complex and continue to end after silicon burning. For a massive star, after exhaustion of helium burning, the core contracts such that temperature and density of the star increases, entering into a region of temperature-density plane where neutrino energy released at this stages is radiated as neutrino-antineutrino pairs, produced via electron-positron pair annihilation or photo-neutrino process. The rise of temperature, from one advanced stage to another, induces rapid acceleration of fuel consumption during this nuclear burning stages. Arising from this, the luminosity- effective temperature of a massive star can appear until the end of hydrostatic silicon burning. Therefore, observing a star in its advanced stages of evolution becomes probably difficult. Table 2.4, show nuclear reactions of the advanced burning stages in a star. In these nuclear burning stages, the reactions proceeds from carbon, neon, oxygen until silicon with respect to temperature rise. The ashes of a consumed burning nuclide become the fuel for next set of nuclear burnings.

Table 2.4: C-burning processes in massive stars and their respective Q value in MeV.

Reaction	**Q-value [MeV]**
$^{12}C(^{12}C,p)^{23}Na$	+2.241
$^{12}C(^{12}C,\alpha)^{20}Ne$	+4.617
$^{12}C(^{12}C,n)^{23}Mg$	-2.599
$^{12}C(^{12}C,\gamma)^{24}Mg$	+13.931
$^{12}C(^{12}C,2\alpha)^{16}O$	-0.114
$^{16}O(^{16}O,p)^{31}P$	+7.678
$^{16}O(^{16}O,2p)^{30}S$	+0.381
$^{16}O(^{16}O,n)^{31}S$	+1.499
$^{16}O(^{16}O,\alpha)^{28}Si$	+9.594
$^{16}O(^{16}O,2\alpha)^{24}Mg$	-0.393
$^{16}O(^{16}O,d)^{30}P$	-2.409
$^{20}Ne(\gamma,\alpha)^{16}O$	-4.730
$^{20}Ne(\alpha,\gamma)^{24}Mg$	+9.316
$^{20}Ne(\alpha,p)^{23}Mg$	+1.821
$^{24}Mg(\alpha,\gamma)^{28}Si$	+9.984
$^{26}Mg(\alpha,n)^{29}Si$	+0.034

2.3.2.1 Carbon Burning

When the core temperature exceeds $7 \times 10^{8}\ K$, Carbon burning takes place. Due to its lowest Coulomb barriers, ^{12}C-^{12}C fusion reaction is the first process that triggered this burning stage. The core abundance of carbon in massive stars is a key quantity which strongly affects all successive evolutionary stages (Arnett, 1972). This is because, carbon abundance essentially determines the availability of carbon for the core and shell C-burning. However, the magnitude of carbon abundance is dependent on nuclear cross section for $^{12}C(\alpha, \gamma)^{16}O$ reaction, which is why nuclear reaction rates of this reaction that is commonly used in stellar computations, affects the predictions of their final nucleosynthesis. The fundamental reactions at astrophysical energies of interest from this burning stage are the first three reactions in Table 2.4. The remaining processes from C-burning are of less important in this regard. Moreover, there are significant amount of elements produced particularly during shell burning, which is a result of carbon exhaustion and subsequent shifts of the burning process to a shell. However, the most efficient neutron source during this shell C-burning is $^{22}Ne(\alpha, n)^{25}Mg$.

2.3.2.2 Neon Burning

After the C-burning phase and when most of the ^{12}C nuclei have been consumed, the proceeding burning stages in the core of the star are mainly ^{16}O, ^{20}Ne, and ^{28}Si. As mentioned earlier, the gravitational contraction of the core of the star induces an increase of central temperature and density, which triggered ignition of subsequent burning phases. Due to small Coulomb barrier of the oxygen, the immediate reaction is photodisintegration of ^{20}Ne nuclei (particularly $^{20}Ne(\gamma, \alpha)^{16}O$) at a temperature of about $(1.2 - 1.9)10^9$ K which is an endothermic reaction. However, this burning phase always produces a convective core, irrespective of stellar mass and lasts only for a short period of time.

2.3.2.3 Oxygen Burning and Beyond

At the end of neon fuel consumption, ^{16}O, ^{24}Mg and ^{28}Si are main chemical composition in the core. The first reaction induced by combinations of these nuclides is fusion of ^{16}O due to the lowest Coulomb barrier of oxygen nucleus. This reaction produces a ^{32}S compound nucleus which is highly excited. This burning stage ignites when the core temperature is around $(1.5 - 2.7)10^9$ K and the most commonly reactions are given Table 2.4. This nuclear burning is able to overcome the neutrino losses as it always occur in convective cores of massive stars. As mass of the star increases, the lifetime of this burning phase decreases so that very massive stars born oxygen at higher core temperatures. However, when the central temperature attains $(2.8 - 4.1)10^9$ K, the Si-burning starts. This is the dominant process at end of the O-burning, and according to numerical simulations (Limongi et al., 2000), it can be divided into a radiative and convective different phases. The schematic diagram of these nuclear reaction processes is shown in Figure 2.5. The Si-burning gradually build up heavier nuclei, until ^{56}Fe, which at temperature $\geq 5 \times 10^9\ K$ break up due to photodisintegration into ^{4}He-particles and reverses the effect of all earlier burnings, thus a Nuclear Statistical Equilibrium (NSE) has been achieved. These processes, however, occur during explosions of supernovae.

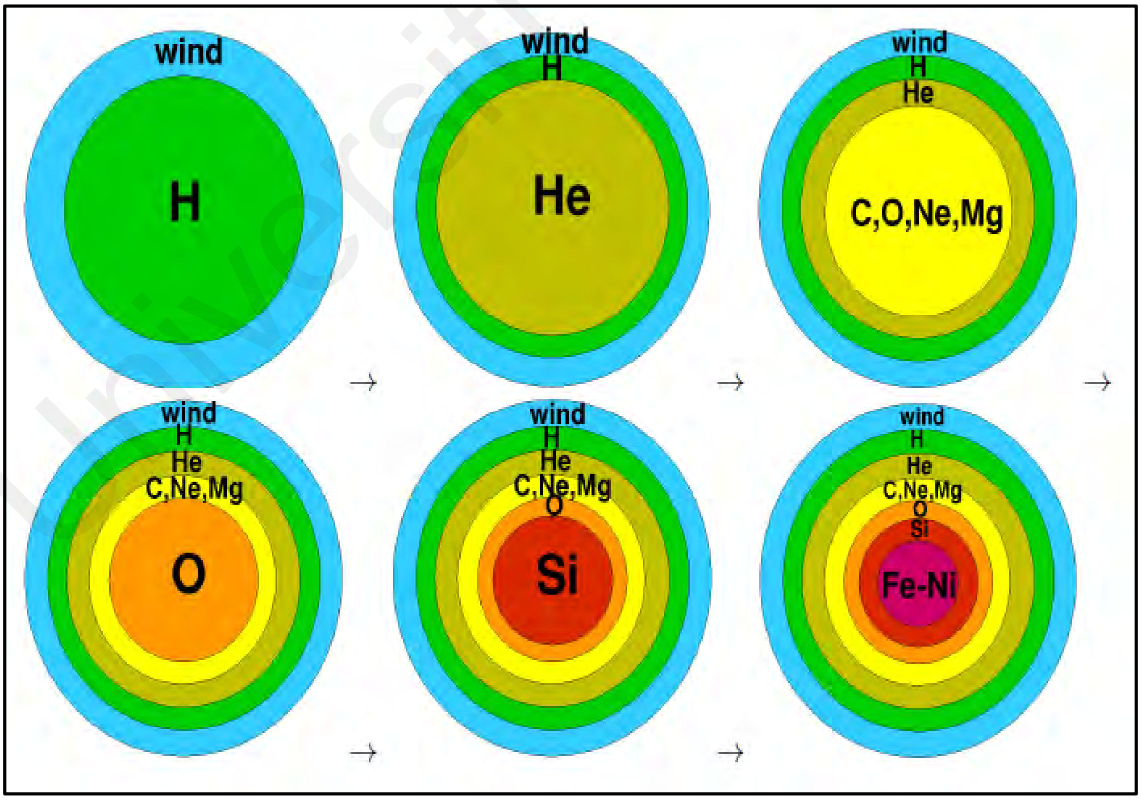

Figure 2.5: Schematic illustration of sequence of nuclear burning phases, showing all major and advanced burning stages. Picture taken from Kozyreva (2014).

2.4 Progenitor Mass of Pair-Instability Supernovae

A star could only experience pair-instability and explode as PISN when it is massive enough. The explosion of PISN is first identified by Barkat et al. (1967) in a detailed analysis of some relevant equation of states for very massive stars at the end of their lifetimes. It is generally originated when central temperature and density of a star are relatively high, (Arnett, 1996; Barkat et al., 1967; Fraley, 1968; Phillips, 2013; Rakavy & Shaviv, 1967) and then reach a region (as is shown in Figure 1.1) where the energy needed to create the rest mass of electron-positron pairs (at high entropy) softens the equation of state and reduce the adiabatic index below 4/3 (Fraley, 1968). The mass range required to undergo this process has been postulated by many researchers in astrophysics community. Many evolutionary calculations found that stars with oxygen core mass greater than 60 $M_{\odot}$ are dynamically unstable due to pair-production and instability set in when central temperature is high (Barkat et al., 1967). In 2002, Woosley et al. (2002) emphasized that pair-production is induced by an instability occurring only in massive stars with initial mass from around 120 $M_{\odot}$ and higher. However, for zero-age main sequence mass (ZAMS), the long-existing prediction was that, only non-rotating and zero-metallicity stars within the range of 140 $M_{\odot} < M_{ZAMS} < 260$ $M_{\odot}$ of ZAMS mass would explode as PISN (Heger & Woosley, 2002). While, Chatzopoulos and Wheeler (2012b), investigated about the minimum ZAMS mass of a star capable of reaching the instability region and demonstrates that stars with 65 $M_{\odot}$ would encounter full PISN and 40 $M_{\odot}$ would encounter Pulsational Pair-Instability Supernova (PPISN). Those results established a criteria for a ZAMS mass to enter the pair-instability region, which states that the instability region is controlled by mass of oxygen core, which in particular is highly dependent on mass loss, metallicity, and rotationally induced mixing, as well as convective and semi-convective instability. In the case of metallicity, Heger et al. (2003) found that there is a threshold of metallicity below which instability can occur, on account of strong metallicity dependence on massive star winds. However, this threshold is investigated by Langer et al. (2007). To emphasize on this, let consider Figure 2.6 which was taken from Heger et al. (2003). The figure show different types of supernova due to metallicity. The green line represent a separation regimes where stars keep hydrogen envelop from regimes where hydrogen envelop is lost. Similarly, the dashed blue line in this figure, represents boundary of regime of direct black hole formation (in black) which is only disrupted by a strip of PISNe that has no remnant.

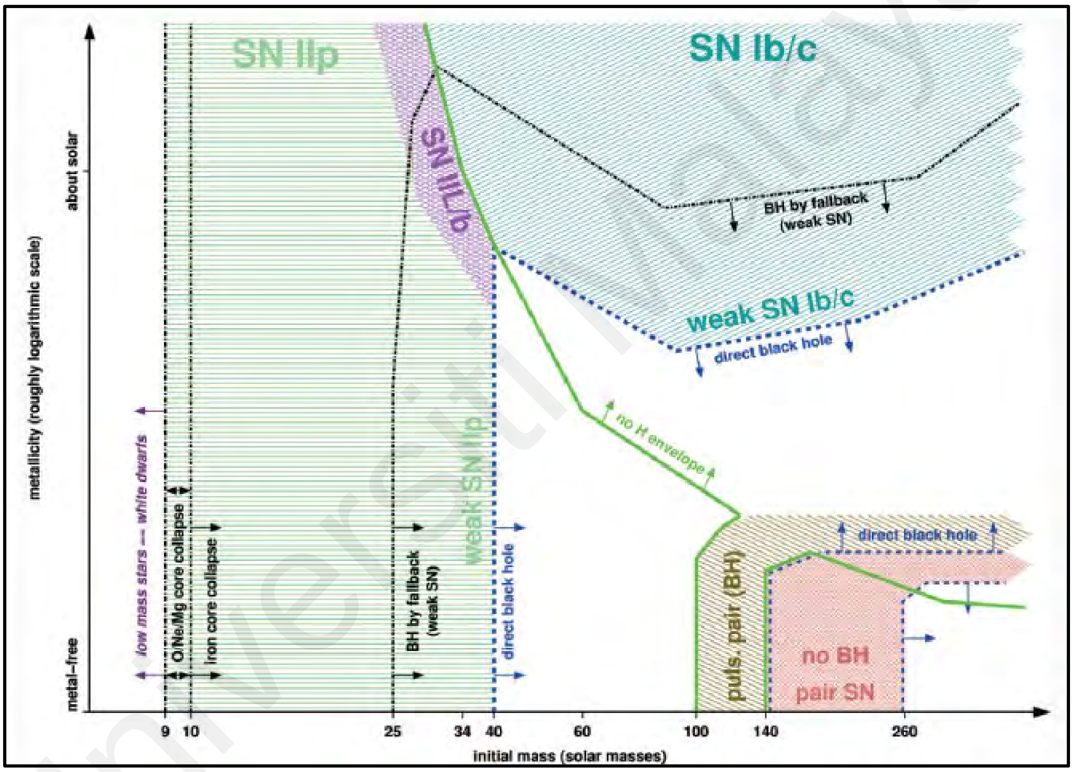

Figure 2.6: Types of supernova as functions of initial metallicity against initial mass. Picture taken from Heger et al. (2003).

It is also postulated that large metallicities produces low oxygen cores and therefore, stars on this range try to avoid instability regions (Chatzopoulos & Wheeler, 2012a; Kozyreva et al., 2014; Vink et al., 2011). And this condition is the most likely reason why instability does not exit at solar metallicity (Woosley et al., 2002; Yusof et al., 2013). Whereas, low metallicities reduces mass loss, and relatively allow lower mass main-sequence stars to encounter the instability (Chatzopoulos & Wheeler, 2012a). However, for mass loss effects, stars loose mass at all evolutionary phases and rate of mass loss varies depending on initial mass of the star. Thus, evolution of massive stars is strongly affected by mass loss and there are various mass loss prescriptions that are used for better understanding of different mass loss rates in stellar evolution models. The effects of rotation can be seen from comparison of rotating and non-rotating models. The rotating models live longer than non-rotating due to decrease in the rate of mass loss and rotation, which also reduce the final mass of the star. Effect of this can be verified by plotting mass-loss against final mass for rotating and non-rotating models, which also affects explosion mechanism of the stars by reducing threshold of pair-instability (Woosley, 2017). In another perspective, to determine the appropriate mass of a star expected to undergo the instability, Heger and Woosley (2002), established that mass range of massive stars with a helium-core mass that could explodes as PISN is within ~ 64-133 $M_{\odot}$. The helium-core mass greatly affects the nucleosynthesis in PISNe. Meanwhile, in stellar evolution models by Yusof et al. (2013); stellar progenitors that are expected to enter the instability region and explode as PISNe are found to be between about 100 $M_{\odot}$ and 290 $M_{\odot}$ rotating models in SMC metallicities and above 450 $M_{\odot}$ rotating and about 300 $M_{\odot}$ non-rotating models in LMC metallicities. The advantage in that later discovery is that many effects have been put into consideration before final conclusion. For instance, the benchmark for helium core mass given by Heger and Woosley (2002) is included. Similarly, metallicity factor, as highlighted in Vink et al. (2011) and others, is considered and finally, rotation effects, which facilitate a more chemically homogenous evolution, and produce higher oxygen-core that is necessary for instability, is also considered and compared with non-rotation. Perhaps, the progenitors need to retain higher mass, to maintain their helium-core mass above ~65 $M_{\odot}$. However, this condition is not guaranteed at high metallicities where stellar wind, mass-loss dominates evolution of very massive stars (Vink et al., 2011).

2.5 Neutrinos in Massive Stars

Neutrinos are produced either naturally or artificially. They are just produced everywhere; as there are still neutrino left over from the Big Bang around us. The natural sources are atmospheric neutrinos, high energy neutrinos, solar neutrinos, cosmic neutrino background and supernova neutrinos. These neutrinos and photons are believed to be produced in astrophysical beams of cosmic-ray particles interacting with matter at source object (Aartsen et al., 2017). They can, however, be made in nuclear reactors (reactor neutrinos) and particle accelerators (proton-accelerator neutrinos). Many information, both on general physics of neutrinos and particularly, on important astrophysical phenomena, can be provided from astrophysical neutrinos. They are very critical in determining the end fate of massive stars. Neutrinos are produced in large numbers from exploding massive stars and are extremely important probes of processes involve in supernovae before its explosion. Different neutrino processes and their reactions in massive stars are shown in Table 2.6. The three flavours of neutrinos are electron neutrinos(ν_e), muon neutrinos(ν_μ), and tau neutrinos(ν_τ) and each of these flavours is associated with a corresponding antineutrino. The neutrino and antineutrino emissions of different flavours from massive stars drives its gravitational binding energy away of compact remnant and brings the star to a cold final state through its initial hot phase (Janka, 2017). In principle, neutrino energy distribution from massive stars could provide great information about their explosion and, generally about neutrino physics.

2.5.1 Neutrino-electron interactions

Neutrinos and antineutrinos might interact with stellar matter such as neutrino-electron interactions. At low-energy neutrinos, this interactions may be assumed to go through elastic scattering process which has no regional boundary such that the initial and final states are equal. There are basically two interaction channels through which neutrinos interact with stellar matter;

I. Charge-current (CC) interaction channel

II. Neutral-current (NC) interaction channel

The neutrino-electron interactions is a free leptonic process with its amplitude easily calculated using Feynman rules of Standard Model (SM). Therefore, two channels propagates via exchange of W and Z bosons respectively, as is shown in the two Feynman diagrams, Figure 2.7.

Table 2.5: Neutrino processes in massive stars, taken from Janka (2016). The N represents nucleons (either neutron 'n' or proton 'p'), $\nu \in (\nu_e, \bar{\nu}_e, \nu_\mu, \bar{\nu}_\mu, \nu_\tau, \bar{\nu}_\tau)$ and $\nu_x \in (\nu_\mu, \bar{\nu}_\mu, \nu_\tau, \bar{\nu}_\tau)$.

Process	**Reaction**
Beta-process	
Electron and υ_e absorption by nuclei	$e^- + (A, Z) \leftrightarrow (A, z-1) + \upsilon_e$
Electron and $\upsilon_e$captures by nucleons	$e^- + p \leftrightarrow n + \upsilon_e$
Positron and $\bar{\nu}_e$captures by nucleons	$e^+ + n \leftrightarrow p + \bar{\nu}_e$
Thermal pair production and annihilation processes	
Nucleon-nucleon bremsstrahlung	$N + N \leftrightarrow N + N + \nu + \bar{\nu}$
Electron-Positron pair process	$e^- + e^+ \leftrightarrow \nu + \bar{\nu}$
Plasmon pair-neutrino process	$\tilde{\gamma} \leftrightarrow \nu + \bar{\nu}$
Photo-neutrino process	$\gamma + e^\pm \leftrightarrow e^\pm + \nu + \bar{\nu}$
Reactions between neutrinos	
Neutrino-pair annihilation	$\nu_e + \bar{\nu}_e \leftrightarrow \nu_x + \bar{\nu}_x$
Neutrino scattering	$\nu_x + (A, Z) \leftrightarrow \nu_x + (\nu_e, \bar{\nu}_e)$
Scattering processes with medium particles	
Neutrino scattering with nuclei	$\nu + (A, Z) \leftrightarrow \nu + (A, Z)$
Neutrino scattering with nucleons	$\nu + N \leftrightarrow \nu + N$
Neutrino scattering with electrons and positrons	$\nu + e^\pm \leftrightarrow \nu + e^\pm$

We can see from this figure that charge-current channel contribute to elastic scattering given by;

$$\nu_e + e^- \to \nu_e + e^- \tag{2.22}$$

While neutral-current contribution is;

$$\nu_r + e^- \rightarrow \nu_r + e^- \tag{2.23}$$

The r in Equation 2.23 stands for $r = \mu, \tau$. And according to Giunti and Kim (2007), for low-energy neutrinos, the effective Lagrangian for the above Feynman diagrams which described the two Equations 2.22 and 2.23 can be expressed as;

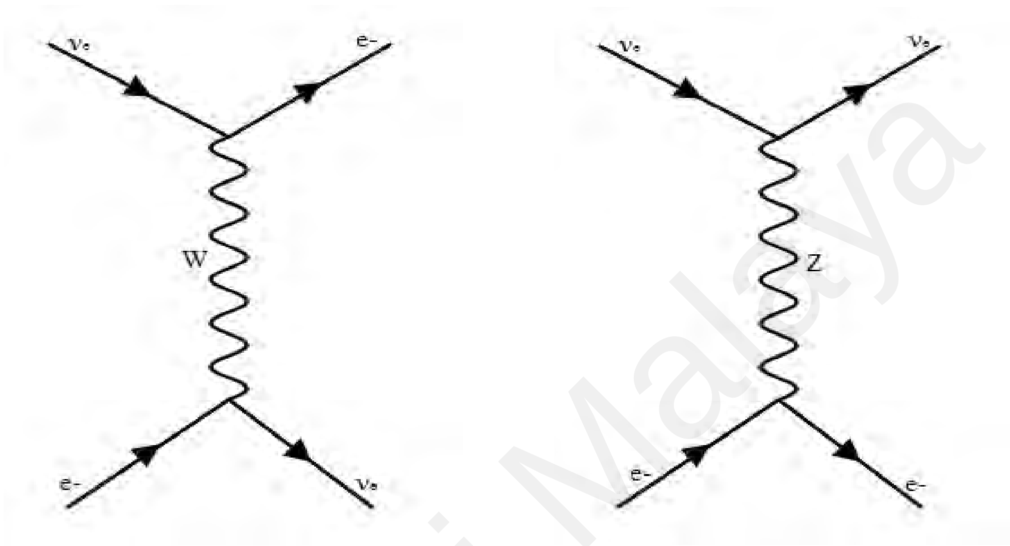

Figure 2.7: Feynman diagrams for neutrino-electron interactions through Charge-current (left) & Neutral-current (right) via W & Z propagators respectively.

$$\mathcal{L}_{eff}(\nu_e e^- \rightarrow \nu_e e^-) = -\frac{1}{\sqrt{2}} G_F\{[\overline{\nu_e}\gamma^\rho(1-\gamma^5)e][\bar{e}\gamma_\rho(1-\gamma^5)\nu_e] + [\overline{\nu_e}\gamma^\rho(1-\gamma^5)\nu_e][\bar{e}\gamma_\rho(g_V^l - g_A^l\gamma^5)e]\} \tag{2.24}$$

The Fermi constant $G_F = 1.16637 \times 10^{-5} GeV^{-2}$ and the two coefficients $g_V^l \; and \; g_A^l = {}^1/_2$ as constant values (Giunti & Kim, 2007). From this equation, it is clear that the second part of the right side represents NC contributions while the first part of the right side accounts for CC channel. However, considering only NC process, Equation 2.23, the effective Lagrangian for neutral-current terms becomes;

$$\mathcal{L}_{eff}(\nu_r e^- \rightarrow \nu_r e^-) = -\frac{1}{\sqrt{2}} G_F\{[\overline{\nu_r}\gamma^\rho(1-\gamma^5)\nu_r][\bar{e}\gamma_\rho(g_V^l - g_A^l\gamma^5)e]\} \tag{2.25}$$

It is important to note that these two processes and their effective Lagrangian are similar in structure and have some common quantities; for example, their cross-sections are proportional to Fermi constant $\left(\sigma \propto {G_F}^2 s\right)$. In principle, the differential cross-section, as given by Giunti and Kim (2007) is;

$$\frac{d\sigma}{dQ^2} = \frac{1}{\pi}{G_F}^2\left[g_1^2 - g_2^2\left(1 - \frac{Q^2}{2p_{\nu i}\cdot p_{ei}}\right)^2 - g_1 g_2 m_e^2 \frac{Q^2}{2(p_{\nu i}\cdot p_{ei})^2}\right] \tag{2.26}$$

However, in laboratory frame, the momentum $\vec{p}_{ei} = 0$ and assuming kinetic energy of a recoil electron T_e, the quantity of energy released is define by;

$$Q^2 = 2m_e T_e \tag{2.27}$$

Thus, the differential cross-section, Equation 2.26, becomes;

$$\frac{d\sigma}{dT_e}(E_\nu, T_e) = \frac{\sigma_0}{m_e}\left[g_1^2 + g_2^2\left(1 - \frac{T_e}{E_\nu}\right)^2 - g_1 g_2 m_e \frac{T_e}{{E_\nu}^2}\right] \tag{2.28}$$

where $g_1$and g_2 are different values which depend on the flavour of the neutrino, m_e is electron mass, $\sigma_0 \simeq 88.06 \times 10^{-46} cm^2$ and $E_\nu$is the energy of the incoming neutrino. We can go further to prove that for any given neutrino energy E_ν, there exist a maximum kinetic energy of the recoil electron T_e^{max}, and there also a minimum neutrino energy E_ν^{min} that produces a given kinetic energy. This maximum kinetic and minimum neutrino energies are respectively given by the following two equations;

$$T_e^{max}(E_\nu) = \frac{2E_\nu^2}{m_e + 2E_\nu} \tag{2.29}$$

$$E_\nu^{min}(T_e) = \frac{1}{2}T_e\left(\sqrt{1 + {}^{2m_e}/_{T_e}} + 1\right) \tag{2.30}$$

However, the minimum neutrino energy takes two different values; for $T_e \ll m_e$, $E_\nu^{min} \simeq \sqrt{2m_eT_e/2}$ while for $T_e \gg m_e$; $E_\nu^{min} \simeq T_e + m_e/2$. We can simply integrate Equation 2.28 to get the total cross-section as follows;

$$\sigma = \frac{\sigma_0}{m_e}\int\left[g_1^2 + g_2^2\left(1-\frac{T_e}{E_\nu}\right)^2 - g_1g_2m_e\frac{T_e}{{E_\nu}^2}\right]dT_e \tag{2.31}$$

We could, however, notice that it is impossible to calculate the neutrino-electron interactions without an initial value of kinetic energy of the recoil electron manifested. Hence, the total cross-section can be measured as a function of both initial kinetic energy of the recoil electron as well as neutrino energy. Assuming the initial kinetic energy is T_e^{ini}, Equation 2.31 can be rewritten as follows;

$$\sigma\left(E_\nu, T_e^{ini}\right) = \frac{\sigma_0}{m_e}\left[(g_1^2+g_2^2)\left(T_e^{max}-T_e^{ini}\right) - \left(g_2^2 + g_1g_2\frac{m_e}{2E_\nu}\right)\left(\frac{{T_e^{max}}^2 - {T_e^{ini}}^2}{E_\nu}\right) + \frac{g_2^2}{3}\left(\frac{{T_e^{max}}^3 - {T_e^{ini}}^3}{{E_\nu}^2}\right)\right] \tag{2.32}$$

where T_e^{max} is similar to Equation 2.30 and T_e^{ini} takes different initial values of the kinetic energy.

2.5.2 Neutrino oscillations

A neutrino flavour might change from its originally generated flavour to a different flavour by travelling certain distance; this phenomenon is called neutrino oscillation. Neutrino oscillations is remarked as a quantum mechanical phenomenon, which is described as dependant on the wave nature of neutrinos (Fantini et al., 2018). The interference of different massive neutrinos give rise to this oscillations and due to their very small mass difference they are produced and detected consistently (Giunti & Kim, 2007). Interest in neutrino oscillations has been intensified especially due to recent big discovery of its peculiar properties such as neutrino mixing and non-zero neutrino mass which actuated major change to standard model of particle physics in the last two decade and half. It is also among the hottest topics in elementary particle physics today. Observations of solar and atmospheric neutrinos over many years revealed the existence of neutrino oscillations and there has been many experiments which significantly improved the discovery of this important phenomenon. Examples of such experiments are Sudbury Neutrino Observatory (SNO) and Super-Kamiokande which their results provided revolutionary insight into the properties of neutrinos and in 2015 noble prize was given to Takaaki Kajita and Arthur B. McDonald for the discovery of neutrino oscillations, which shows that neutrinos have mass. The two types of neutrino oscillations are explained in the following sub-sections. A neutrino oscillations involving mixing of neutrino flavours is best described in the following equations (Mikheyev & Smirnov, 1986);

$$\nu_e = \nu_1 \cos\theta + \nu_2 \sin\theta \tag{2.33}$$

$$\nu_r = -\nu_1 \sin\theta + \nu_2 \cos\theta \tag{2.34}$$

where ν_e is the electron-neutrino and $\nu_r = \nu_\mu \; or \; \nu_\tau$ represents muon and tau neutrinos respectively. ν_1 and ν_2 are definite eigenstates with masses $m_1$and m_2 respectively. And θ is a mixing angle.

2.5.2.1 Vacuum Neutrino oscillations

Around the year 1976, the theory of plane-wave neutrino oscillations was introduced ably by Fritsch and Minkowski (1976), Bilenky and Pontecorvo (1976) and Eliezer and Swift (1976), which was later reviewed by Bilenky and Pontecorvo (1978) and Bilenky et al. (1999). According to these established theory, when a particular flavour of neutrino (α) having momentum $\vec{p}$, is created in a weak interaction by charged-current process from a charged lepton or antilepton, the eigenstates of the Hamiltonian of a massive neutrino states is given by;

$$H|\nu_k\rangle = E_k|\nu_k\rangle \tag{2.35}$$

with the energy eigenvalues for ultra-relativistic approximation defined as;

$$E_k = (\vec{p}^2 + m_k^2)^{1/2} \simeq E + \frac{m_k^2}{2E} \Longrightarrow E_k - E_j = \frac{\Delta m_{kj}^2}{2E} \tag{2.36}$$

The neutrino with a given mass will propagate with a Hamiltonian given by Equation 2.35 and evolve in time t as plane waves which can be describe by Schrödinger equation as;

$$H|\nu_k(t)\rangle = i\frac{d}{dt}|\nu_k(t)\rangle = E_k|\nu_k(t) \tag{2.37}$$

And the consequent time evolution of the plane wave's equation takes the form;

$$|\nu_k(t)\rangle = e^{-E_k t}|\nu_k\rangle. \tag{2.38}$$

When, for example, a particular neutrino flavour (say$|\nu_e\rangle$) is created at time t, the transition probability of this neutrino to oscillate into another (say into $|\nu_\mu\rangle$) can be given by;

$$P_{\nu_e\to\nu_\mu}(t) = \left|\langle\nu_\mu|\nu_e(t)\rangle\right|^2 = \frac{\sin^2 2\theta[1-\cos(E_2-E_1)t]}{2}. \tag{2.39}$$

By Equation 2.36, the transition probability becomes;

$$P_{\nu_e\to\nu_\mu}(t) = \frac{\sin^2 2\theta\left[1-\cos\frac{\Delta m_{12}^2}{2E}t\right]}{2} \tag{2.40}$$

But in neutrino oscillation experiments, the propagation time t cannot be measured, but it is represented by a source-detector distance L_(in metre), and hence for ultra-relativistic limit $t \simeq L$ such that $c = 1$, which leads to the standard oscillation probability;

$$P_{\nu_e\to\nu_\mu}(L,E) = \frac{\sin^2 2\theta\left[1-\cos\frac{\Delta m_{12}^2}{2E}L\right]}{2} \tag{2.41}$$

This is called neutrino oscillation with transition probability as periodic function of L/E, which shows that the source-detector distance and neutrino energy are quantities that depend on experiment that determine the phases of neutrino oscillations. While the phases are equally determined by neutrino squared-mass differences Δm_{kj}^2 (in eV^2), where $\sin^2 2\theta$ is amplitude of oscillations, and E is neutron energy measured in MeV or GeV. However, the oscillation length in vacuum can be define by;

$$L_\nu = \frac{4\pi E}{\Delta m_{12}^2} \tag{2.42}$$

Meanwhile, this oscillation length is $L_{\boldsymbol{\nu}} \lesssim L$, which shows that neutrino oscillations can be observed when oscillation length is not much greater than distance between the source and detector (Bilenky et al., 1999).

2.5.2.2 Neutrino oscillations in matter

Vacuum oscillations can be modified by matter, particularly for different amplitudes of neutrino flavours of forward elastic scattering on electrons and nucleons (Mikheyev & Smirnov, 1986). In 1978, Wolfenstein showed that massless neutrinos could also oscillate when it passed through matter. This happens due to change in potential and mixing angle which is, as the result of forward scattering of neutrinos with matter. The effective mixing angle in matter depends solely on density of matter and can therefore replace the vacuum mixing angle (Wolfenstein, 1987). Wu et al. (2016) provided that inside the Sun, for example, the propagation of neutrinos will experience a potential that grow out of the coherent forward scattering with particles in the medium which leads to what is now called Mikheyev-Smirnov-Wolfenstein (MSW) mechanism (Mikheyev & Smirnov, 1986; Wolfenstein, 1978). Today it is known that vacuum mixing angle which are suitable for neutrino oscillations in the sun is large although not to maximum level and it is also known that the transitions of flavour for solar neutrinos occur by this famous mechanism

(Giunti & Kim, 2007). It is worthy to note that neutrinos in matter are affected by both coherent and incoherent forward elastic scatterings, but the latter is extremely negligible in most situations. The evolution equation of a propagating neutrino in matter is affected by effective potentials resulting from interactions with medium by means of two weak; CC and NC scatterings processes. Let assume in the case of CC, the potential is V_{CC} when an electron neutrino propagates in an isotropic and homogeneous gas, the effective Hamiltonian for the CC scattering process can be defined by;

$$H_{eff}^{CC} = \frac{1}{2} G_F [\bar{\nu}_e(x)\gamma^{\rho}(1-\gamma^5)e(x)]\left[\bar{e}(x)\gamma_{\rho}(1-\gamma^5)\nu_e(x)\right], \tag{2.43}$$

And the charge-current potential, after some physical approximations, is given as functions of electron density of the medium, by;

$$V_{CC} = \sqrt{2} G_F N_e. \tag{2.44}$$

while, on the other hand, when in a low density and temperature astrophysical environment in which mainly electrons, protons and neutrons are dominated; the number of electrons and protons are equal and their NC potentials cancels, leaving only neutron contributions given by

$$V_{NC} = -\frac{1}{2}\sqrt{2} G_F N_n. \tag{2.45}$$

The constant $\sqrt{2}G_F \simeq 7.63 \times 10^{-14} \frac{eVcm^3}{N_A}$ will rendered the two potentials very small, where G_F is Fermi constant and N_A is Avogadro's number. The transition probability is density dependant and changes with time. For constant matter density, the transition probability changes from that of the vacuum oscillations with only replacing the mixing angle and squared-mass difference from the vacuum case to matter. However, for nonconstant density of matter, the transition is adiabatic and the oscillation length in matter changes to:

$$L_M^{osc} = \frac{4\pi E}{\Delta m_M^2} = \left(\frac{L_\nu}{\sqrt{\left(1-2\left(L_\nu/_{L_0}\cos 2\theta\right)+\left(L_\nu/_{L_0}\right)^2\right)}} \right), \tag{2.46}$$

However, $L_0 = 2\pi/\sqrt{2}G_F n_e$. Thus, we can see that the MSW effect is described based on the ratio L_ν/L_0 and the oscillations length in matter affects the survival probability as follows; for $L_\nu/L_0 = \cos 2\theta_M$, the maximum mixing is called MSW resonance, while for $L_\nu/L_0 \ll 1$, matter effects are in-essential and the probability is similar to the vacuum transition probability.

2.5.3 Stopping power of matter for Neutrino

In the calculations of total neutrino energy-loss in a massive star, the radius of the star can be multiplied by stopping power which is a function of neutrino energy and can be assumed constant. Assuming the neutrino-electron cross-sections with effect of neutrino oscillations is known, as given by Sulaksono and Simanjuntak (1994), we can integrate the cross-section to get the stopping power of matter for neutrinos as follows;

$$-\left(\frac{dE}{ds}\right) = \frac{G_F^2 m_e N_e}{2\pi}\left[P_e\left[A_e\frac{(Q_{m_e}^2-\eta^2)}{2} + B_e\frac{(Q_{m_e}^3-\eta^3)}{3} + C_e\frac{(Q_{m_e}^4-\eta^4)}{4}\right] - (P_e-1)\left[A_\tau\frac{(Q_{m_\tau}^2-\eta^2)}{2} + B_\tau\frac{(Q_{m_\tau}^3-\eta^3)}{3} + C_\tau\frac{(Q_{m_\tau}^4-\eta^4)}{4}\right]\right] \tag{2.47}$$

where A_i, B_i and $C_i (i = e, \tau)$ are constants, with their values depending on whether effect of neutrino oscillations or neutrino mass is considered. For simplicity, we refer the reader to Sulaksono and Simanjuntak (1994) for explicit expressions of these constants. In the above Equation 2.47; $N_e$is electron density, $\eta = \left(2N_e e^2/m_e\right)$ is the Plasmon energy of electrons in the star and $Q_m = 2m_e\left(E_\nu^2 - M_\nu^2\right)/\left(M_\nu^2 + m_e^2 + 2m_e E_\nu\right)$, is the maximum energy transferred to electron from neutrino of mass M_ν(which was set to be zero in Equation 2.47).

2.5.4 Neutrino flavour transformation

Neutrinos can undergo flavour oscillations in both vacuum and material medium. The phenomena of neutrino flavour transformation is a link of two exciting developments: the successful achievements in experimental neutrino physics and magnificent progress of both astronomy and astrophysics (Duan et al., 2010). The propagation of a particular flavour of neutrinos through a medium (vacuum or matter) to reach the Earth, will affect the neutrino spectra by transitional change of the initial flavour into an entirely different one, and has potential of mixing the spectral features and time of one flavour with those of another (Wright et al., 2017). This transformations is mainly caused due to oscillations of neutrino flavour as neutrinos propagates through stellar atmosphere and due to neutrino vacuum propagation between supernova and Earth, which resulted in quantum de-coherence on neutrino journey to the Earth (Wright et al., 2017a; Wright et al., 2017b; Wright et al., 2016). However, this de-coherence is caused as a result of large propagation distance which is greater than coherence length (Giunti et al., 1998). The key quantities for this flavour transformations are material density and electron fraction of the medium by which neutrinos propagates (Wolfenstein, 1978).

Let us consider a system of 3-flavour neutrino oscillations $\left(\nu_e, \nu_\mu, \nu_\tau\right)$ having neutrino mass squared differences(Δm_{ea}^2), the evolution matrix $S(x)$ which described the neutrino oscillations can be given, in form of (X) basis, by a Schrödinger equation

$$i\frac{dS^{(XX)}}{dr} = H^{(X)}S^{(XX)} \tag{2.48}$$

Where the Hamiltonian $H^{(X)}$ is defined by;

$$H^{(X)} = \frac{V}{2}\begin{pmatrix} 1 & 0 \\ 0 & -1 \end{pmatrix} + \delta \begin{pmatrix} -\cos 2\theta & \sin 2\theta \\ \sin 2\theta & \cos 2\theta \end{pmatrix} \tag{2.49}$$

In this term, the matter-induced potential is $V(X) = \sqrt{2} G_F N_e(x)$. And $\delta = \Delta m^2/4E$. Therefore, the evolution matrix relating state of neutrinos in basis (X) at some initial position r_1 to another state with possibly different basis (Y) at r_2, can be denoted by $S^{(YX)}(r_1, r_2)$. This defines the transition probability as probability for state x in the (X) basis which is positioned at r_1, to be in a different basis (Y) which is positioned at r_2, this can be expressed as;

$$P_{yx}^{(YX)} = \left|S_{yx}^{(YX)}\right|^2 \tag{2.50}$$

The only difference in the transition probability of antineutrinos to that of neutrinos is by denoting the transition probability with an over bar. The bases (X) and (Y) stands for flavour basis which contains basis states $(\nu_e, \nu_\mu,\ and\ \nu_\tau)$ and matter bases or simply referred to mass basis in vacuum that has (ν_1, ν_2, ν_3) basis states (Bethe, 1986). Hence, we can expressed neutrino transition probability, for example, by $P_{ij}^{(mm)} = P(\nu_j \to \nu_i)$, which is for a particular neutrino at state j in matter basis to be detected at state i. However, the mixing matrix U_V is given by Maki-Nakagawa-Sakata (MNS) matrix U, given by:

$$|\nu_\propto\rangle = \sum_I U_{\alpha i}^* |\nu_i\rangle \tag{2.51}$$

where $\alpha = e, \mu, \tau$ and $i = 1,2,3$ are flavour states and mass eigenvalues respectively, $U_{\alpha i}$ are elements of unitary transformation matrix which has four free parameters, namely; three mixing angles, $\theta_{12}, \theta_{23}, \theta_{13}$ and a CP-violating phase δ_{CP}. The mixing angles defines a unitary matrix for mixing of states,U_{ij}, with c_{ij} and s_{ij} are cosine and sine of the appropriate mixing angle θ_{ij}. The individual matrices can be given as;

$$U_{12} = \begin{pmatrix} c_{12} & s_{12} & 0 \\ -s_{12} & c_{12} & 0 \\ 0 & 0 & 1 \end{pmatrix}, \tag{2.52}$$

$$U_{13} = \begin{pmatrix} c_{13} & 0 & s_{13}e^{-i\delta_{cp}} \\ 0 & 1 & 0 \\ -s_{13}e^{-i\delta_{cp}} & 0 & c_{13} \end{pmatrix}, \tag{2.53}$$

$$U_{23} = \begin{pmatrix} 1 & 0 & 0 \\ 0 & c_{23} & s_{23} \\ 0 & -s_{23} & c_{23} \end{pmatrix}, \tag{2.54}$$

These three equations can be used to describe mixing between neutrino flavours consisting of two mass states (Cherry, 2012), and they can also form a full MNS matrix (Duan & Kneller, 2009) given by the following parameterisation;

$$U_V = U_{23}U_{13}U_{12} = \begin{pmatrix} c_{12}c_{13} & s_{12}c_{13} & s_{13}e^{-i\delta_{cp}} \\ -s_{12}c_{23} - c_{12}s_{23}s_{13}e^{i\delta_{cp}} & c_{12}c_{23} - s_{12}s_{23}s_{13}e^{i\delta_{cp}} & c_{13}s_{23} \\ s_{12}s_{23} - c_{12}s_{13}c_{23}e^{i\delta_{cp}} & -c_{12}s_{23} - s_{12}s_{13}c_{23}e^{i\delta_{cp}} & c_{13}c_{23} \end{pmatrix} \tag{2.55}$$

However, in Equation 2.48, the Hamiltonian represent the sum of two terms: a vacuum term H_V and a matter term H_M. These are explained in the following subsections.

2.5.4.1 Vacuum Hamiltonian

The oscillations of neutrino flavour in vacuum originate from the fact that weak interaction or flavour eigenstates for neutrinos are not concurrent with their mass or energy eigenstates. The neutrino is created in a pure flavour state by weak interaction and is in a superposition of mass eigenstates. The different eigenstates which is arising from neutrino propagation via space will build up a quantum mechanical phase at different rates, which is a manifestations of distinct momenta with respect to each mass eigenstates for a single neutrino (Cherry, 2012). These eigenstates are expressed by MNS matrix U, which is given in Equation 2.55. In solving the Schrödinger equation, the Hamiltonian in vacuum for flavour basis is a single matrix H_V which is dependent on particular basis and neutrino energy$E$. Assuming the three neutrino states has masses m_1, m_2, m_3, the vacuum Hamiltonian in the flavour basis can be determined by;

$$H_V^f = \frac{1}{2E} U_V \begin{pmatrix} m_1^2 & 0 & 0 \\ 0 & m_2^2 & 0 \\ 0 & 0 & m_3^2 \end{pmatrix} U_V^\dagger \tag{2.56}$$

However, for corresponding antineutrinos, the vacuum Hamiltonian $\overline{H}_V$ is by taken a simple complex conjugates of H_V.

2.5.4.2 Matter Hamiltonian

The Hamiltonian in matter comes because of a difference between electron flavour neutrinos/antineutrinos interaction with medium, with that of muon and tau flavours. The vacuum Hamiltonian H_V is added with matter Hamiltonian H_M:

$$H = H_V + H_M \tag{2.57}$$

And the interaction is best described by an effective potential that leads to Hamiltonian given by;

$$H_M^f = \sqrt{2} G_F n_e \begin{pmatrix} 1 & 0 & 0 \\ 0 & 0 & 0 \\ 0 & 0 & 0 \end{pmatrix} \tag{2.58}$$

where $n_e$is electron number density which can be expressed as $n_e = Y_e n_N$, for which Y_e is electron fraction and n_N is nucleon density which are both provided by simulation. Hence, we can say that neutrino flavour transformation is dependent on the density of the material and its electron fraction. However, the antineutrino matter Hamiltonian is $\overline{H}_M = -H_M$. Meanwhile, the density of the high-density MSW resonance, ρ_{high}^{MSW}, can be determined from, assuming two-flavour approximation;

$$\rho^{MSW} = \frac{m_N}{\sqrt{2} G_F Y_e} \left| \frac{\delta m^2 \cos 2\theta}{2E} \right| \tag{2.59}$$

where m_N is nucleon mass. From this equation, in high-density MSW, δm_{32}^2 is used for mass splitting δm^2 in the formula and θ_{13} for mixing angle θ. While in case of low-density MSW resonance, ρ_{low}^{MSW}, we use δm_{12}^2 for mass splitting δm^2 and θ_{12} for the mixing angle θ.

2.5.4.3 Neutrino self-interaction potential

During the supernova explosions, neutrino emission become very intense such that interactions between neutrinos begin to manifest a substantial impact in their flavour evolutions. Hence, the need to include the contribution of neutrino self-interaction to the Hamiltonian of neutrino flavour oscillations is sought. The Hamiltonian of neutrino self-interaction possesses the same order of magnitude as in matter potential. In 1992, Pantaleone (1992) derived the correct neutrino forward coherent scattering, or neutrino self-interaction Hamiltonian which was then applied to the study of neutrino transformations in early universe (Pantaleone, 1995). However, this flavour transformation was later found to be significant in supernova and may have greater influence on electron fraction in neutrino driven wind (Yang & Kneller, 2018). A details review on neutrino self-interaction has been provided by many authors (Duan et al., 2010; Duan & Kneller, 2009; Mirizzi, 2016). Meanwhile, in PISN the neutrino densities are very low, and the matter density is much less than the one finds in CCSNe, and hence, the neutrino self-interaction is obviously doubtful and might be ignored. This situation that self-interaction potentials becomes many orders of magnitude lower than the matter or vacuum Hamiltonian, was later confirmed by Wright et al. (2017a), and can therefore be ignored in calculating neutrino flavour evolution. It is now clear that neutrino self-interaction potential is strongly dependent on position and direction of propagation of the test neutrino. On this note, two important conditions are proposed (Yang, 2018) to be sought for in determining neutrino self-interaction potential;

I. The momentum vector and spatial coordinates of the test neutrino be identified.

II. The content of the neutrino flavour and fluxes of all neutrino beams emanating from surface of the neutronsphere which is captured by the test neutrino are known.

Another constraint to determination of neutrino self-interaction potential is due to self-consistency requirement where evolution history of the neutrinos are expected to be on record and should be evolved simultaneously. This is perhaps, almost impracticable due to computational limits (Yang, 2018). To address these weighty challenges, Duan et al. (2006) proposed a "BULB model" that can solve the self-consistent neutrino flavour transformations, especially in supernova environments.

(a) ***Neutrino bulb model***

The neutrino bulb model has been widely used in various supernova problems and has provided an important insights on the change of perception of supernova neutrinos. The model is an approximation of physical and geometrical conditions found in the after-shock supernova. It comprises of a neutrino emission source in spherical geometry (the neutrino bulb) and neutrino beams originating from the bulb. The characteristic properties of the bulb model can be summarised as follows:

I. The model is spherically symmetric.

II. The neutrino flux observed at any point is cylindrically symmetric.

III. The neutrino flavour eigenstates are stationary on the surface of the neutron sphere.

With these numerous symmetries, as illustrated in Figure 1 by Duan et al. (2006), the neutrino self-interaction Hamiltonian can be derived. For simplicity, we would like to refer the reader to Equation 1.80, by Yang (2018), for complete expression of neutrino self-interaction Hamiltonian.

2.5.4.4 Matter basis transformation probabilities

The basis where eigenvalues of the Hamiltonian $H = H_V + H_M$ appears on the diagonal is referred to as matter basis. To remove the trivial mixing in flavour basis, the neutrino transformation calculations must be undertaken in matter basis (Wright et al., 2017b). This is achieved by arranging the eigenvalues in a manner by which the masses appear in vacuum Hamiltonian, this ordering is also similar for antineutrinos (Wright et al., 2017a). Matter basis is significantly important to use over others because in adiabatic evolution, the evolution matrix is close to diagonal with constant transition probabilities. The transition probabilities for a neutrino which is in matter basis and initially at j state to be detected after neutrinos have propagated through the *SN*, at *i* state, will be a function of neutrino mass orderings, line of sight and the epoch. This can be given by:

$$P_{ij}^{(m)} = P\left(\nu_j^m \rightarrow \nu_i^m\right) \tag{2.60}$$

where the transition probabilities between states ν_j and ν_i are approximately one for $j = i$ and zero for $j \neq i$, which is also similar in the case of antineutrinos (Wright et al., 2017a).

2.5.4.5 Flavour basis transition probabilities at Earth

The de-coherence of neutrino wave packet are accounted for after propagation of neutrinos through the star as they embark their journey to the earth and, once, the oscillation probabilities of the matter basis are known(Wright et al., 2017a; Wright et al., 2017b). For a neutrino which emitted as a particular flavour (α) in the SN, to be detected as another flavour (β) at the Earth, the probability is given by:

$$P_{\beta\alpha} = \sum_j \left|U_{V,\beta J}\right|^2 P_{J\alpha}^{(mf)}(R_*, R_0). \tag{2.61}$$

In this equation, R_0 stands for radius of neutrino production near the centre of the SN, R_* is radius of outer edge of the SN. Similarly, the survival probabilities of the antineutrino favour basis is $\bar{P}_{\beta\alpha}$. These two probabilities are from evolution matrix and as such, they are different from transition probabilities earlier discussed.

2.5.4.6 The neutrino flux at Earth

A neutrino detector at Earth will see the neutrino flux:

$$F_\alpha = \frac{1}{4\pi d^2} \sum_\beta P_{\alpha\beta}(E) \Phi_\beta(E). \tag{2.62}$$

where $\Phi_\beta(E)$ is flavour β differential spectrum at point of emission, and d is the supernova distance. These neutrino flux is calculated by combination of particular flavour basis oscillation probabilities and neutrino emission spectra (Wright et al., 2017a).

2.6 Chapter Summary

This chapter begins with review on phenomenology of massive stars; from formation, evolution and fate to their ultimate death. Modules of stellar evolution is reviewed in section two of this chapter. This include evolution equations, rotation in stellar evolution and mass loss. In the proceeding sections, detail review on nuclear reactions involve in stellar evolution is given, with emphasis on reactions taking place in massive stars. The section that followed, reviewed the initial mass of progenitor stellar models that would encounter instability region. And finally, the chapter conclude with review on neutrino processes in massive stars. In the last subsections, we discuss neutrino-electron interactions, neutrino oscillations in massive stars. And closed the chapter with neutrino flavour transformation.

CHAPTER 3: METHODOLOGY OF RESEARCH

3.1 Introduction

In accordance with objectives of this research, this work is intended to investigate the characteristic dynamics of electron-positron pair-production and neutrino cooling processes involved in the instability regions of some selected mass range of very-massive stars. This processes which are threshold mechanisms that appear as a result of photon-photon, photon-particle, and particle-particle interactions are vital in understanding the final fates of massive stars. Of course, as a theoretical work, this research does not involve any experimental activity.

3.2 Stellar Models and Input Physical Parameters

Since electron-positron pairs are produced in late stages of stellar evolution (Woosley et al., 2002), this work focuses on all burnings beyond core hydrogen and helium (advanced burning stage). The data grids of evolutionary progenitor models considered are 120, 150, 200, 300 and 500M$_\odot$ which are taken from Yusof et al. (2013). From the work by Yusof et al. (2013), the 120, 150, 200, 300 M$_\odot$ and 500 M$_\odot$ models at $Z = 0.006$ (LMC) evolved with rotation, while 120, 150, 500 M$_\odot$ models evolved without rotation. These models were evolved from zero-age main-sequence (ZAMS), through at least oxygen burning, using Geneva evolution code (GENEC) (Eggenberger et al., 2009), which is used to solve most massive stars (R136a1) observed today (Crowther et al., 2010). This code, in its latest developments, has prescription for both rotating and magnetic fields included (Eggenberger et al., 2009; Ekström et al., 2012). According to Yusof et al. (2013) the explosion phase of these progenitors are followed by end of core helium burning through explosions, using KEPLER Code (Weaver et al., 2017). The KEPLER code is a stellar evolution/explosion code containing detailed treatment of nuclear burning processes incorporated with an implicit hydrodynamics and is capable of completely studying the evolution of massive and supermassive stars, supernovae, hydrostatic and explosive nucleosynthesis (Weaver et al., 2017). Additional details of evolution, physical input parameters and explosion calculations are reported by Yusof et al. (2013). However, Yusof et al. explained that the final fates of these models is predicted from outcomes of simulations with the KEPLER code and the simulations showed that indeed 150 $M_{\odot}$ and 200 $M_{\odot}$ rotating models in SMC and the 500$M_{\odot}$ rotating and non-rotating models in LMC produced electron-positron pairs and ended as PISNe (Whalen et al., 2014b) . This further indicates that carbon-oxygen (CO) core mass is very suitable to make an estimate of whether these models produce PISNe or not? (Which is a method that has been used in various studies of very-massive stars for similar demonstration of fates of stars with same CO core (Bond et al., 1984; Chatzopoulos & Wheeler, 2012a; Heger & Woosley, 2002)). Carbon-oxygen core masses of the rotating models are 32.67, 38.44, 42.36, 44.96 and 73.12 $M_{\odot}$ for 120, 150, 200, 300 500 $M_{\odot}$ respectively. While for non-rotating models the Carbon-oxygen core masses are 43.85, 47.56 and 92.55 $M_{\odot}$ for 120, 150 and 500 $M_{\odot}$ respectively. However, the helium-core masses for the rotating models are 39.25, 45.58, 51.02, 54.04 and 74.75 $M_{\odot}$ respectively, while for non-rotating models, the helium-core masses are 54.11, 59.59 and 94.56 $M_{\odot}$ for 120, 150 and 500$M_{\odot}$ respectively, which shown in Tables 3.1 and 3.2. This clearly shows that these models are either at near end or lower end of the instability mass range. Radiative line-driven winds from Vink et al. (2001) was used in the work by Yusof et al.(2013) for mass loss prescription. The nuclear reaction rates are taken from Nuclear Astrophysics Compilation of Reaction Rates (NACRE) database (Angulo et al., 1999), and effects of these rates in stellar evolution are well explained in literature, see for example Ekström et al. (2012). The models were evolved with critical rotation (0.4) and rotation set to zero at ZAMS.

Table 3.1: Properties of stellar models used in this work and compared with others, showing initial mass, final mass, initial metallicity, velocity, ρ_c^{max} & T_c^{max} maximum central density and temperature, and finally He-core and O-core mass.

M_i [M⊙]	M_f [M⊙]	Z_{ini}	V_{ini}/V_{crit}	log ρ_c^{max} [g cm^{-3}]	log T_c^{max} [K]	He-core [M⊙]	CO-core [M⊙]	Fate
With rotation (Yusof et al., 2013)								
120	39.25	0.006	0.4	7.99	9.76	39.25	32,67	BH/CCSN
150	45.58	0.006	0.4	6.17	9.44	45.58	38.44	BH/CCSN
200	51.02	0.006	0.4	7.90	9.79	51.02	42.36	BH/CCSN
300	54.04	0.006	0.4	6.02	9.39	54.04	44.96	BH/CCSN
500	74.75	0.006	0.4	5.92	9.35	74.75	73.12	PISN
150	106.74	0.002	0.4	5.53	9.29	107	93	PISN
200	128.91	0.002	0.4	5.48	9.30	129	124	PISN
Without rotation (Yusof et al., 2013)								
120	54.11	0.006	00	5.59	9.22	54.11	43.85	BH/CCSN
150	59.59	0.006	00	5.35	9.17	59.59	47.56	BH/CCSN
500	94.56	0.006	00	4.52	9.01	94.56	9.55	PISN
Ref. (Wright et al., 2017a)								
150	-	0.001	00	-	-	-	65.7	PISN
250	-	0.001	00	-	-	-	126.7	PISN
Ref.(Kozyreva et al., 2014)								
150	94	0.001	00	6.25	9.54	72	64	PISN
250	169	0.001	00	6.69	9.71	121	110	PISN
Ref.(Chatzopoulos & Wheeler, 2012a)								
200	-	0.014	00	6.54	9.70	-	120	PISN

Summary of these selected models with their key properties are given in Table 3.1, and are compared with other reported results (Heger & Woosley, 2002; Kozyreva et al., 2014; Langer et al., 2007; Wright et al., 2017a). The first two columns in this table are initial masses and final masses (in $M_\odot$), third, fourth, fifth and sixth columns are initial metallicities, velocity, log of maximum central density (g cm^{-3}) and maximum central temperature (K) encountered due to the pair-production instability respectively. The remaining columns seventh, eighth and ninth represents helium core mass ($M_\odot$), oxygen core mass ($M_\odot$) and finally, fates of the models observed by various hydrodynamic codes. The increase in rotation brings about a chemically homogeneous evolution and produced higher oxygen core mass, which is necessary for pair-production in the core of the stars. Thus higher degrees of rotation brings a star much closer to density-temperature region, where adiabatic index is below 4/3, this trend was noted by Chatzopoulos and Wheeler (2012a). The 150 $M_\odot$, 200 $M_\odot$, and 500 $M_\odot$ rotating models fully entered the pair-instability region except for non-rotating 500 $M_\odot$ only its final mass almost collapses before reaching the pair-instability region, this might be due to non-rotational effects which are explained in chapter five. In all the induced rotating models, mass of oxygen core is shrinking by degrees of rotation, such that rotating models are more luminous than non-rotating and nucleosynthesis alter the rotation occurring in the stars. This may be due to reduction in the effective gravity of centrifugal force during the rotation, and due to hydrogen burning core, when main sequence becomes enlarged with rotationally-induced chemical mixing.

Electron-positron pairs are produced in late stages of stellar evolution (Woosley et al., 2002), this is why in this work, we focus on burnings beyond core hydrogen and helium. In Table 3.2, we summarized the main properties of the models, after been induced by pair-production instability. From this table, Eddington limit (Γ_{Edd}) in the pair-production region of all models are within theoretical limit at which radiation pressure of photon-emitting star would exceed its gravitational attraction. The maximum Eddington recorded values for 120, 150, 200, 300 and 500 $M_\odot$ rotating models at LMC are 0.83, 0.86, 0.87, 0.88 and 0.92 respectively. While for non-rotating models, these values are 0.97, 0.97 and 0.98 for the 120, 150 and 500 $M_\odot$ non-rotating models respectively, as shown in Table 3.2. There are several factors that affect this values; for example, the Eddington factor in rotating models depends on metallicity of the star, such that increase in metallicity reduce the value of the Γ_{Edd} and this induces low metallicity models to become unstable. Other factors that affect the Eddington parameters are rotation and mass loss. The succeeding evolution, after the helium burning as finished off by helium cores, is very rapidly such that the mass loss is insignificant. Subsequently, the cores of the stars are mostly ^{16}O, and some amount of ^{12}C and ^{20}Ne. the fact that the ^{12}C is abundantly low and the energy release from the ^{20}Ne burning which is negligible, rendered their burning fuels to have insignificant effects, and hence, the stars are fundamentally oxygen cores.

3.3 Equation of State

Every stellar model require the construction of a thermodynamic variables (equation of state) which relate the internal energy and pressure as functions of density, temperature, and composition. Similarly, several thermodynamic derivatives are required for evolving these models realistically. The equation of state (Henceforth EoS) is a generalized-mathematical thermodynamic relation describing the state of matter under a given set of physical conditions. The most common physical quantities in stellar models are absolute temperature T, density ρ, and chemical composition X_i. However, only by means of EoS, the rest of the useful functions of thermodynamic consequence are known, such as pressure $P(T, \rho, X_i)$, specific energy $E(T, \rho, X_i)$, or entropy $S(T, \rho, X_i)$.

Table 3.2: Models' physical properties (taken from Yusof et al. (2013)) showing maximum values of initial mass M_{ini}, metallicity z_{ini} and the third column is final mass followed by age, luminosity, mass loss and central density and temperature respectively. The 9th, 10th and 11th columns are ZAMS effective temperature, equitorial velocity, and Eddington factor respectively.

M [$M_\odot$]	Z_{ini} [$Z_\odot$]	M_{fin} [$M_\odot$]	Age x10^6[yr]	log [$L_\odot$]	Mass loss [$M_\odot/yr$]	log ρ_c [g cm^{-3}]	Log T_c [K]	log T_{eff} [K]	V_{eq} [Kms^{-1}]	Γ_{Edd}
With Rotation										
120	0.006	39.25	3.48	6.33	-4.48	7.99	9.75	4.89	39.35	0.83
150	0.006	45.58	3.17	6.40	-4.44	6.17	9.44	4.90	36.30	0.86
200	0.006	51.02	2.91	6.46	-4.42	7.90	9.79	4.90	95.12	0.87
300	0.006	54.04	2.63	6.49	-4.42	6.02	9.39	4.91	0.00	0.88
500	0.006	74.75	2.39	6.65	-4.21	5.92	9.35	4.87	0.02	0.92
Without Rotation										
120	0.006	54.11	3.00	6.53	-4.48	5.59	9.22	3.99	0.00	0.97
150	0.006	59.59	2.85	6.58	-4.41	5.35	9.17	4.32	0.00	0.97
500	0.006	94.56	2.18	6.78	-4.28	4.52	9.01	4.44	0.00	0.98

In massive stars and at the end of the Fe-burning, there is no nuclear burning that can proceed to create the pressure needed to hold the star against gravitational collapse. The star at this situation, will begin to implode its core into a dense mater within a second into a neutron star. Hence, the EoS of the central region during the stellar collapse is obviously important in determining the characteristics and the outcomes of the implosion. Only at extreme densities (> 10^{11} g cm^{-3}), the equation of states describing the relations of energy and pressure in massive stars, to temperature, density, and composition is straightforward (Woosley et al., 2002). The state of matter in massive stars, and in most of astrophysical objects, are described by the ideal gas law; $PV = Nk_BT$. In this equation, P is the gas pressure, V the volume occupied by the gas, N is the total number of particles in the centre of the massive star, and k_B is Boltzmann's constant. However, the number density is $\rho = \frac{N\mu m}{V}$, where μ is the mean molecular weight in unit of the particles' mass m. Thus, the EoS can be given by $P = \frac{k_BT}{\mu m}\rho$.

3.3.1 Distribution Functions

The distribution function for different forms of particles determines number density of the particles in dimensional coordinates and momenta. Knowing this function for a particular gas, all other thermodynamic variables may be derived with respect to density, temperature, and composition of the gas. In quantum statistics, when a group of indistinguishable particles is in thermal equilibrium, there is a momentum of distribution given by;

$$f(\vec{p})d^3\vec{p} \; = \frac{g}{h^3}\left[exp\left(\frac{E(p)-\mu}{k_BT}\right) \pm 1\right]^{-1} d^3\vec{p} \tag{3.1}$$

However, the average number of particles is

$$n_{av} = \frac{g}{\exp\left[\frac{E(p)-\mu}{k_BT}\right] \pm 1} \tag{3.2}$$

where $E(p) = (m^2c^4 + p^2c^2)^{1/2}$ is the kinetic energy of the particle, the upper sign (positive) refer to fermions (half-integer spin particles), and is called Fermi-Dirac distribution, and the lower sign (negative) is for bosons (zero or integer spin particles), and is called Bose-Einstein distribution. g is a degeneracy factor, which is the number of spin states, the particle can have (1 for neutrinos, 2 for charged particles and photons, and 6 for quarks). μ is the chemical potential and is related to the number density and temperature of the particles, and $c = 3 \times 10^5\ kms^{-1}$ is the speed of light, $k_B = 1.38 \times 10^{-16}\ erg\ K^{-1}$ is Boltzmann constant, T is temperature and $h = 2\pi \times \hbar = 6.63 \times 10^{-27}\ g\ cm^2\ s^{-1}$ is Planck's constant. And the physical number density of particles in unit volume is;

$$n(p)dp = \frac{4\pi g p^2}{h^3 \exp\left[\frac{E(p)-\mu}{k_B T}\right] \pm 1} dp \tag{3.3}$$

This is between the momenta p and $p + dp$, with a surface $4\pi p^2$ and thickness dp. Hence the number density of particles with all momenta is defined by integrating over all momentum space;

$$n = \int_0^\infty n(p)dp \tag{3.4}$$

Since the particles can be relativistic, ultra-relativistic and non-relativistic, the correct form of the total energy of the particle must be equal to the sum of the rest mass energy and the kinetic energy of the particle, given by;

$$E = E(p) + E_0 = (m^2c^4 + p^2c^2)^{1/2} - mc^2 \tag{3.5}$$

Which when in non-relativistic limit ($pc \ll mc^2$), this equation becomes $E = \frac{p^2}{2m}$ and ultra-relativistic limit ($pc \gg mc^2$), it becomes $E = pc$.

Another physical quantity of importance here is particle velocity which is given by;

$$v = \frac{dE}{dp} = \frac{p}{m\left[1+\left(\frac{p}{mc}\right)^2\right]^{1/2}} \tag{3.6}$$

Such that, the two asymptotic limits gives, $v \approx \frac{p}{m}$ and $v \approx c = 1$ for non-relativistic and ultra-relativistic respectively. For an isotropic gas, the pressure, which is a flux of momentum across a unit surface, and integrated over all particles moving in all directions, can be given by;

$$P = \frac{1}{3}\int_0^\infty v(p)n(p)dp \tag{3.7}$$

Similarly, the internal energy of all particles in a unit volume can be calculated as;

$$E = \int_0^\infty E(p)n(p)dp \tag{3.8}$$

These Equations 3.1 – 3.8, described the generalized sets of relations needed in the construction of any form of equation of state.

3.3.2 Adiabatic Processes and Thermodynamic Functions

There are different processes taken place at a very high temperature and relatively low densities. An adiabatic process is one in which no heat is exchanged between a system and its surroundings. That is, the gain or loss of heat by conduction or radiation can be ignored in an adiabatic process. A measure of this process is the adiabatic index

$$\gamma = C_p/C_v \tag{3.9}$$

The adiabatic index γ takes values from 5/3, 7/5 to 4/3, for an ideal monoatomic, diatomic and polyatomic gas respectively.

Using laws of thermodynamics, and a similar equation for the internal energy, we can derive from the EoS the thermodynamic properties that are needed to describe the structure of a star, such as the specific heats, C_v and C_p, the adiabatic exponent and the adiabatic temperature gradient (Pols, 2011). As stated earlier, a stellar model require thermodynamic variables, such as pressure and internal energy, as functions of density, temperature and, composition to realistically evolve. Similarly, the thermodynamic derivatives are equally important for the evolution of not only the massive stars but many astrophysical events. However, the calculation of the thermodynamic derivatives is particularly difficult in situations where the relative concentrations of the stellar chemical composition does not change with respect to temperature and density of the stellar medium.

3.3.2.1 Specific Heats

The specific heats are the first derivatives encountered in thermodynamics and can be given by;

$$C_\alpha = \left(\frac{dQ}{dT}\right)_\alpha \tag{3.10}$$

where Q is amount of heat released by the star (in erg g^{-1}), such that specific heats are measured in units of (erg g^{-1} K^{-1}). However, the specific heats can be with respect to $\alpha = P, V$. From the thermodynamic law, the amount of heat is given by;

$$dQ = dE - \frac{P}{\rho^2} d\rho \tag{3.11}$$

Hence, Equation 3.10, becomes;

$$C_V = \left(\frac{dQ}{dT}\right)_\rho = \left(\frac{\partial E}{\partial T}\right)_\rho \tag{3.12}$$

While the other specific heat at constant pressure can be known from the thermodynamic relation;

$$C_p = \left(\frac{dQ}{dT}\right)_p = \left(\frac{\partial E}{\partial T}\right)_p + P\left(\frac{\partial V}{\partial T}\right)_p \tag{3.13}$$

and these two properties of stellar structure (Equation 3.12 and 3.13) are related by;

$$C_p - C_v = \left[\left(\frac{\partial E}{\partial V}\right)_T + P\right]\left(\frac{\partial V}{\partial T}\right)_p \tag{3.14}$$

However, for an ideal gas $PV = nRT$ and the first law $dQ = dE + PdV$ Equation 3.14 transform to;

$$C_p - C_v = nR \tag{3.15}$$

3.3.2.2 Adiabatic Derivatives

The requirement for the adiabatic condition, $dQ = 0$ imposes, through the first law of thermodynamics, some relation between the pressure, *P*, temperature, *T*, and the volume, *V*, and the thermodynamic response of a system to this adiabatic changes is measured by adiabatic derivatives. Two of these have special importance for stellar structure:

I. The adiabatic exponents γ_{ad} which measure the response of the pressure to adiabatic compression or expansion, or to a change in the density. It is defined as

$$\Gamma_1 = \left(\frac{d\ln P}{d\ ln\ \rho}\right) = \gamma_{ad} \tag{3.16}$$

If γ_{ad} is constant then $P\ \alpha\ \rho^{\gamma_{ad}}$ for adiabatic changes. This adiabatic exponent is however related to the dynamical stability of stars.

II. The adiabatic temperature gradient is defined as

$$\frac{\Gamma_2}{(\Gamma_2 - 1)} = \left(\frac{d\ln P}{d\ln T}\right) = \frac{1}{\nabla_{ad}} \tag{3.17}$$

It is, in fact, another exponent that describes the behavior of the temperature under adiabatic compression or expansion ($T\ \alpha\ P^{\nabla_{ad}}\ if\ \nabla_{ad}\ is\ constant$), which turns out to be important for stability against convection. and

$$\Gamma_3 - 1 = \left(\frac{d \ln T}{d \ln \rho}\right) \tag{3.18}$$

The general identity for the relationship between these adiabatic exponents is given by

$$\frac{\Gamma_3 - 1}{\Gamma_1} = \frac{\Gamma_2 - 1}{\Gamma_2} = \nabla_{ad} \tag{3.19}$$

In general, Γ_1 is important for determining the conditions of the dynamical instability of stars, similarly, Γ_2 and Γ_3 are important, respectively, in determining the conditions of the convective and Pulsational instability of stars. Unlike the exponent γ in the case of perfect gas, the Γ_i are not equal to the ratio C_p/C_v. The Γ_i depend on the equation of Degenerate gasses (Maeder, 2008).

3.4 Fermi-Dirac Equation of State

In massive stars, when the central temperature is very high, $kT >= mc^2$, electrons become relativistic and an energetically electron-positron pairs is produced. The distribution function of these electron-positron pairs is therefore given by Fermi-Dirac distribution. The thermodynamic variables of these relativistic fermions and anti-fermions are greatly important not only in massive stars, but many astrophysical situations. For example, the cores of the massive stars are supported in mechanical equilibrium by the pressure of relativistic electrons (Blinnikov et al., 1996). The prime motivation of this equation of state in massive stars, is electron-positron pair-production in the centres of the massive stars which together with neutrino energy-loss triggered an explosion that result to PISN. In general, for an ideal Fermi gas, the pressure equation for the fermions (electrons) can be define by

$$P_{e^-} = \frac{m_e c^2}{3\pi^2 \alpha^4}\left(\frac{m_e c}{\hbar}\right)^3 \int_0^\infty \frac{x^4 (x^2 - \alpha^2)^{-1/2} dx}{exp\left[(x^2 + \alpha^2)^{1/2} - \varphi\right] + 1} \tag{3.20}$$

where $\alpha = \frac{m_e c^2}{k_B T}$ is relativity parameter and $\varphi = \frac{\mu}{k_B T}$. And the integral is generalized a form of Fermi-Dirac integral which can be numerically approximated for any astrophysical application. For details about the numerical and analytic approximations of Fermi-Dirac integrals, see the references (Blinnikov et al., 1996; Chabrier & Potekhin, 1998; Johns et al., 1996; Potekhin & Chabrier, 2010). However, the number density for the fermions (electrons) is define by

$$n_{e^-} = \left(\frac{\partial P_{e^-}}{\partial \mu}\right)_T \tag{3.21}$$

And the energy and entropy are given by

$$E_{e^-} = -\frac{1}{\rho}\left[P_{e^-} + \alpha\left(\frac{\partial P_{e^-}}{\partial \alpha}\right)_{\varphi}\right] \tag{3.22}$$

$$S_{e^-} = \frac{1}{\rho}\left(\frac{\partial P_{e^-}}{\partial T}\right)_{\mu} \tag{3.23}$$

The expressions for pressure, number density, energy, and entropy for anti-fermions (positrons) are quite similar to these relations.

3.4.1 Degenerate Electrons

Since electrons are fermions; they must, therefore, obey the Pauli Exclusion Principle, for which they shall be distributed in such a way that each quantum state is fully occupied by one electron. This is limited up to certain energy level because for higher energies the quantum states are unoccupied. This type of electron distribution represents the zero temperature limit of the Fermi-Dirac distribution. The degenerate electrons are, therefore, cold gas electrons which have fallen into a lowest energy quantum states.

The number of electrons in a degenerate gas can be given by;

$$n = \int_0^{p_F} g_s \frac{n}{h^3} 4\pi p^2 dp = \frac{8\pi n}{3h^3} p_F^3 \tag{3.24}$$

For two independent spin states of electrons; $g_s = 2$. While the Fermi momentum p_F can be expressed in terms of electron density as;

$$p_F = \left(\frac{3n}{8\pi}\right)^{1/3} h \tag{3.25}$$

These two equations can simply prove the fact that; the de Broglie wavelength $\lambda = h/p_F$ of most energetic electrons in a degenerate gas is comparable with the inverse of the cube-square of the number density $1/n^3$. At a very high temperature $kT \geq mc^2$, the electrons are relativistic and an electron-positron pairs is produced by creating a new particle (positron-the anti-electron). Therefore, the distribution functions for both types of electrons must be written down. Having knowing the total number of electrons in the degenerate gas, the equation of state of this gas can be found from the expression of the internal energy. In the next section, we shall describe the equation of state for the electron-positron degenerate gas.

3.4.2 Equations of State for Relativistic Electron-Positron Pairs

In the relativistic limit, the photons inside the stars have Bose-Einstein distribution, while their chemical potential is zero. However, the pairs of electron-positron are in thermal equilibrium with the photons due to the annihilation and pair-production reactions. This must satisfy the equilibrium condition $\mu = \mu_{e^-} = -\mu_{e^+}$ where μ_{e-} and μ_{e+} are electron and positron chemical potentials respectively. The chemical potential for the electrons and positrons only differ by two rest mass energies

$$\mu_{e^-} = mc^2 \; and \quad \mu_{e^+} = \mu_{e^-} - 2mc^2 = -\mu_{e^-} \tag{3.26}$$

However, this condition does not mean that the electron and positron concentrations are equal, perhaps, at a lower temperature, the positron number is exponentially lower than the electrons by almost $exp\left(\frac{-\mu}{k_B T}\right)$. Furthermore, the total pressure of the electrons and positrons, both in equilibrium with matter and radiation is

$$P = P_{e^-} + P_{e^+} \tag{3.27}$$

The number densities of the electrons and positrons (Timmes & Swesty, 2000) are given by;

$$n_{e^\pm} = \frac{64\pi^4\sqrt{2}}{\hbar^3}(m_e c)^3 \propto^{3/2} F_n(\varphi, \alpha) \tag{3.28}$$

where;

$$F_n(\varphi, \alpha) = \int_0^\infty \frac{y^n(1+0.5\alpha y)^{1/2}}{1+e^{(y-\varphi)}} dy \tag{3.29}$$

is a special case of Fermi-Dirac integral. The values of this integral are calculated using an analytic approximation by Potekhin and Chabrier (2010). However, since high accuracy is needed, the values of the integral are also calculated (Timmes & Arnett, 1999) and the algorithm that preserves the thermodynamic consistency are interpolated, which are available at MESA (Paxton et al., 2010). So, the individual number density for free electron (Arnett, 1996; Fowler & Hoyle, 1964; Timmes & Arnett, 1999) can be;

$$n_{e^-} = \frac{64\pi^4\sqrt{2}}{\hbar^3}(m_e c)^3 \propto^{3/2} \left[F_{1/2}(\varphi, \alpha) + F_{3/2}(\varphi, \alpha)\right] \tag{3.30}$$

While for positron, the chemical potential must have the rest mass terms which was subtracted in the case of electrons, and therefore it is given by

$$n_{e^+} = \frac{64\pi^4\sqrt{2}}{\hbar^3}(m_e c)^3 \propto^{3/2} \left[F_{1/2}\left(-\varphi - {}^2/_\alpha, \alpha\right) + \alpha F_{3/2}\left(-\varphi - {}^2/_\alpha, \alpha\right)\right] \tag{3.31}$$

The chemical potential μ (which is the only unknown in this equation) can be found by applying the boundary condition for complete ionization of the matter present,

$$n_0 = n_{e^-} - n_{e^+} = N_a \frac{\rho Z}{A} = Z n_{ion} \tag{3.32}$$

where N_a is Avogadro's number and ρ, Z and A are the mass density, atomic number and atomic weight of the matter excluding electron-positron pairs. However, many methods can be used for this one-dimensional root finding. While absolute accuracy and thermodynamic consistency are primarily the major concern, Timmes EoS evaluated the Fermi-Dirac integrals and their derivatives with respect to the chemical potential and relativity parameter, whereas, the chemical potential was calculated using Newton-Raphson scheme to at least 15 significant figures (Timmes & Arnett, 1999). After finding the value for the chemical potential by the use of Newton-Raphson iteration method, the electron positron pressure,

$$P_{e^-} = \frac{128\pi^4\sqrt{2}}{3\hbar^3} m^4{}_e c^5 \alpha^{5/2} \left[F_{3/2}(\varphi,\alpha) + \frac{1}{2}\alpha F_{5/2}(\varphi,\alpha)\right] \tag{3.33}$$

Similarly, the positron pressure is

$$P_{e^+} = \frac{128\pi^4\sqrt{2}}{3\hbar^3} m^4{}_e c^5 \alpha^{5/2} \left[F_{3/2}\left(-\varphi - {}^2/_\propto, \alpha\right) + \frac{1}{2}\alpha F_{5/2}\left(-\varphi - {}^2/_\propto, \alpha\right)\right] \tag{3.34}$$

And the specific thermal energy of the electron can be given as

$$E_{e^-} = \frac{64\pi^4\sqrt{2}}{\rho\hbar^3} m^4{}_e c^5 \alpha^{5/2} \left[F_{3/2}(\varphi,\alpha) + \alpha F_{5/2}(\varphi,\alpha)\right] \tag{3.35}$$

While the specific thermal energy of the positron is

$$E_{e^+} = \frac{64\pi^4\sqrt{2}}{\rho\hbar^3} m^4{}_e c^5 \alpha^{5/2} \left[F_{3/2}\left(-\varphi - {}^2/_\propto, \alpha\right) + \alpha F_{5/2}\left(-\varphi - {}^2/_\propto, \alpha\right)\right] + \frac{2m_e c^2}{\rho} n_{e^+} \tag{3.36}$$

For the electron entropy;

$$S_{e^-} = \frac{{}^{P_{e^-}}/_{\rho} + E_{e^-}}{T} + \frac{\mu k N_{e^-}}{\rho} \tag{3.37}$$

While the positron entropy is

$$S_{e^+} = \frac{P_{e^+}/\rho + E_{e^+}}{T} + \frac{(\mu + 2/\alpha) k N_{e^+}}{\rho} \tag{3.38}$$

The total pressure is given by Blinnikov et al. (1996), which is used conveniently in relativistic electron-positron gas is,

$$P = P_{e^-} + P_{e^+} = \frac{m_e c^2}{12\pi^2}\left(\frac{m_e c}{\hbar}\right)^3 \left[\frac{1}{\alpha^4}\left(\frac{7\pi^4}{15} + 2\pi^2\varphi^2 + \varphi^4\right) - \frac{1}{\alpha^2}(\pi^2 + 3\varphi^2) + \frac{3}{2}\left(ln\frac{4\pi}{\alpha} + \frac{3}{4}\right) + \frac{2}{\pi}\int_{-1}^{1}(1 - x^2)^{3/2}\Psi_F(\varphi + \alpha x)dx\right] \tag{3.39}$$

where $\Psi_F(\varphi + \alpha x) = \sum_{k=0}^{\infty} \Psi_F^k(\varphi)\frac{\alpha^k x^k}{k!}$. Therefore, substituting this into Equation 3.39, and integrating over x, we get;

$$P = \frac{m_e c^2}{12\pi^2}\left(\frac{m_e c}{\hbar}\right)^3 \left[\frac{1}{\alpha^4}\left(\frac{7\pi^4}{15} + 2\pi^2\varphi^2 + \varphi^4\right) - \frac{1}{\alpha^2}(\pi^2 + 3\varphi^2) + \frac{3}{2}\left(ln\frac{4\pi}{\alpha} + \frac{3}{4}\right) + \frac{3}{2}\sum_{j=0}^{\infty}\frac{\alpha^{2j}}{2^{2j} j!(j+2)!}\Psi_F^{2j}(\varphi)\right] \tag{3.40}$$

However, the entire integral in this equation is has a very negligible contribution to the leading terms in the relativistic region, and so has negligible accuracy. The accurate expression is achieved by assuming the Chebyshev quadrature formula as ideal, and the exact relativistic formula is;

$$P = P_{e^-} + P_{e^+} = \frac{m_e c^2}{12\pi^2}\left(\frac{m_e c}{\hbar}\right)^3 \left[\frac{1}{\alpha^4}\left(\frac{7\pi^4}{15} + 2\pi^2\varphi^2 + \varphi^4\right) - \frac{1}{\alpha^2}(\pi^2 + 3\varphi^2) + \frac{3}{2}\left(ln\frac{4\pi}{\alpha} + \frac{3}{4}\right) + \frac{2}{5}\sum_{n=1}^{5}(1 - X_n^2)^2\Psi_F(Y_n)\right] \tag{3.41}$$

where $X_n = \cos\left[\frac{(2n-1)\pi}{10}\right]$ and $Y_n = \varphi + \alpha X_n$.

This total expression for the electron-positron pressure is accurate for an ideal Fermi gas and is true for any values of φ and α and any temperature and density, but it is practically acceptable in the relativistic region. It gives the complete expression for pressure in mass powers. The total number density of electron-positron pairs is

$$n_{e^-} - n_{e^+} = \frac{\alpha}{m_e c^2}\left(\frac{\partial P}{\partial \varphi}\right)_\alpha \tag{3.42}$$

and the total energy of the electron-positron pairs is;

$$E = E_{e^-} + E_{e^+} = -\alpha\left(\frac{\partial P}{\partial \alpha}\right)_\varphi - P - m_e c^2 N_a Y \tag{3.43}$$

while the total entropy of the pairs is

$$S = S_{e^-} + S_{e^+} = \frac{1}{T}[P + E - (n_{e^-} - n_{e^+})\mu] \tag{3.44}$$

The derivatives -to the first order- with respect to density and temperature, of the above equations for pressure, energy, and entropy must satisfy some thermodynamic identities (Equations 3.52 – 3.54) given in the section below. However, these thermodynamic derivatives are essentially needed in implementing a complete iteration scheme for solving thermodynamic convergence of various stellar evolution models. Meanwhile, the evaluation of these set of equations is confronted by extreme complexities. This is due to the excessive time consuming, the instability and lack of suitability of many computer codes that are commonly used in the direct calculation of the electron-positron physics in the EoS. One particular difficulty is the complexity that often arises when solving the many-body problems which describe the interactions between the constituents of the gas, and also, the behavior of the EoS with respect to the range of temperature and density, which evidently shows discontinuities in thermodynamic variables at the phase transitions and coexistence boundaries (Swesty, 1996). To this extent, a viable solution is sought; a tabular equation of state is highly desirable in addressing these complexities. A tabular interpolation scheme of this type of EoS can remove the difficulties in the implicit solution of hydrodynamic equations involved in various numerical hydrodynamic codes.

3.5 Electron-Positron Equation of State Model based on Table Interpolation of Helmholtz Free Energy

Conditions found in instability regions of very massive stars requires not only accurate and efficient but thermodynamically consistent equation of state tables. However, there are many stellar EoS routines that can be useful for solving thermodynamic conditions in this regime. In 1999, Timmes and Arnett (1999) compared the consistencies of thermodynamic properties as well as the execution speed of five different independent equations of state routines, with the aim to finding the most accurate in the regions where electrons are randomly degenerate and have an arbitrary speed close to the setting boundary conditions. Furthermore, the comparison provides a benchmark value for the accuracy and speeds of the EoS routines commonly used in stellar models. Among the five EoS considered, Timmes EoS shows a high degree of precision in thermodynamic consistency and was designed for maximum accuracy. It evaluates the Fermi-Dirac integrals (Equation 3.29) and their derivatives to high accuracy (at least 18 significant figures), such that the uncertainty in the value of φ is avoided. Similarly, the chemical potential is obtained from Newton-Raphson iteration to at least 15 significant figures. However, a special case of the Timmes EoS is the Helmholtz equation of state (Henceforth Helm-EoS) which was constructed only for electron-positron plasma based on table interpolation of Helmholtz free energy (Timmes & Swesty, 2000). The Helm-EoS evaluates the electron-positron EoS with accurate temperature-density grid, and displays thermodynamic consistency at the floating point, it also executes faster than any other stellar EoS. It is the stellar EoS of choice in many hydrodynamic and stellar evolution codes. The Helm-EoS is developed such that an isotope i having Z_i and A_i as its protons and nucleon number respectively, the total isotope i has a mass and number densities to be ρ (g cm^{-3}) and n_i (cm^{-3}) respectively and a temperature T (K). For this, the dimensionless mass fraction for individual isotope i is

$$X_i = \frac{A_i n_i}{\rho N_A} \tag{3.45}$$

And the dimensionless number density is

$$Y_i = \frac{X_i}{A_i} = \frac{n_i}{\rho N_A} \tag{3.46}$$

where N_A is the Avogadro's number (Timmes & Swesty, 2000; Woosley et al., 2002). However, constructing a tabular equation of state requires that the constraints for thermodynamic consistency and assurance of accuracy are satisfied. These constraints are

I. The first law of thermodynamics be defined by an exact differential equation, which, for reversible system requires;

$$dE = TdS + \frac{P}{\rho^2} d\rho \tag{3.47}$$

Since temperature and density are the variables, here, the most suitable thermodynamic potential is the Helmholtz free energy, which is defined by;

$$F = E - TS \tag{3.48}$$

Therefore, from Equation 3.47, the relationship between F, T and ρ is given by;

$$dF = \frac{P}{\rho^2} d\rho - SdT \tag{3.49}$$

where the pressure and entropy are defined as

$$P = \rho^2 \left.\frac{\partial F}{\partial \rho}\right|_T \tag{3.50}$$

And;

$$S = -\left.\frac{\partial F}{\partial T}\right|_\rho \tag{3.51}$$

II. The exactness of Equation 3.47, is achieved, if the following Maxwell relations (Callen, 1985) are satisfied;

$$P = \rho^2 \frac{\partial E}{\partial \rho}\bigg|_T + T\frac{\partial P}{\partial T}\bigg|_\rho \tag{3.52}$$

$$\frac{\partial E}{\partial \rho}\bigg|_T = T\frac{\partial S}{\partial T}\bigg|_\rho \tag{3.53}$$

$$\frac{\partial^2 F}{\partial T \partial \rho} = -\frac{\partial S}{\partial \rho}\bigg|_T = \frac{\partial^2 F}{\partial \rho \partial T} = \rho^{-2}\frac{\partial P}{\partial T}\bigg|_\rho \tag{3.54}$$

However, the first Maxwell Equation 3.52 relations is automatically satisfied by substituting Equations 3.47 & 3.48 into Equation 3.50. While the second Maxwell (Equation 3.53) relations is satisfied by substituting Equations 3.47 & 3.48 into Equation 3.51. And finally, the Maxwell (Equation 3.54) relation, which ensures commutivity of the mixed partial derivatives, is satisfied by Substituting Equations 3.47 & 3.48, into Equation 3.54. Failure to satisfy these thermodynamic constraints in any numerical simulations leads to an adiabatic flow owing to an unphysical decay of the entropy or temperature, which as a result, the stellar models experienced inaccuracies over a significant number of time steps (Swesty, 1996). For complete details on the interpolation of the Helmholtz free energy $F(\rho, T)$ see references (Swesty, 1996; Timmes & Swesty, 2000).

3.6 Neutrino Energy-Loss in Massive Stars

A fast moving particle passing through matter will transfer certain energy Q per unit time to the matter. This estimated energy is called energy-loss and can be expressed from collision limit (Kirzhnits et al., 1990);

$$Q = nv\int_0^{\omega_0} \frac{d\sigma}{d\omega} d\omega\omega \tag{3.55}$$

where σ is the scattering cross section of the particle, ω is the energy transfer and $\omega_0 = \frac{2E^2}{(2E+m)}$ is the energy transfer kinetic limit; E and v, are the energy, velocity of the particle in the rest frame of the medium; and the mass and number density of the particles are represented by m and n respectively. Neutrinos are produced in massive stars via two main processes; the weak process which occur in the nuclear network of the star and the thermal neutrino process which is from leptonic processes in the stellar plasma. This neutrino production is vital in the stars' late evolution such that instead of been dominated by photon diffusion the star is dominated by neutrino-cooling. The neutrino energy-loss could be large enough to cool the core of massive stars, as demonstrated by many researches (Jing-Jing & Zhi-Quan, 2009).

3.6.1 Processes of thermal neutrino energy-loss

As mentioned earlier, there are various methods of neutrino energy-loss and unlike many complicated neutrino processes, energy-loss rates of emitted neutrinos can be calculated very accurately from thermodynamic properties of matter; such as density-temperature regime (Esposito et al., 2003; Itoh et al., 1989; Itoh et al., 1996; Janka, 2016; Munakata et al., 1985; Wright et al., 2017a; Wright et al., 2017b). However, for different density-temperature regions, which described the endpoints of stellar evolutions, only thermal processes dominate (Esposito et al., 2002). There are however, four thermal neutrino processes which do not involve nuclear reactions but are product of very hot and dense plasma (Odrzywolek et al., 2004). These processes are; pair neutrino, plasma neutrino, photo neutrino and Bremsstrahlung neutrino processes (Itoh et al., 1989). Table 3.3, give details of temperature-density regions where each of these thermal neutrino processes dominate under different circumstances. At central temperatures, below $T \approx 5 \times 10^8 K$, a star cools through photo-neutrino process ($\gamma + e^- \rightarrow e^- + \nu_{e,\mu,\tau} + \bar{\nu}_{e,\mu,\tau} + e^\pm$), which only depend on conditions in nearby regions. However, since nuclei in the instability regions are fully ionized and has density ρ and temperature T in thermodynamic equilibrium, the temperature increases to $T \geq 10^9 K$, and the density is relatively low $\rho \leq 10^5 g\ cm^{-3}$, and as a result, pair neutrino become the most efficient cooling process in this region. Details on dominant thermal processes in the density-temperature regions of very-massive stars can be found in the work by Esposito et al. (2002).

Table 3.3: Density-temperature regions of thermal neutrino processes in very massive stars.

S/N	Thermal process	Reaction	Temperature-Density
1	Pair neutrino	$e^+ + e^- \rightarrow \nu_{e,\mu,\tau} + \bar{\nu}_{e,\mu,\tau}$	$T \geq 10^9 K, \rho \leq 10^5 gcm^{-3}$
2	Photo neutrino	$\gamma + e^{\pm} \rightarrow \nu_{e,\mu,\tau} + \bar{\nu}_{e,\mu,\tau} + e^{\pm}$	$10^8 \leq T \leq 10^9 K,$ $\rho \leq 10^5 gcm^{-3}$
3	Plasma neutrino	$\gamma^* \rightarrow \nu_{e,\mu,\tau} + \bar{\nu}_{e,\mu,\tau}$	$10^8 \leq T \leq 10^{10} K,$ $\rho \geq 10^6 gcm^{-3}$
4	Bremsstrahlung neutrino	$e^{\pm} + Z \rightarrow \nu_{e,\mu,\tau} + \bar{\nu}_{e,\mu,\tau} + e^{\pm}$	$10^8 \leq T \leq 10^{10} K,$ $\rho \geq 10^9 gcm^{-3}$

3.6.1.1 Pair neutrino

In stellar evolution theory, when temperature and density are relatively high, the dominant neutrino emission is by pair neutrino process. A specific example is the recent simulations which revealed that pair neutrino dominate over photo-neutrino process in 150 M⊙ and 250 M⊙ progenitors (Wright et al., 2017a). For details on emissivity and spectra of neutrinos in supernovae, see references (Itoh et al., 1996; Lunardini, 2015; Odrzywolek & Plewa, 2011; Wright et al., 2017a; Wright et al., 2017b). The pair neutrino energy-loss has been generally investigated based on Weinberg-Salam theory (Itoh et al., 1989; Itoh et al., 1996; Munakata et al., 1985) and specifically investigated by Esposito et al. (2003) at a wide density-temperature region for late stages of stellar evolutions. In the analytic fitting formulae, the energy-loss rate per unit volume due to pair neutrino process is expressed in the following form (Itoh et al., 1989; Munakata et al., 1985):

$$Q_{pair} = {}^1/_2\,[(x^2 + y^2) + n(z^2 + k^2)]Q_{pair}^{+} + {}^1/_2\,[(x^2 - y^2) + n(z^2 - k^2)]Q_{pair}^{-} \quad (3.56)$$

where $x = {}^{1}\!/_{2} + 2sin^2\theta_W$; $y = \frac{1}{2}$; $z = 1 - x$; $k = 1 - y$ and $sin^2\theta_W = 0.2319 + 0.0005$. θ_W is the Weinberg angle and n is the number of neutrino flavours other than electron neutrino which is practically massless at high temperature. However, Q^{+}_{pair} is calculated by (Beaudet et al., 1967), and Q^{-}_{pair} is given by Munakata et al. (1985). These two quantities are almost equal at temperature $T \leq 10^9$ K, and $Q^{+}_{pair} \gg Q^{-}_{pair}$ at $T \geq 10^{10}$ K. Different values of these quantities for different density-temperature regions can be found in Itoh et al. (1996). However, Equation 3.56 can be explicitly expressed in units of $ergs\ cm^{-3}s^{-1}$ as;

$$Q_{pair} = {}^{1}\!/_{2}\,[(x^2+y^2)+n(z^2+k^2)] \times \left[1 + \frac{(x^2-y^2)+n(z^2-k^2)}{(x^2+y^2)+n(z^2+k^2)} q_{pair}\right] \times g(\lambda)e^{-2/\lambda} f_{pair} \quad (3.57)$$

where;

$$q_{pair} = (10.7480\lambda^2 + 0.3967\lambda^{0.5} + 1.0050)^{-1.0} \times \left[1 + ({}^{\rho}\!/_{\mu_e})(7.692 \times 10^7\lambda^3 + 9.715 \times 10^6\lambda^{0.5})^{-1.0}\right]^{-0.3} \quad (3.58)$$

$$f_{pair} = \frac{(a_0 + a_1\xi + a_2\xi^2)e^{-c\xi}}{\xi^3 + b_1\lambda^{-1} + b_2\lambda^{-2} + b_3\lambda^{-3}} \quad (3.59)$$

$$g(\lambda) = 1 - 13.04\lambda^2 + 133.5\lambda^4 + 1534\lambda^6 + 918.6\lambda^8 \quad (3.60)$$

$$\xi = \left(\frac{({}^{\rho}\!/_{\mu_e})}{10^9 gcm^{-3}}\right)\lambda^{-1} \quad (3.61)$$

$$\lambda = \frac{k_B T}{mc^2} = \left(\frac{T}{5.9302 \times 10^9 K}\right) \quad (3.62)$$

where ${}^{\rho}\!/_{\mu_e}$ is in density unit. And the natural unit $\hbar = c = 1$ is used. The numerical values of the coefficients $a_0, a_1, a_2, b_1, b, b_3$ and c are defined (Itoh et al., 1989; Jing-Jing & Zhi-Quan, 2009) for different temperature values.

3.6.1.2 Photo neutrino

In the temperature range $10^8 \leq T \leq 10^9 K$, and density $\rho \leq 10^5 gcm^{-3}$, only photo neutrino process dominates and the energy-loss rate per unit volume due to this process of neutrino can be given by:

$$Q_{photo} = {}^1/_2\,[(x^2 + y^2) + n(z^2 + k^2)]Q^+_{photo} - {}^1/_2\,[(x^2 - y^2) + n(z^2 - k^2)]Q^-_{photo} \quad (3.63)$$

All quantities in this equation are similar to Equation 3.56. And according to modifications made by Itoh et al. (1989) this can further be expressed as:

$$Q_{photo} = {}^1/_2\,[(x^2 + y^2) + n(z^2 + k^2)]\left[1 - \frac{(x^2-y^2)+n(z^2-k^2)}{(x^2+y^2)+n(z^2+k^2)} q_{photo}\right] f_{photo} \quad (3.64)$$

where;

$$q_{photon} = 0.666(1 + 2.045\lambda)^{-2.066}\left[1 + \left({}^{\rho}/_{\mu_e}\right)(1.875 \times 10^8\lambda^3 + 1.653 \times 10^8\lambda^2 + 8.499 \times 10^8\lambda^3 - 1.604 \times 10^8\lambda^4)^{-1.0}\right]^{-1.0} \quad (3.65)$$

And other constant remain same as above, except;

$$f_{photo} = \frac{(a_0 + a_1\xi + a_2\xi^2)e^{-c\xi}}{\xi^3 + b_1\lambda^{-1} + b_2\lambda^{-2} + b_3\lambda^{-3}} \quad (3.66)$$

3.6.1.3 Plasma neutrino

The plasma neutrino process becomes important at the temperature-density region $10^8 \leq T \leq 10^{10} K \; and \; \rho \geq 10^6 gcm^{-3}$. The energy-loss rate per unit volume in the Weinberg-Salam theory for plasma neutrino process can be define by:

$$Q_{plasma} = (x^2 + nz^2)Q_V \quad (3.67)$$

The contributions of the vector Q_V has been explicitly defined by Kohyama et al. (1994) and by Itoh et al. (1996). For exact calculations (particularly at low-temperature), Equation 3.67 can be given by a fitted formula as:

$$Q_{plasma} = (x^2 + nz^2)(\rho/\mu_e)^3 f_{plasma} \quad (3.68)$$

Where;

$$f_{plasma} = \frac{(a_0+a_1\xi+a_2\xi^2)e^{-c\xi}}{\xi^3+b_1\lambda^{-1}+b_2\lambda^{-2}+b_3\lambda^{-3}} \tag{3.69}$$

3.6.1.4 Bremsstrahlung neutrino

In Bremsstrahlung neutrino process, the density-temperature region is between $10^8 \leq T \leq 10^{10} K \ and \ \rho \geq 10^9 gcm^{-3}$. However, for accurate calculations of the energy-loss rate influenced by this process, this region can be dived into: region of strongly degenerate electrons and region of weakly degenerate electrons. This has been investigated by many researchers (Itoh & Kohyama, 1983; Itoh et al., 1984; Munakata et al., 1987), but simplicity we refer to Itoh et al. (1996) for complete analysis of the expressions of both weakly and strongly degenerate electrons.

3.6.2 Energy-loss by neutrino oscillations in massive stars

Most stellar models calculate energy-loss of the neutrinos that are produced through thermal processes in the star without considering effects of neutrino oscillations. This might be due to the fact that effect of neutrino oscillations on the energy-loss is very small and is mostly neglected. However, in 2014, results from Super-Kamiokande experiments confirmed that terrestrial matter indeed has effects on solar neutrino oscillations (Renshaw et al., 2014). This latest observations warrants the consideration of the effects of oscillations on neutrino-energy loss in massive stars. This is because, during the evolution of massive stars large amount of neutrinos are released and the temperature-density grid is high compared to solar-like models. Neutrinos can only interact through weak interactions with matter, and are massless, as emphasized by standard model of particles. As such this work will only consider weak interactions of neutrinos with electrons by including effects of neutrino oscillations. The total energy loss (ΔE_ν) through oscillations for a neutrino consisting of an initial energy E_ν^i in the centers of massive stars, can be calculated by integration of the modified stopping power equation (SPE) using relevant properties which are taken from the massive stellar evolution models under consideration. When the neutrino travels through a distance R (radius of the stars), the neutrino energy that will escape from the star is given by;

$$E_{\nu}^{f} = \int_{R} \left(\frac{dE}{dR}\right) dR \tag{3.70}$$

And therefore, the total neutrino-energy loss is obtained from;

$$\Delta E_{\nu} = E_{\nu}^{i} - E_{\nu}^{f} \tag{3.71}$$

E_{ν}^{i} and E_{ν}^{f} are the initial and final neutrino energies in the star. In all neutrino flavors, except electron neutrinos, the scattering with electron has neutral bosons as mediator. The latter is mediated by $W^{\pm}$ and Z^{o} bosons, according to Feynman diagram which we have shown in Figure 2.6.

3.7 Chapter Summary

Chapter three represents methodology employed in carrying out this research. In this chapter, the post-processed stellar models are described; which include physical properties of the progenitor models and methods and codes used for stellar evolution. A generalized description of equation of states (EoS) involved in stellar models is presented. The distribution functions and adiabatic processes are discussed in subsection two of this chapter. The chapter is narrowed to the scope of this research, by describing relativistic electron-positron EoS, arising from pair-production in centres of the stars and at high temperature. Specific EoS routines used in this work is described in section 4 of this chapter. A model constructed into this EoS is also discussed. Finally, the method used for neutrino energy-loss is presented in last part of this chapter. In this work, thermal neutrino processes from the selected progenitor models of very-massive star is calculated.

CHAPTER 4: RESULTS AND DISCUSSION

4.1 Adiabatic Properties from the Instability Regions of Very-Massive Stars

Models of very-massive stellar evolutions provides qualitative information about the instability of the progenitor stars. The dynamical instability of any star is determined by its adiabatic indices (Bond et al., 1984), such that a star is dynamically unstable when the ratio of its adiabatic index is less than 4/3 (Ledoux, 1946). In 1990, Kippenhahn et al. (1990), maintained that due to hydrodynamic instability; the radial structure of stars is an adiabatic dependent. Whence, adiabatic properties are greatly important in massive objects such as stars and in many astrophysics and plasma research (Beule et al., 1997). However, Pols (2011), confirmed that pair-production leads to low adiabatic index which triggered explosion of massive stars. For this reason, there is need to identify the adiabatic effects of pair-production from any particular stellar model. A stellar model may not be beautiful if its stability and/or instability is unknown. This is why many cases were considered and the stability of many models was investigated. Consequently, effects of adiabatic changes due to pair-production in massive stars, appeared worth-while to be examined and studied, considering its role in the stability and/or instability, collapse, and explosion of massive stars. For this reason, the discovery of a super-luminous supernova (SLSN), has rapidly increased the interest in pair-instability explosion of massive stars. Nuclear adiabatic process, considered in this work, is defined by Beule et al. (1997) as a thermonuclear process which is characterized by a rapid change of state without heat exchange between the system and its surrounding In massive stars, however, pairs of electrons and positrons are produced as a result of high energy photons in their core (Barkat et al., 1967; Bond et al., 1984; Carr et al., 1984; El Eid & Hilf, 1977; Fraley, 1968; Ober et al., 1983; Rakavy & Shaviv, 1967; Stringfellow & Woosley, 1988; Wheeler, 1977). Meanwhile, different magnitude of adiabatic index could make a star unstable, or in general term, stability of a star could be affected by decrease in its adiabatic index (Ledoux, 1946). Once any collapsing star enter the electron-positron pair-production region (Figure 1.1), it will become destabilized by pair-production through a decrease in adiabatic index (Montero et al., 2012). One of significant role of this pair-production (inside the core of massive stars) is its effect on instability and subsequent explosion of the star, which occur during advanced nuclear burning stages of evolution. In general, when abundance of degenerate electrons and positrons in the centres of massive stars are comparable to each other, there exist a region, in temperature-density plane where adiabatic index is <1.33. The adiabatic exponents and their derivatives are, therefore, a major event in stellar evolution; ranging from stellar formation, pulsation, convection to core collapse and supernova explosions. In particular, adiabatic derivatives (exponent and temperature gradient) measures the thermodynamic response such as expansion and/or compression, characterized by dynamic instability as well as convection instability of stars (Hansen et al., 2004; Kippenhahn et al., 1990; Maeder, 2008). Similarly, the behaviour of a star after it is adiabatically expanded or compressed depends on the numerical value of the adiabatic index (γ_{ad}). Thus, we know that the stars' internal energy derivatives with respect to pressure, temperature and density are relevant for its stability against convection and dynamical motion. This section investigates roles of adiabatic processes inside the region where electron-positron pairs are created in the centres of massive stars, which is originated at high central temperature and relatively low density (Phillips, 2013). The adiabatic quantities due to pair-production in 150 $M_\odot$ and 200 $M_\odot$ rotating models at Small Magellanic Cloud (SMC) and rotating and non-rotating 500 $M_\odot$ models at Low Magellanic Cloud (LMC), is numerically evaluated and analysed. The non-rotating model experienced least instability by achieving a maximum central temperature $T_c = 1.02\text{x}10^9$ K and density $\rho_c = 3.29\text{x}10^4$ g cm^{-3}. On the other hand, rotating models for 150 $M_\odot$, 200 $M_\odot$ and 500 $M_\odot$ achieved maximum central temperature and density given by T_c = 1.94x10^9 , 1.99x10^9 , and 2.25x10^9 [K], and ρ_c = 3.42x10^5 , 3.02x10^5, and 8.25x10^5 [g cm^{-3}] respectively. However, the initial central temperature and density of the instability regions are shown in table 3.3 (columns 7th and 8th). The equation of state chosen for this part of work is HELM-EoS which is described in chapter three. The input of the routines (as explained in previous chapters) are central mass fractions of individual compositions, average charge per isotope and its average nucleons number, under a particular central temperature (K) and density (g cm^{-3}). The result of this routine produced many physical properties ranging from pressure, specific thermal energies to most relevant, in this section, the adiabatic quantities such as adiabatic index and specific heats of the species involved. In centres of massive stars, many processes occur, particularly, at high temperature and relatively low density. One such important process is photon disintegration into electron-positron pairs when the photons' energy ($h\upsilon$) is higher than the rest-mass energy of the pairs ($h\upsilon > 2m_ec^2$), this only occur during collision with nucleus (Pols, 2011). The electron-positron pairs are created just before formation of any element heavier than oxygen, and therefore, various physical quantities due to pair-production in centres of massive stars requires understanding of the adiabatic effects, such as heat capacities, adiabatic indices etc., in order to describe their phenomenology. The thermodynamic coefficients that described pair-production process in massive stars are derived from electron-positron EoS using thermodynamic laws, together with internal energy equations; the most important of such thermodynamic coefficients are specific heat capacities, adiabatic indices and adiabatic temperature gradient (Pols, 2011). We have discussed all of these extensively in chapter two and three. In Table 4.1 the adiabatic properties obtained from progenitor models under consideration are shown. As we can see in this table only advanced burning flues that are used in the production of electron-positron thermal energy in the instability region, possesses low adiabatic index below 4/3. In the next sections, we discuss result of these quantities and its significance on the dynamical instability of massive stars.

4.1.1 Heat Capacities

The heat capacities of rotating progenitor models are found to be decreased when central temperature increases within the pair-production region. And it increased with central density. Thus, the central temperature required for explosion and collapse of massive star (with rotation) can be attained at small amount of heat within the pair-production region. In the following sections, physical dynamic of heat capacities in the models under consideration is discussed.

4.1.1.1 150 M⊙ Progenitor Model

The heat capacities of 150 M⊙ model in the instability regions, shown in Table 4.1, are independent of the stars' composition. In Figure 4.1, we show the behaviour of heat capacities with respect to constant pressure plotted against temperature and density in the instability region. At onset of pair-production, the compressed star speedily rise the temperature of the instability region until it produced more electron-positron thermal energies. As a result of this, the region become completely disturbed by many thermal processes and the quantity of heat required to raise the temperature reduces the density of pair-production. The manifestation of this dynamic is that the star cools down immediately after pair-production is ignited.

4.1.1.2 200 M⊙ Progenitor Model

While heat capacities at constant volume show similar dynamic with respect to central mass fractions, it, however, differ in magnitude. In Figure 4.2 the heat capacity with respect to temperature and density is shown. However, it is observed that the amount of heat required to rise a unit temperature necessary for pair- production is very small. This also follows same physical argument with previous 150 M⊙ model.

Table 4.1: Adiabatic properties from instability region of 150 $M_\odot$ progenitor model, showing few chemical abundance within which adiabatic index is below 4/3.

Den [g cm^{-3}]	T [K]	He3				C13				O17			
		C_v [erg K^{-1}]	C_p [erg K^{-1}]	γ_{ad}	Δ_{ad}	C_v [erg K^{-1}]	C_p [erg K^{-1}]	γ_{ad}	Δ_{ad}	C_v [erg K^{-1}]	C_p [erg K^{-1}]	γ_{ad}	Δ_{ad}
3.2386E+04	1.0487E+09	1.2581E+07	1.4882E+15	1.2264	1.3026	1.9091E+04	1.6477E+12	1.2268	1.3026	5.8230E+06	6.8732E+14	1.2264	1.3026
3.8143E+04	1.0935E+09	1.2518E+07	1.4408E+15	1.2233	1.2992	1.8997E+04	1.6302E+12	1.2237	1.2992	5.7938E+06	6.6564E+14	1.2233	1.2992
4.2581E+04	1.1252E+09	1.2506E+07	1.4179E+15	1.2219	1.2969	1.8980E+04	1.6256E+12	1.2223	1.2969	5.7882E+06	6.5517E+14	1.2219	1.2969
4.5910E+04	1.1478E+09	1.2511E+07	1.4060E+15	1.2213	1.2953	1.8987E+04	1.6368E+12	1.2217	1.2954	5.7903E+06	6.4975E+14	1.2213	1.2953
4.9125E+04	1.1686E+09	1.2522E+07	1.3976E+15	1.2210	1.2939	1.9005E+04	1.6484E+12	1.2213	1.2940	5.7955E+06	6.4593E+14	1.2210	1.2939
5.1996E+04	1.1864E+09	1.2535E+07	1.3918E+15	1.2210	1.2928	1.9025E+04	1.6587E+12	1.2213	1.2928	5.8014E+06	6.4328E+14	1.2210	1.2928
5.5059E+04	1.2047E+09	1.2546E+07	1.3861E+15	1.2211	1.2916	1.9043E+04	1.6680E+12	1.2214	1.2916	5.8067E+06	6.4070E+14	1.2211	1.2916
5.8099E+04	1.2220E+09	1.2555E+07	1.3809E+15	1.2213	1.2906	1.9057E+04	1.6761E+12	1.2216	1.2906	5.8110E+06	6.3835E+14	1.2213	1.2906
6.1385E+04	1.2399E+09	1.2560E+07	1.3750E+15	1.2217	1.2895	1.9064E+04	1.6824E+12	1.2220	1.2895	5.8129E+06	6.3565E+14	1.2217	1.2895
6.5010E+04	1.2586E+09	1.2558E+07	1.3680E+15	1.2223	1.2885	1.9062E+04	1.6872E+12	1.2225	1.2885	5.8122E+06	6.3248E+14	1.2223	1.2885
6.8629E+04	1.2764E+09	1.2548E+07	1.3603E+15	1.2229	1.2875	1.9047E+04	1.6893E+12	1.2232	1.2875	5.8077E+06	6.2894E+14	1.2229	1.2875
7.2523E+04	1.2946E+09	1.2532E+07	1.3515E+15	1.2237	1.2865	1.9022E+04	1.6894E+12	1.2240	1.2866	5.8000E+06	6.2487E+14	1.2237	1.2865
7.6806E+04	1.3137E+09	1.2509E+07	1.3417E+15	1.2246	1.2856	1.8988E+04	1.6877E+12	1.2249	1.2856	5.7896E+06	6.2039E+14	1.2246	1.2856
8.0015E+04	1.3275E+09	1.2490E+07	1.3345E+15	1.2254	1.2849	1.8960E+04	1.6859E+12	1.2256	1.2849	5.7809E+06	6.1708E+14	1.2254	1.2849
8.2829E+04	1.3391E+09	1.2474E+07	1.3284E+15	1.2261	1.2844	1.8935E+04	1.6843E+12	1.2263	1.2844	5.7731E+06	6.1428E+14	1.2261	1.2844
8.5660E+04	1.3506E+09	1.2457E+07	1.3227E+15	1.2267	1.2839	1.8910E+04	1.6823E+12	1.2270	1.2839	5.7656E+06	6.1166E+14	1.2267	1.2839
8.8794E+04	1.3630E+09	1.2438E+07	1.3164E+15	1.2275	1.2833	1.8881E+04	1.6797E+12	1.2278	1.2833	5.7567E+06	6.0876E+14	1.2275	1.2833
9.2360E+04	1.3766E+09	1.2417E+07	1.3097E+15	1.2284	1.2828	1.8849E+04	1.6771E+12	1.2287	1.2828	5.7469E+06	6.0567E+14	1.2284	1.2828
9.6488E+04	1.3920E+09	1.2393E+07	1.3025E+15	1.2295	1.2822	1.8813E+04	1.6740E+12	1.2297	1.2822	5.7359E+06	6.0235E+14	1.2295	1.2822
1.0178E+05	1.4109E+09	1.2363E+07	1.2939E+15	1.2309	1.2814	1.8768E+04	1.6702E+12	1.2311	1.2814	5.7221E+06	5.9839E+14	1.2309	1.2814
1.0825E+05	1.4332E+09	1.2329E+07	1.2845E+15	1.2325	1.2806	1.8716E+04	1.6662E+12	1.2328	1.2806	5.7061E+06	5.9405E+14	1.2325	1.2806
1.1472E+05	1.4546E+09	1.2297E+07	1.2763E+15	1.2342	1.2799	1.8668E+04	1.6629E+12	1.2344	1.2799	5.6916E+06	5.9029E+14	1.2342	1.2799
1.2168E+05	1.4768E+09	1.2268E+07	1.2690E+15	1.2360	1.2792	1.8624E+04	1.6606E+12	1.2362	1.2792	5.6780E+06	5.8693E+14	1.2360	1.2792
1.2922E+05	1.4999E+09	1.2242E+07	1.2629E+15	1.2380	1.2785	1.8585E+04	1.6596E+12	1.2382	1.2785	5.6661E+06	5.8411E+14	1.2380	1.2785
1.3743E+05	1.5244E+09	1.2224E+07	1.2588E+15	1.2401	1.2779	1.8557E+04	1.6612E+12	1.2403	1.2779	5.6577E+06	5.8224E+14	1.2401	1.2779
1.4633E+05	1.5502E+09	1.2217E+07	1.2574E+15	1.2423	1.2772	1.8546E+04	1.6664E+12	1.2425	1.2772	5.6542E+06	5.8159E+14	1.2423	1.2772
1.5593E+05	1.5774E+09	1.2225E+07	1.2598E+15	1.2447	1.2767	1.8559E+04	1.6768E+12	1.2449	1.2767	5.6582E+06	5.8272E+14	1.2447	1.2767
1.6295E+05	1.5970E+09	1.2244E+07	1.2644E+15	1.2465	1.2763	1.8588E+04	1.6882E+12	1.2467	1.2763	5.6668E+06	5.8487E+14	1.2465	1.2763
1.6895E+05	1.6136E+09	1.2266E+07	1.2698E+15	1.2480	1.2760	1.8621E+04	1.6999E+12	1.2482	1.2760	5.6771E+06	5.8740E+14	1.2480	1.2760
1.7419E+05	1.6280E+09	1.2289E+07	1.2755E+15	1.2493	1.2757	1.8657E+04	1.7113E+12	1.2495	1.2757	5.6879E+06	5.9003E+14	1.2493	1.2757
1.7925E+05	1.6416E+09	1.2312E+07	1.2811E+15	1.2505	1.2755	1.8691E+04	1.7223E+12	1.2507	1.2755	5.6983E+06	5.9264E+14	1.2505	1.2755
1.8418E+05	1.6545E+09	1.2332E+07	1.2863E+15	1.2517	1.2753	1.8722E+04	1.7324E+12	1.2519	1.2753	5.7076E+06	5.9504E+14	1.2517	1.2753
1.8899E+05	1.6668E+09	1.2348E+07	1.2906E+15	1.2528	1.2751	1.8746E+04	1.7411E+12	1.2530	1.2751	5.7150E+06	5.9704E+14	1.2528	1.2751
1.9418E+05	1.6797E+09	1.2359E+07	1.2941E+15	1.2540	1.2750	1.8763E+04	1.7487E+12	1.2541	1.2750	5.7201E+06	5.9865E+14	1.2540	1.2750

Table 4.1, continued.

Den [g cm^{-3}]	T [K]	He3				C13				O17			
		C_v [erg K^{-1}]	C_p [erg K^{-1}]	γ_{ad}	Δ_{ad}	C_v [erg K^{-1}]	C_p [erg K^{-1}]	γ_{ad}	Δ_{ad}	C_v [erg K^{-1}]	C_p [erg K^{-1}]	γ_{ad}	Δ_{ad}
1.9935E+05	1.6921E+09	1.2364E+07	1.2963E+15	1.2551	1.2748	1.8770E+04	1.7543E+12	1.2552	1.2748	5.7225E+06	5.9969E+14	1.2551	1.2748
2.0492E+05	1.7049E+09	1.2362E+07	1.2971E+15	1.2562	1.2747	1.8767E+04	1.7579E+12	1.2564	1.2747	5.7214E+06	6.0008E+14	1.2562	1.2747
2.1052E+05	1.7173E+09	1.2354E+07	1.2967E+15	1.2573	1.2745	1.8754E+04	1.7595E+12	1.2575	1.2745	5.7176E+06	5.9988E+14	1.2573	1.2745
2.1658E+05	1.7303E+09	1.2338E+07	1.2949E+15	1.2585	1.2744	1.8731E+04	1.7592E+12	1.2586	1.2744	5.7105E+06	5.9907E+14	1.2585	1.2744
2.2267E+05	1.7428E+09	1.2318E+07	1.2922E+15	1.2596	1.2743	1.8701E+04	1.7574E+12	1.2598	1.2743	5.7013E+06	5.9780E+14	1.2596	1.2743
2.2930E+05	1.7560E+09	1.2292E+07	1.2882E+15	1.2607	1.2742	1.8661E+04	1.7540E+12	1.2609	1.2742	5.6891E+06	5.9599E+14	1.2607	1.2742
2.3665E+05	1.7701E+09	1.2259E+07	1.2830E+15	1.2620	1.2741	1.8610E+04	1.7487E+12	1.2622	1.2741	5.6736E+06	5.9357E+14	1.2620	1.2741
2.5007E+05	1.7948E+09	1.2192E+07	1.2723E+15	1.2641	1.2739	1.8510E+04	1.7373E+12	1.2643	1.2739	5.6429E+06	5.8864E+14	1.2641	1.2739
2.7504E+05	1.8381E+09	1.2071E+07	1.2531E+15	1.2678	1.2737	1.8326E+04	1.7158E+12	1.2680	1.2737	5.5868E+06	5.7976E+14	1.2678	1.2737
3.0652E+05	1.8890E+09	1.1935E+07	1.2324E+15	1.2720	1.2736	1.8119E+04	1.6926E+12	1.2722	1.2736	5.5237E+06	5.7019E+14	1.2720	1.2736
3.4167E+05	1.9418E+09	1.1802E+07	1.2133E+15	1.2762	1.2736	1.7918E+04	1.6710E+12	1.2764	1.2736	5.4625E+06	5.6138E+14	1.2762	1.2736

The compression must have increased pair-production energy and pressure. This thermal energy is necessary for annihilation of the pairs. In both models, rotation increased mass loss and mass of oxygen cores such that more pairs are produced and later annihilated.

4.1.1.3 500 M⊙ Progenitor Model

The heat, at constant volume and pressure, is, however, independent of chemical abundance within the instability region, and is steadily uniform at final mass of explosion. In Figures 4.3 & 4.4, the manifestation of this physical behaviour is shown. These figures compares rotating and non-rotating models. The rotation affects the nucleosynthesis of the stellar evolution, and in the productions of pairs, temperature and density play key role on the instability of the region. The nuclear burnings affect not only the heat capacities but also rotation of the stars. In Figure 4.5 it can be seen that, as mass loss continue to increase in rotating models, heat capacities slow down, so that it induces high central temperature and density for production of pairs and subsequent annihilations and explosion of the stars. The non-rotating model experienced greater heat capacities and possesess low mass loss which drives the star further away from pair-production region. This also confirms that non-rotating models are not good for pair-production, due to the fact that most of its mass is lost to heat, and therefore, the star must collapse before its explosions.

4.1.2 Adiabatic Index

The adiabatic index γ_{ad} ($\gamma_{ad} = \left(\frac{\partial \ln P}{\partial \ln \rho}\right)_{ad}$) as a measure of pressure to adiabatic compression or expansion, is found to be proportional to central temperature in the instability region (as in Figure 4.6) and is constant when pressure is proportional to density (i.e. $P\ \alpha\ \rho^{\gamma_{ad}}$). This adiabatic index is however, related to dynamical stability of stars, it describe whether the star is dynamically unstable when pressure average of γ_{ad} is less than 4/3, (Bond et al., 1984).

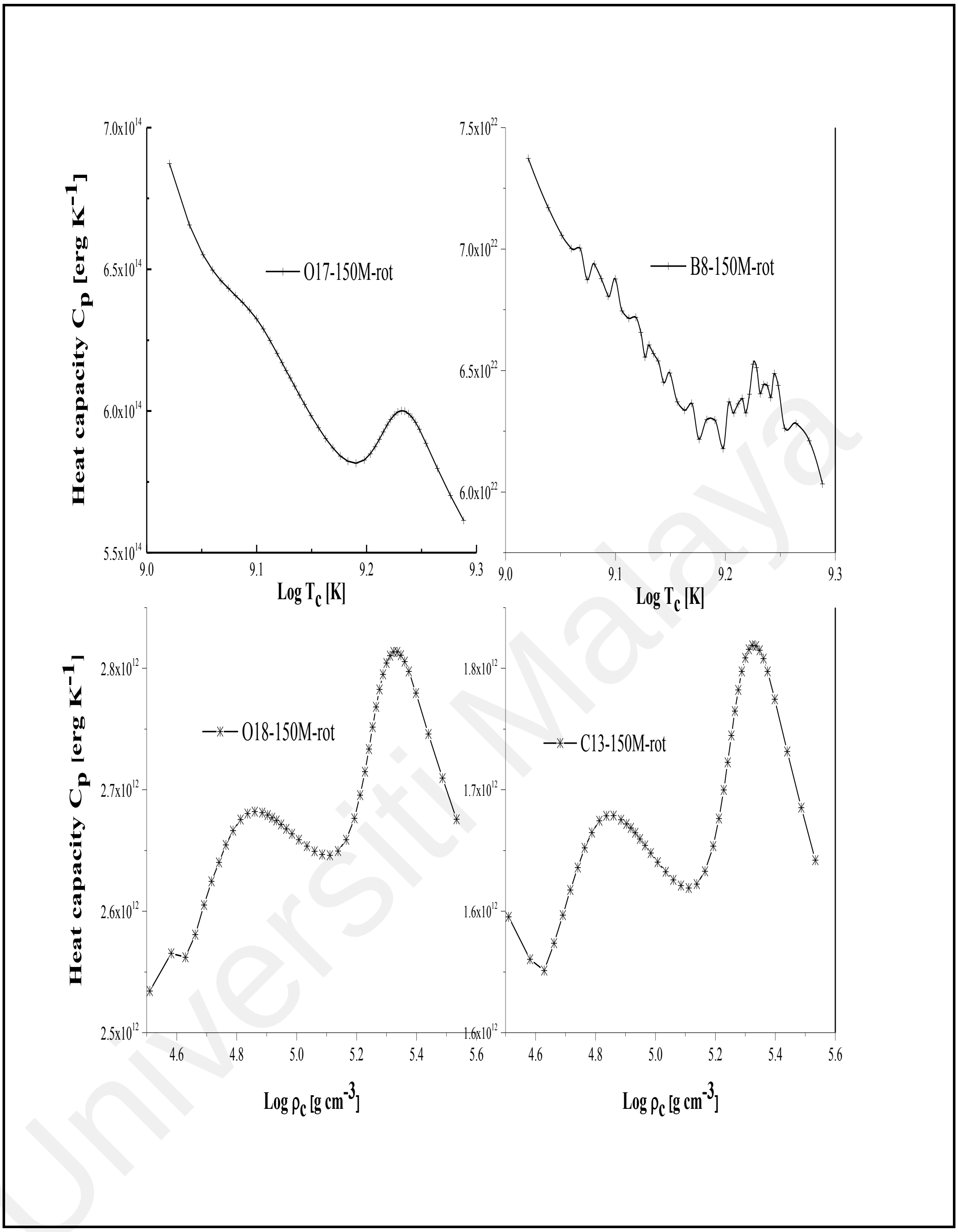

Figure 4.1: Heat capacity at constant pressure due to pair-production for 150 M⊙ progenitor model. Upper graph represents heat capacity with temperature, while lower with density.

The numerical values of the adiabatic indices for 150 M⊙ and for all models under consideration are shown in Table 4.1. These values shows that, indeed these models possesses adiabatic indices below 4/3 at late burning stages of their evolution. Figure 4.7, shows adiabatic indices with mass loss from the models under consideration.

Table 4.2: Adiabatic quantities at minimum and maximum temperature and density in the centres of massive stars with respect to selected chemical abundance. R & NR represents rotating and non-rotating models respectively.

Adiabatic Quantity	^{13}C				^{18}O				^{8}B			
	150 [M⊙]-R	**200** [M⊙]-R	**500** [M⊙]-**R**	**500** [M⊙]-**NR**	**150** [M⊙]-R	**200** [M⊙]-R	**500** [M⊙]-**R**	**500** [M⊙]-**NR**	**150** [M⊙]-R	**200** [M⊙]-R	**500** [M⊙]-**R**	**500** [M⊙]-**NR**
C_v[erg K^{-1}]	1.91E4 1.80E4	1.94E4 1.89E4	3.30E03 2.93E03	2.58E4 2.52E4	3.08E04 2.89E4	3.93E04 3.82E4	7.80E03 6.85E03	2.96E03 2.91E3	6.26E14 5.85E14	9.52E14 9.25E14	1.12E15 9.78E14	5.40E15 5.30E15
C_p[erg K^{-1}]	1.65E12 1.67E12	1.93E12 2.19E12	8.88E10 1.43E11	2.04E12 1.97E12	2.53E12 2.68E12	3.99E12 4.49E12	2.42E11 3.64E11	5.91E10 5.88E10	7.37E22 6.03E22	1.35E23 1.19E23	9.95E22 7.14E22	5.96E23 5.58E23
γ_{ad}	1.23 1.28	1.23 1.28	1.24 1.30	1.23 1.23	1.23 1.28	1.23 1.28	1.23 1.30	1.25 1.25	1.22 1.28	1.23 1.30	1.23 1.28	1.24 1.23
Δ_{ad}	1.30 1.27	1.31 1.27	1.31 1.28	1.31 1.31	1.30 1.27	1.31 1.27	1.31 1.28	1.31 1.31	1.30 1.27	1.31 1.27	1.30 1.28	1.31 1.31

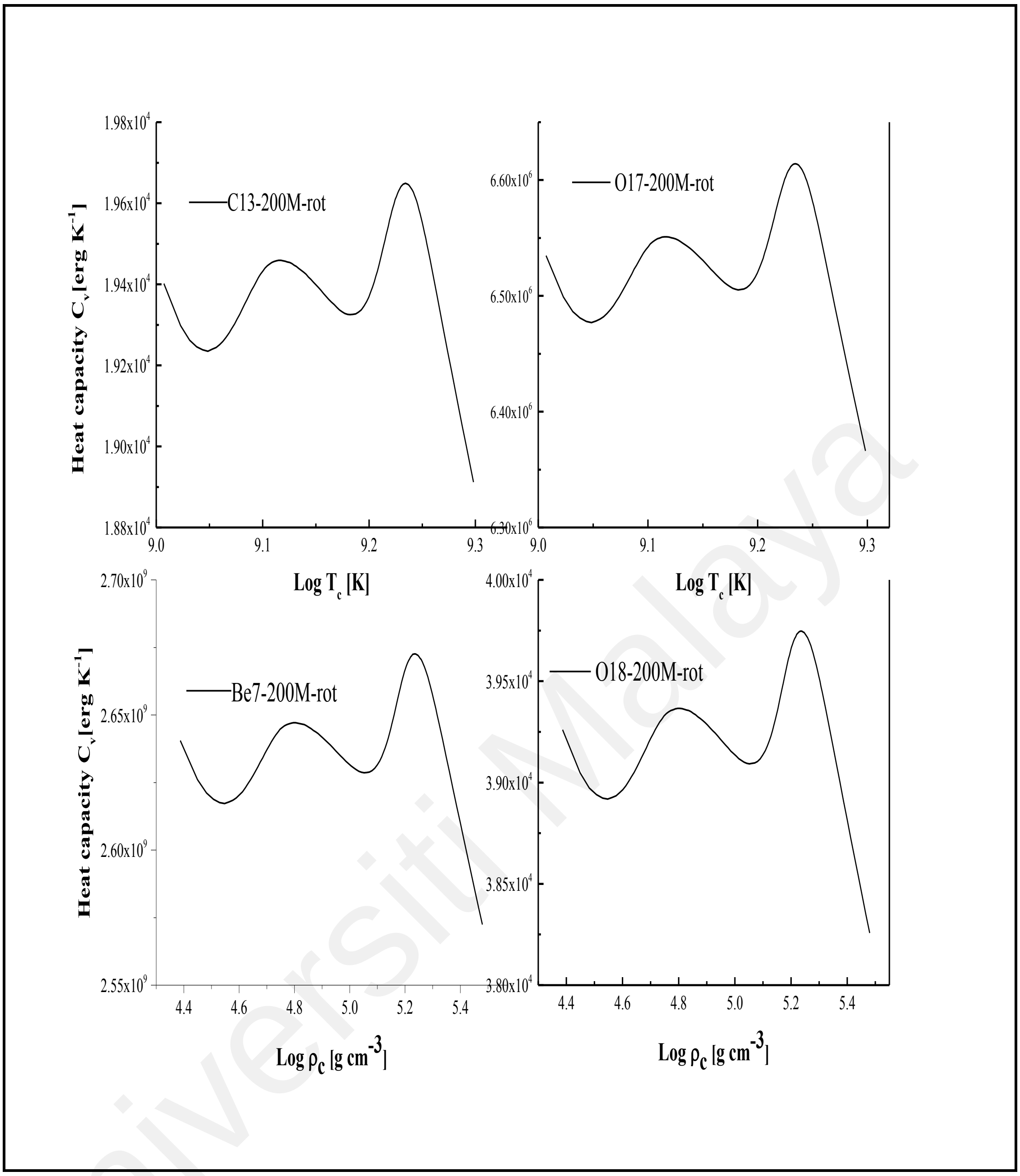

Figure 4.2: Heat capacity at constant volume due to pair-production in 200 M⊙ progenitor model. Upper graph represents heat capacity with temperature, while lower is for density. M represents M⊙.

We observed that rotation reduced mass loss and increase adiabatic index. The non-rotating model possesses lowest adiabatic index which is the manifestation of its quick collapse as it lost most of its mass very quickly in the instability region. Similarly, oxygen core in rotating models induces an increase of adiabatic indices such that rotating stars produces pairs of electrons and positrons. In Figure 4.6, effects of electron-positron pairs, in which the adiabatic indices are less than 4/3, are plotted against temperature within the instability regions. However, in this figure, we show that the adiabatic index due to pair-production is almost independent of nuclear burning taking place in the instability region, as predicted by Rakavy and Shaviv (1967). This adiabatic index which represents pressure derivatives create disturbance in the region and is fundamentally positive with temperature for all rotating models but decreases in case of the non-rotating, as can be seen in Figure 4.6. This scenario, in rotating model, keeps the instability in the region and the star produces more pairs which later annihilate into neutrinos. Therefore, pair-production leads to a dynamical instability which is responsible for rapid explosion of the star immediately after creation of electron-positron pairs. Meanwhile, sudden decrease of the adiabatic index in non-rotating model and its quick collapse is basically due to its low mass loss and less oxygen core mass that is necessary for production of the pairs.

4.1.3 Adiabatic Temperature Gradients

The temperature gradient $\nabla_{ad} = \left(\frac{\partial \log T}{\partial \log P}\right)_{ad}$ is another adiabatic derivative which determines characteristics of temperature under adiabatic compression or expansion of a star and is evaluated as flow rate of energy in relation to surface of the star. This quantity is only important for convective stability of a particular star. In Table 4.2, minimum and maximum evaluated values of this quantity is presented in last rows for all models under consideration. However, we noticed equal values for all models which clearly shows that all the models are convectively unstable and finally explode as PISNe. The convective instability, which is described by adiabatic temperature gradients, is out of scope of this work. It is interesting to note that the adiabatic quantities show similar dynamics in all the rotating models within the pair-production regions. Non-rotating model has different pattern of instability. The quantity of heat required to rise central temperature necessary for explosions of the star to occur is found to be decreasing.

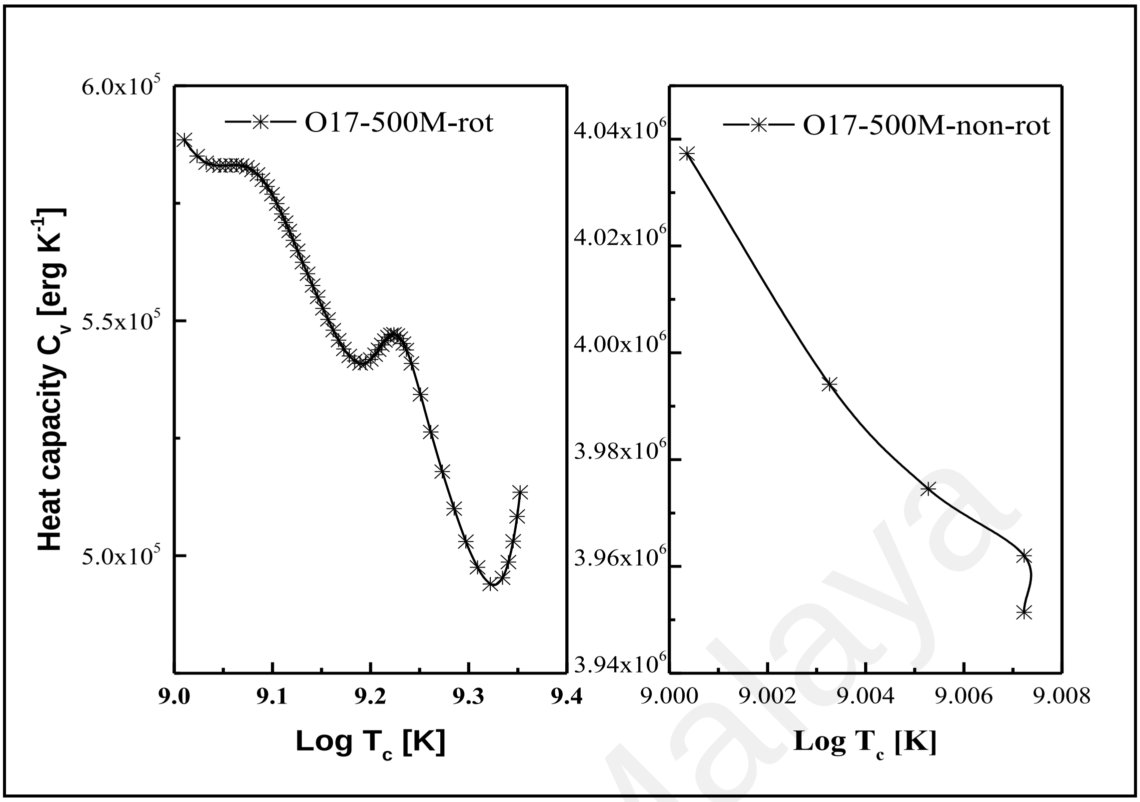

Figure 4.3: Evolution of specific heat capacities at constant volume against temperature for rotating (left) and non-rotating (right) 500 M⊙ model. M represents M⊙ while R and NR represent rotation and non-rotation.

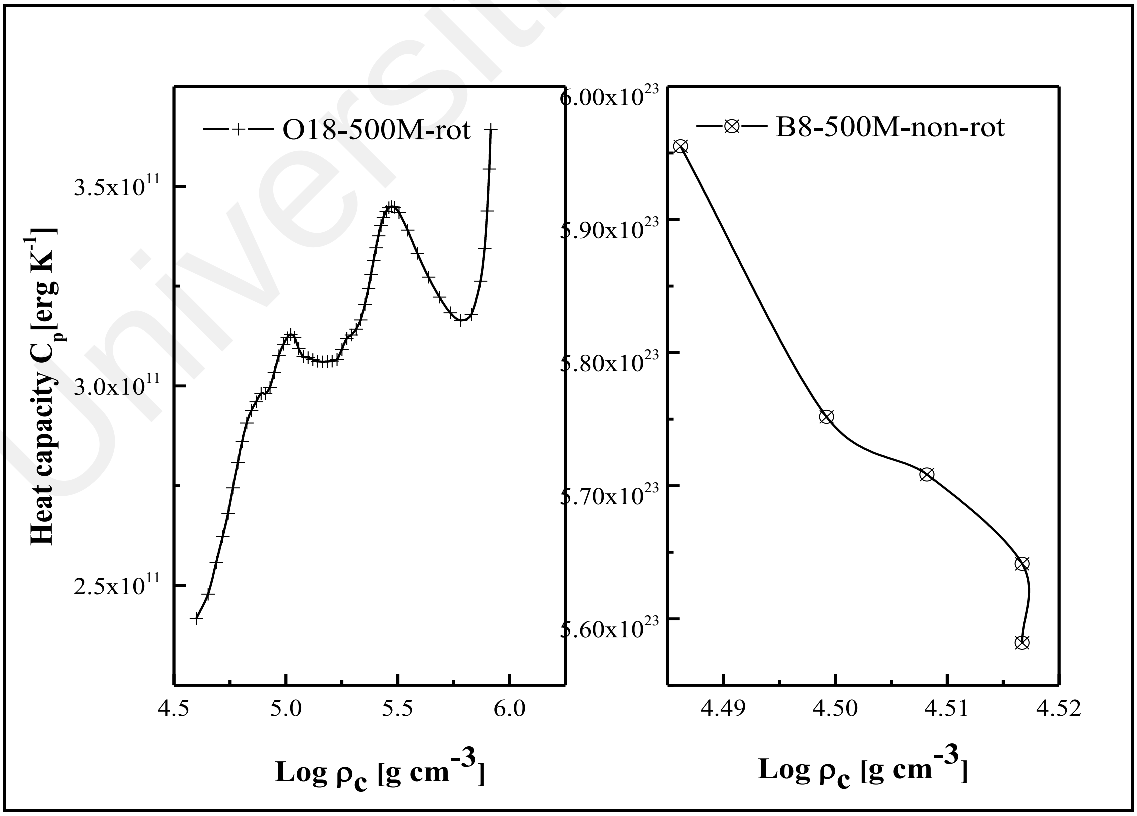

Figure 4.4: Evolution of specific heat capacities with density at constant pressure for rotating (left) and non-rotating (right) 500 M⊙ model. M represents M⊙ while R and NR represent rotation and non-rotation.

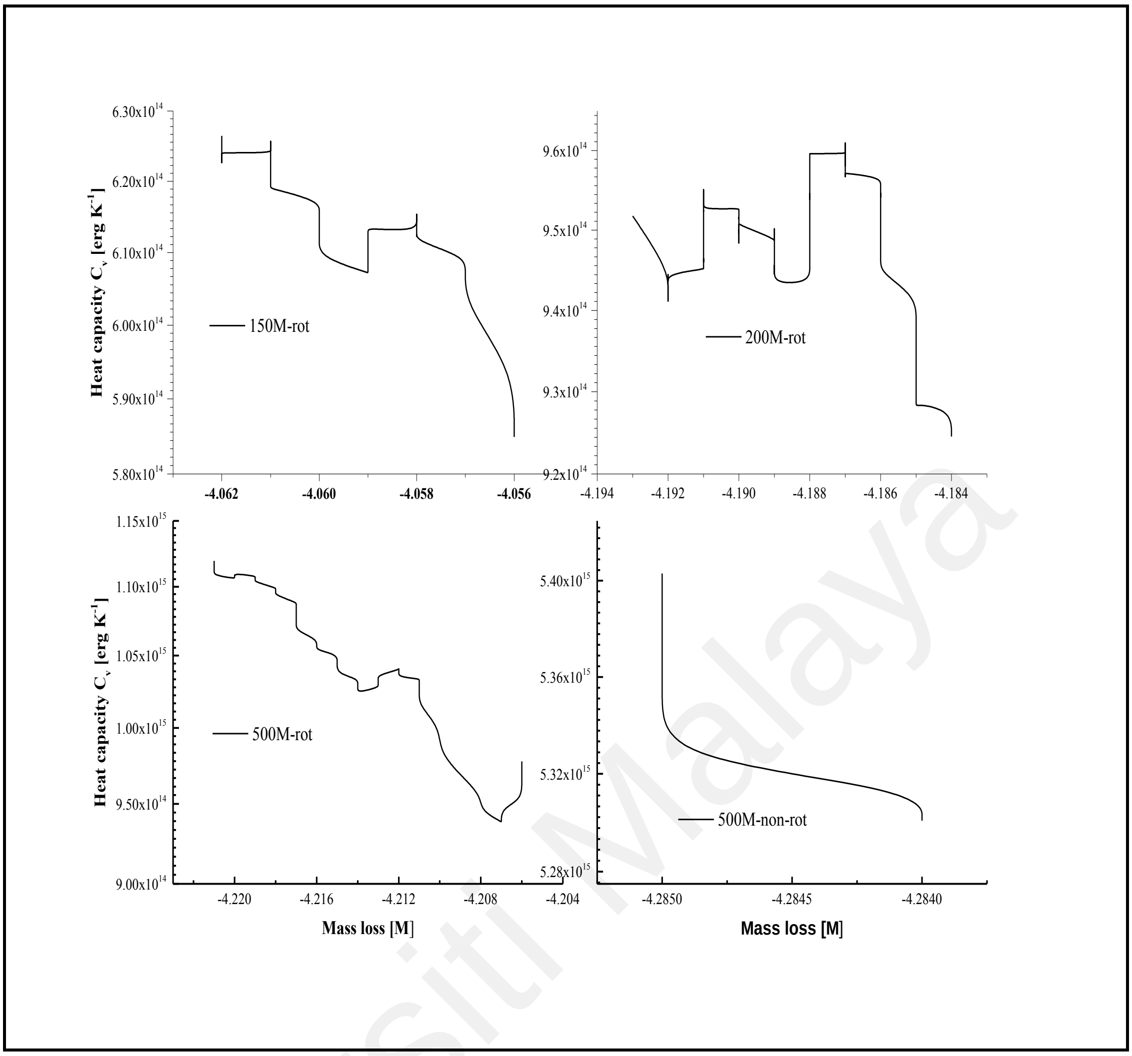

Figure 4.5: Track of heat capacities with mass loss for all models. Non-rotating model loses less mass and acquires higher heat capacities.

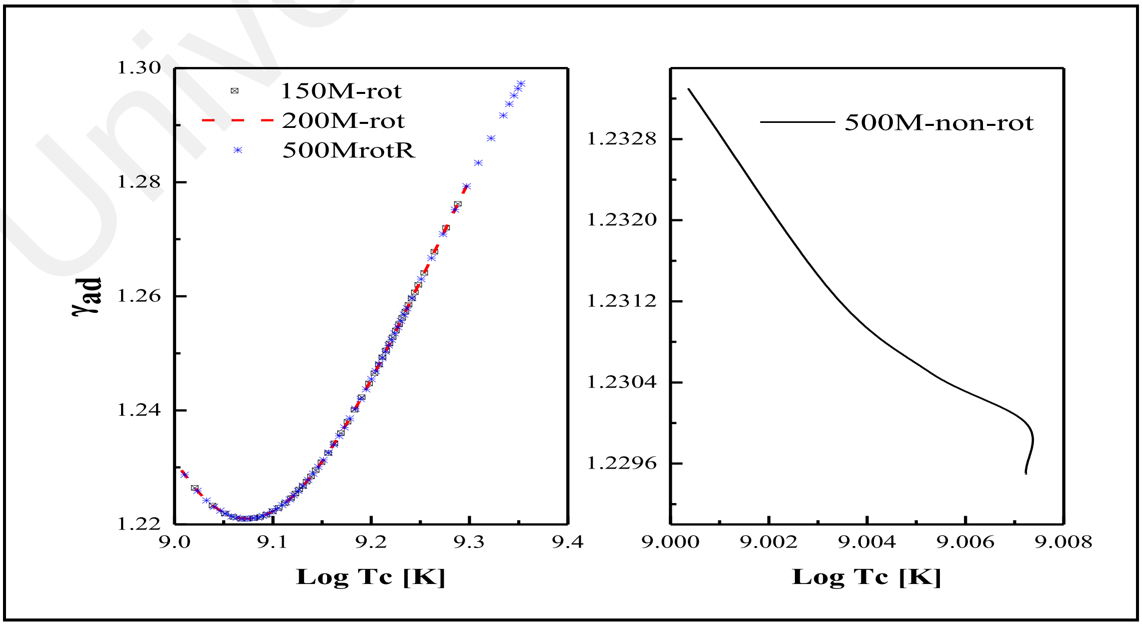

Figure 4.6: Effect of Pair-production instability on adiabatic index. M represents mass of the star in [M⊙], while, R & NR stands for rotating and non-rotating models.

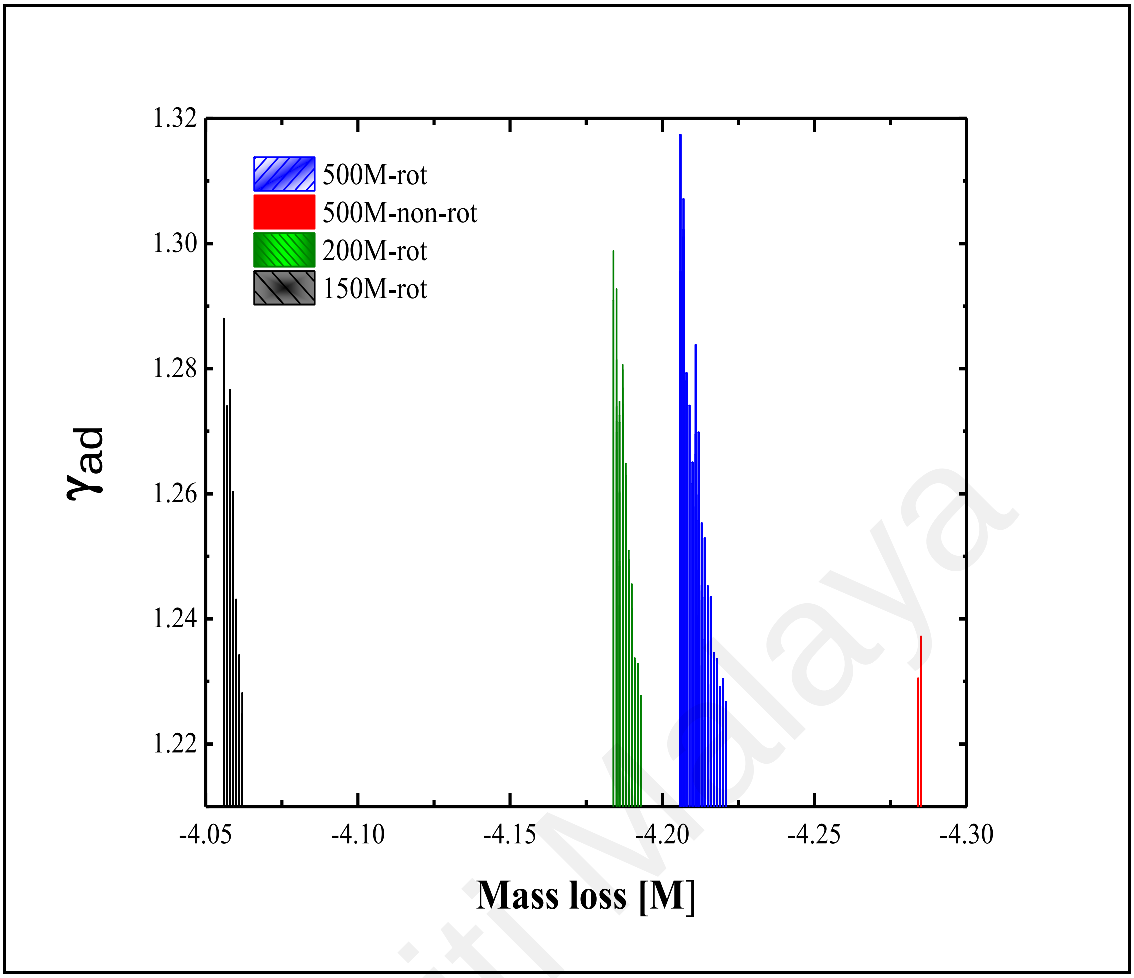

Figure 4.7: Adiabatic index with respect to mass loss for 150 M⊙ 200 M⊙ rotating models in SMC and 500 M⊙ rotating and non-rotating models in LMC.

4.1.4 Results Summary

Generally, the stability and/or instability of a star is determined by magnitude of its adiabatic index γ_{ad} (index). Any star predominantly occupied by an ideal gas or by classically degenerate electrons have adiabatic index $\gamma_{ad} = \frac{5}{3} = 1.6667$ and are therefore dynamically stable. However, for relativistic electron and positron, the adiabatic index is $\gamma_{ad} = \frac{4}{3} = 1.33333$ and such stars extend to neutral instability condition. Any further disturbance of such a star could results to its collapse and/or explosion. At very high temperature; the $\gamma_{ad} < \frac{4}{3}$ at core of the star and during pair production, this is a condition sufficient for generating instability in massive stars. However, since massive stars are dominated by radiation and gas of photon has $\gamma_{ad} = \frac{4}{3}$, the instability is only important for stars with $M_S/R_S << 1$ (Fowler, 1966). If $\gamma_{ad} > \frac{4}{3}$ the excess pressure leads to re-expansion so that high energy is restored. If however, $\gamma_{ad} < \frac{4}{3}$, the increase of pressure is insufficient to gain high energy. The compression will therefore reinforce itself and the situation is unstable on dynamical timescale, thus we have a criterion for dynamical stability; that is; $\gamma_{ad} > \frac{4}{3}$. It can be shown that a star that has $\gamma_{ad} > \frac{4}{3}$ everywhere is dynamically stable, and if $\gamma_{ad} = \frac{4}{3}$ it is neutrally stable and the compression leads to hydrostatic equilibrium. . If γ_{ad} is not constant within a star, the stability take place at an average value of γ_{ad} through which the star has a critical value 4/3. The radiation pressure brings γ_{ad} near this critical value, and as such very-massive stars are in neutral equilibrium, or attain a marginal stability. If on the other hand, a star approaches dynamical instability, there will be a point at which the usual method of perturbation used to obtain the condition of vibrational stability will cease to be applicable. However, in the case when the adiabatic index is $\gamma_{ad} < \frac{4}{3}$ in centres of massive stars, require further investigation, because the burden of the adiabatic change on the star increases stronger than pressure and hence the star after going through a gigantic instability would finally collapse.

In this section, we presents adiabatic effects of pair-production on the dynamical instability of selected progenitor models. Adiabatic quantities are evaluated by constructing a model into a thermodynamically consistent electron-positron equation of state (EoS) routines. At very high temperature and relatively low density; the production of electron-positron pairs in the centres of massive stars led the adiabatic index to below 4/3. It is observed that the adiabatic index, which creates disturbances in pair-production region is fundamentally positive with central temperature and density for all rotating models under consideration. Similarly, mass of oxygen cores in rotating models within the pair-production region has increased the adiabatic indices such that stars compresses, and whence induces an explosion to PISN, while mass loss and adiabatic index in non-rotating model exponentially decay. The increase of mass loss in rotating models and decrease of heat capacities in their instability regions show that only small quantity of heat energy, which is independent of chemical abundance, is required to keep the central temperature high. This high temperature is required for explosion and collapse of massive stars. The dynamic of many adiabatic quantities show similar pattern for rotating models. While, non-rotating model may, however, not be suitable for inducing the instability due to large mass loss to heat. Various effects of adiabatic properties on the dynamical instability of massive stars due to pair-production is examined in this section.

4.2 Electron-Positron Thermal Energy. Pressure and Entropy from the Instability Regions of Very-Massive Stars

In massive stars, very energetic photons are converted into electron-positron pairs just before ignition of any element heavier than oxygen and the star will enter a region (Figure 1.1) whereby energy needed to create rest mass of electron-positron pairs (at high entropy) softens the equation of state and reduce the adiabatic index to below 4/3 (Fraley, 1968), which subsequently leads to a violent contraction that activates nuclear explosion (Barkat et al., 1967; Bond et al., 1984; Carr et al., 1984; Chatzopoulos & Wheeler, 2012a; El Eid & Hilf, 1977; El Eid et al., 1983; Fraley, 1968; Ober et al., 1983; Rakavy & Shaviv, 1967; Stringfellow & Woosley, 1988; Wheeler, 1977). The thermal concentration of these pairs occur during advanced burning phase of the stars' evolution and causes a dynamic instability in the star (Woosley & Heger, 2015). This instability results in explosion of massive star as PISN. In this section, the thermal energies, pressure, and entropy of electron-positron gas produced in the instability regions of selected progenitor models is presented, discussed and analysed. As mentioned in previous chapters, any massive star that enter the instability region will be dynamically unstable and will eventually be disrupted by a powerful PISN explosion. At the explosion of the PISN and after a sufficient portion of the star passed out from unstable region, the pressure increases faster than gravitational forces, which reverse its collapse and the energy released in oxygen burning again disrupt the star and eject all materials with high velocity (Fraley, 1968), this energy, which obviously, increased the temperature and provide more pressure, is diverted into creation of electron-positron pairs. The thermal energy of these relativistic electron-positron pairs increases both temperature and density of the region through contraction of the star and indirectly triggered its explosion. This energy is, therefore, crucial to understanding the stellar cores and explosions (Blinnikov et al., 1996). Similarly, explosion disrupts the core of helium and other heavier nuclei and energy of this explosion increases with mass (Woosley et al., 2002). On the other hand, the dynamically unstable stars at certain core temperature also have an entropy which greatly affects its explosion (Fraley, 1968). In the following sub-section, we analyse those results one-after-another.

4.2.1 Electron-Positron Thermal Energy from Instability Regions of Massive Stars

In Table 4.3, results of maximum pair-production thermal energies from progenitor models under consideration is shown; first column is initial mass of star ($M_\odot$), second, third, fourth and fifth columns represents initial metallicity, critical rotational ratio, maximum central density (g cm^{-3}) and temperature (K) respectively, while last columns are maximum values of electron-positron thermal energies (erg g^{-1}) recorded against chemical abundances in the instability regions of the progenitor models respectively. The thermonuclear reactions began at core of the star with hydrogen and helium burnings which require low energy for nuclear fusion. The main focus-point here is where electron-positron pairs are produced at high energy, especially in late stages. At this region, however, nuclear reaction rates increases by a certain amount such that an energy is released due to oxygen mass consumption. This energy, by pairs of electron and positron, produced an oscillatory vibration within the instability region and is large enough to cause annihilation of pairs into neutrinos. The oscillations will soon die and the star evolves again slowly and enter the instability region. The process continues until all oxygen is completely exhausted from centre of the star. The stellar implosion got to higher density and temperature, and pair-production proceeds, such that generation of specific thermal energy inside the massive star is only poised by neutrino emission. Finally, as energy is spent by pair-production, the core loses its stability and begin to contract. This is evident, on account that, pair-production contributes only during advanced nuclear burning phases and production of electron-positron pairs in the instability region induces contraction of the stars and increases density-temperature of the region, which triggers quick annihilation of pairs. Electron-positron thermal energy is emitted during this contraction and is necessary and sufficient for release of the stars from contraction to its subsequent explosion. This energy is almost same for all nuclei beyond helium burning in the instability region. However, this later finding was predicted long ago by (Rakavy & Shaviv, 1967). The contraction of the star is overcome through increase of electron-positron thermal energy in the instability region. Figure 4.8, shows the increase of thermal energy when temperature of the region rises. It is shown here, that the progenitors are able to overcome their contraction through increase of thermal energy within the instability region. Figure 4.9 and Figure 4.10, is a comparison between electron-positron thermal energy with respect to central temperature and density from the progenitor models. Rotating models at SMC exhibits higher energies arising from higher temperature and density. This is, however, due to abundance of electron-positron pairs, that are produced in their centres. The thermal energy induced ability of star to reach the instability region as a result of low mass-loss and higher oxygen cores, which is contrary to models in LMC that loses more mass. This evidently affects the fates of the stars, such that electron-positron in centres of SMC models will fully annihilate into pair neutrinos, which may spark off their explosion as PISNe without remnant. As strong mass-loss drives stars further away from the instability region; adversely, thermal energy of pairs is reduced due to mass-loss and low oxygen cores as can be seen in Figure 4.11. However, metallicity also affects the thermal energy in a way that SMC models with lower metallicity than LMC suppresses the mass loss with greater amount of energy, and since 200 $M_\odot$ has greater mass of oxygen cores, it must have greater thermal energy in the instability-region to corresponds with its low metallicity and low mass loss. On the other hand, non-rotating 500 $M_\odot$ might have only reached the instability region due to low metallicity (only when compared with solar metallicity), which is capable of suppressing the mass-loss, such that thermal energy would be large enough for contraction of the star to convert electron-positron pairs into neutrinos. The graph in Figure 4.9 and Figure 4.10, indicates that instability is set in at temperature of around 1.01×10^9 K, 1.02×10^9, 1.02×10^9 K and 1.00×10^9 K corresponding to density 4.56×10^4 g cm^{-3}, 2.44×10^4 g cm^{-3}, 3.99×10^4 g cm^{-3} and 3.06×10^4 g cm^{-3} respectively for 150 $M_\odot$, 200 $M_\odot$ rotating and 500 $M_\odot$ rotating and non-rotating progenitor models. Inside the instability region, however, nuclear reaction rates increased by certain quantity; such that energy is released due to production of high mass oxygen-cores that is necessary for pair production.

Table 4.3: Maximum electron-positron thermal energy E_{max}[ergs g^{-1}] recorded from instability regions of very-massive stars.

Massive stars [M⊙]	Z_{in}	$\Omega/\Omega_{Crit\ rot}$	Density [g cm^{-3}]	T [K]	Thermal Energy E_{max}[ergs g^{-1}]					
					He3	**C13**	**O17**	**O18**	**Be7**	**B8**
150	0.002	0.40	3.42E+05	1.94E+09	2.57E+17	2.54E+17	2.57E+17	2.55E+17	2.57E+17	2.57E+17
200	0.002	0.40	3.02E+05	1.99E+09	3.29E+17	3.26E+17	3.29E+17	2.83E+17	3.29E+17	3.29E+17
500	0.006	0.40	8.25E+05	2.25E+09	2.31E+17	2.21E+17	2.31E+17	2.25E+17	2.32E+17	2.31E+17
500	0.006	0.00	3.29E+04	1.02E+09	4.01E+16	3.83E+16	4.01E+16	2.78E+16	4.01E+16	4.01E+16

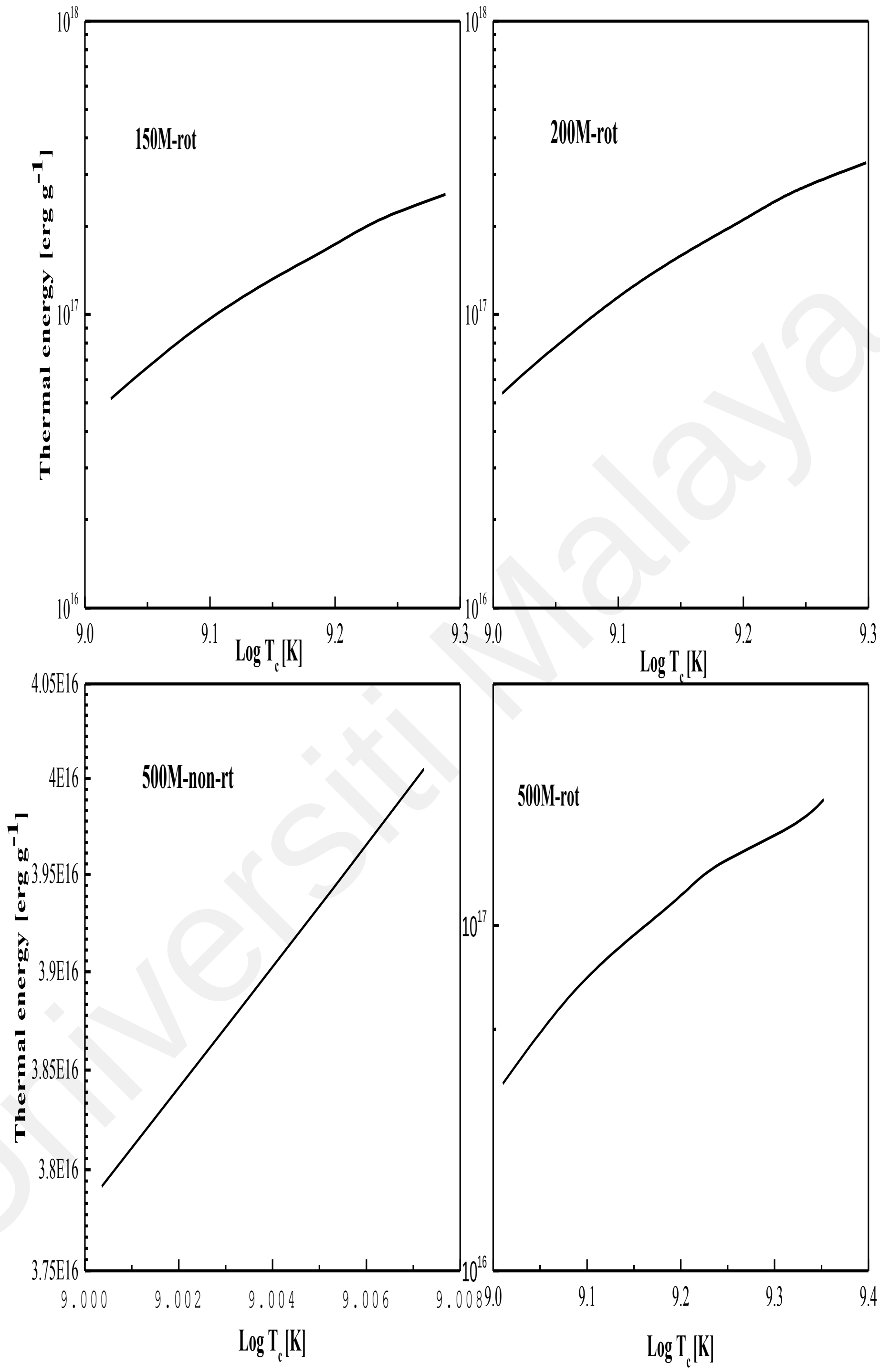

Figure 4.8: Electron-positron thermal energy with respect to temperature for 150 M⊙ (top-left) 200 M⊙ (top-right), 500 M⊙ non-rotating (down-left) and 500 M⊙ rotating (down-right) progenitor models.

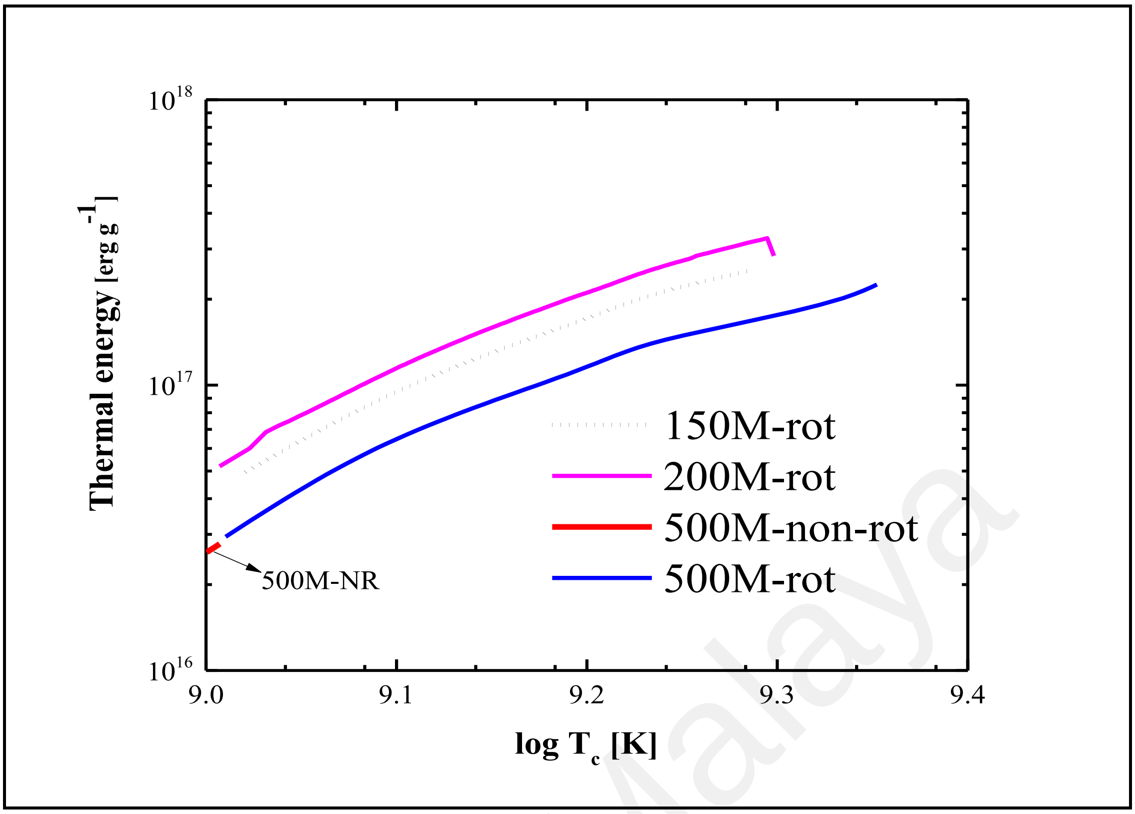

Figure 4.9: Electron-positron thermal energy for 150 M⊙ (black), 200 M⊙ (magenta) and 500 M⊙ rotating (blue) and non-rotating (red) models with respect to temperature.

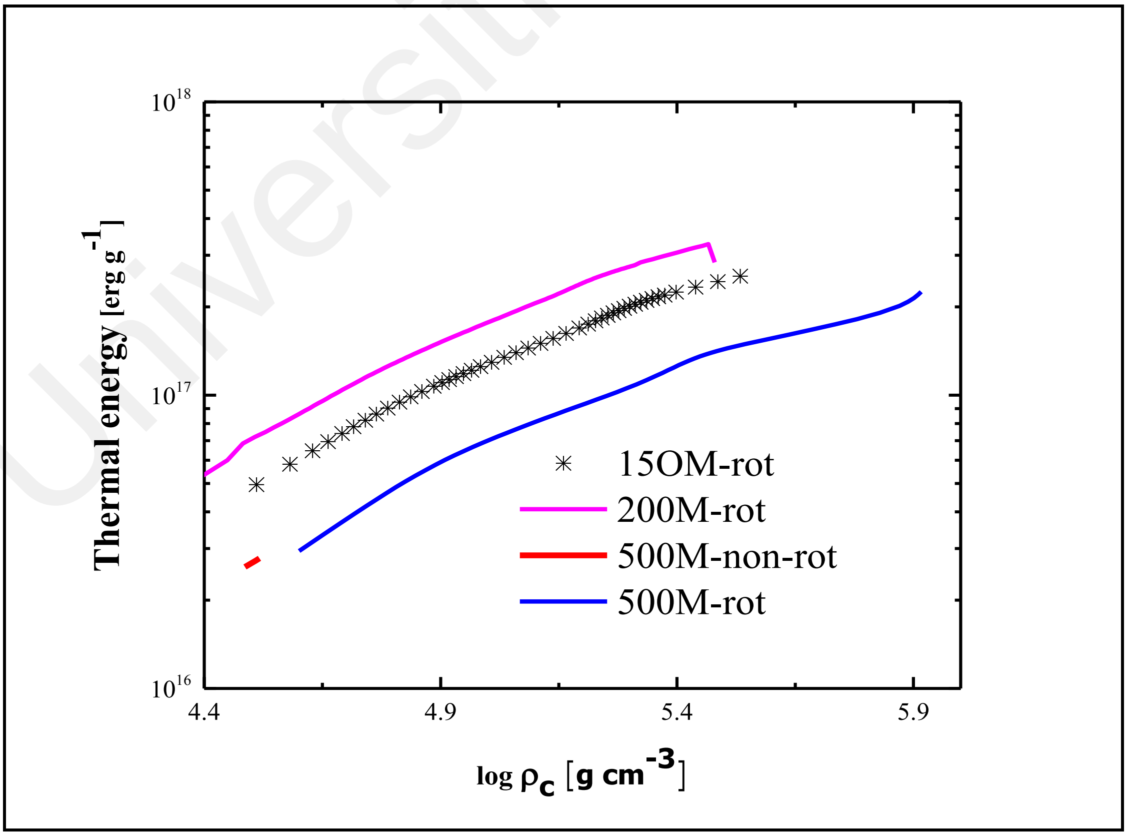

Figure 4.10: Electron-positron thermal energy for 150 M⊙ (black), 200 M⊙ (magenta) and 500 M⊙ rotating (blue) and non-rotating (red) models with respect to density.

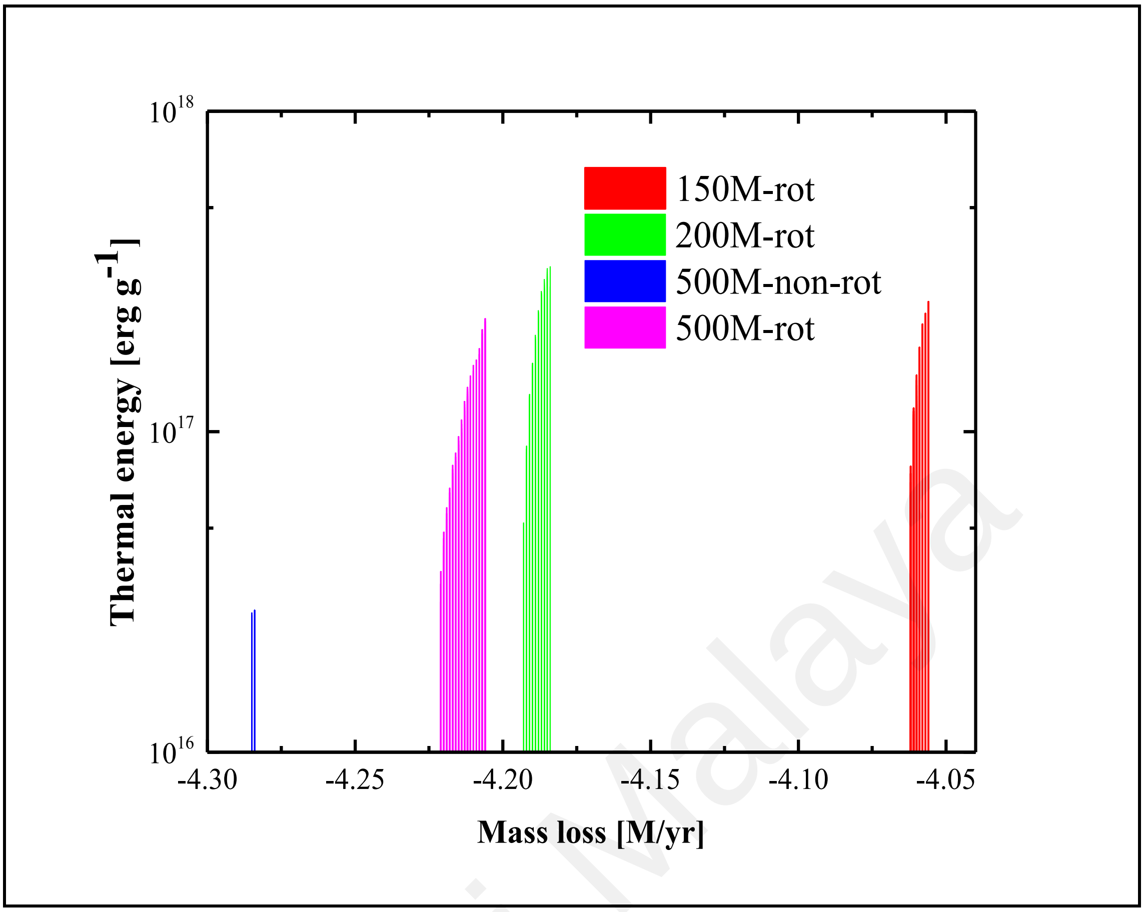

Figure 4.11: Electron-positron thermal energy [in erg g^{-1}] with respect to mass loss (in $M_{\odot}$ yr^{-1}].

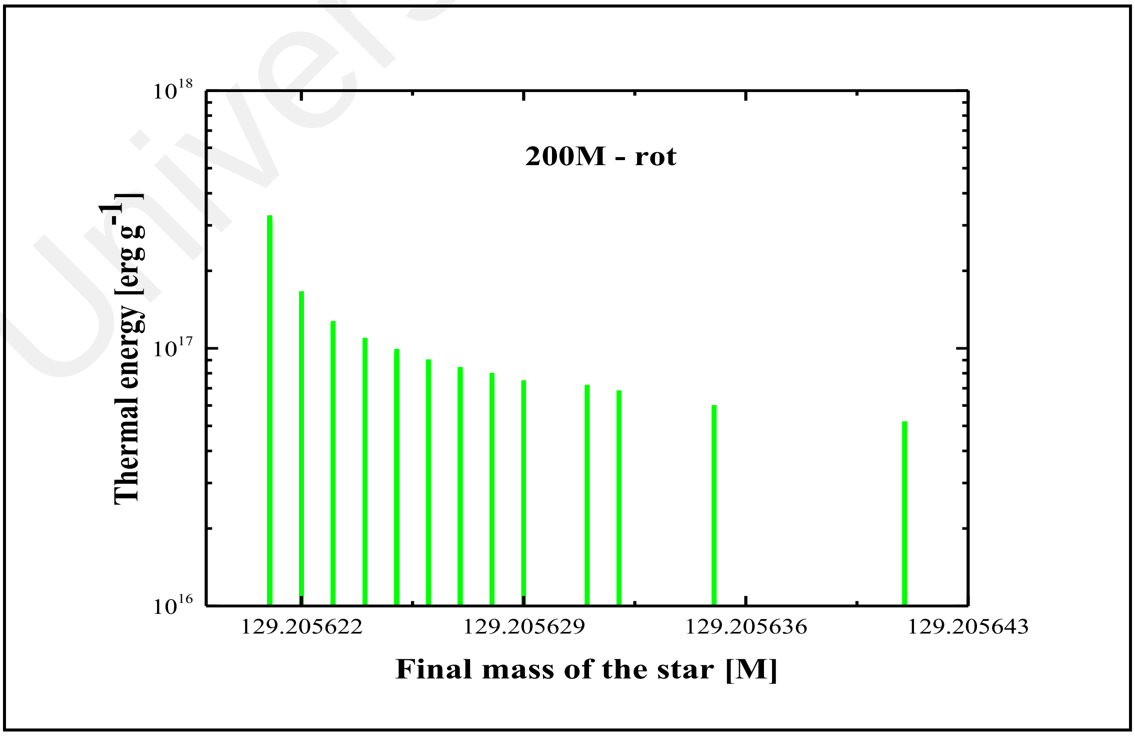

Figure 4.12: Thermal energies of electron-positron pairs with respect to final mass for 200 $M_{\odot}$.

In Figure 4.12 effect of mass of helium cores on electron-positron energy is examined. Bearing in mind that, helium mass directly affects explosion mechanism such that higher helium core mass reduce the instability threshold. In this figure (Figure 4.12) thermal energy decays when star approaches its final explosive mass (helium core mass), and it is interesting to note that, all rotating models show similar dynamic, differing only with non-rotating model (Figure 4.13). In case of non-rotating model; thermal energy is small compared to rotating models, and is almost uniform within the instability region until final mass of the star, where star will probably die or collapse. Models with highest helium mass (200 $M_{\odot}$) maintained greater stability and produced grater thermal energy. In low helium core mass (500 $M_{\odot}$) the thermal energy is steady and suddenly decay with respect to fractional rotation. The electron-positron thermal energy produced vibrational instability in density-temperature region and is sufficient enough to untie the stars from contraction and annihilate the electron-positron pairs into neutrinos, which drives explosion of the star. This vibration dies very quickly and the star evolves back to the instability region. The process continues until all oxygen is completely exhausted from center of the star and it is completely exploded without any remnant.

4.2.2 Relativistic Electron-Positron Pressure from Instability Regions of Very-Massive Stars

The total pressure, as a combination of ideal gas, radiation, and in the end partially degenerate electrons, keep up the star against gravitational force. However, at end of Fe-burning during evolution of the stars, there is no nuclear burning that could proceed to create pressure needed to keep the star against gravitational collapse. The star at this situation is dominated by pair-production and therefore begins to implode. In Figure 4.14 evaluated pressure with temperature for 200 $M_{\odot}$ and 500 $M_{\odot}$ rotating progenitor models is shown.

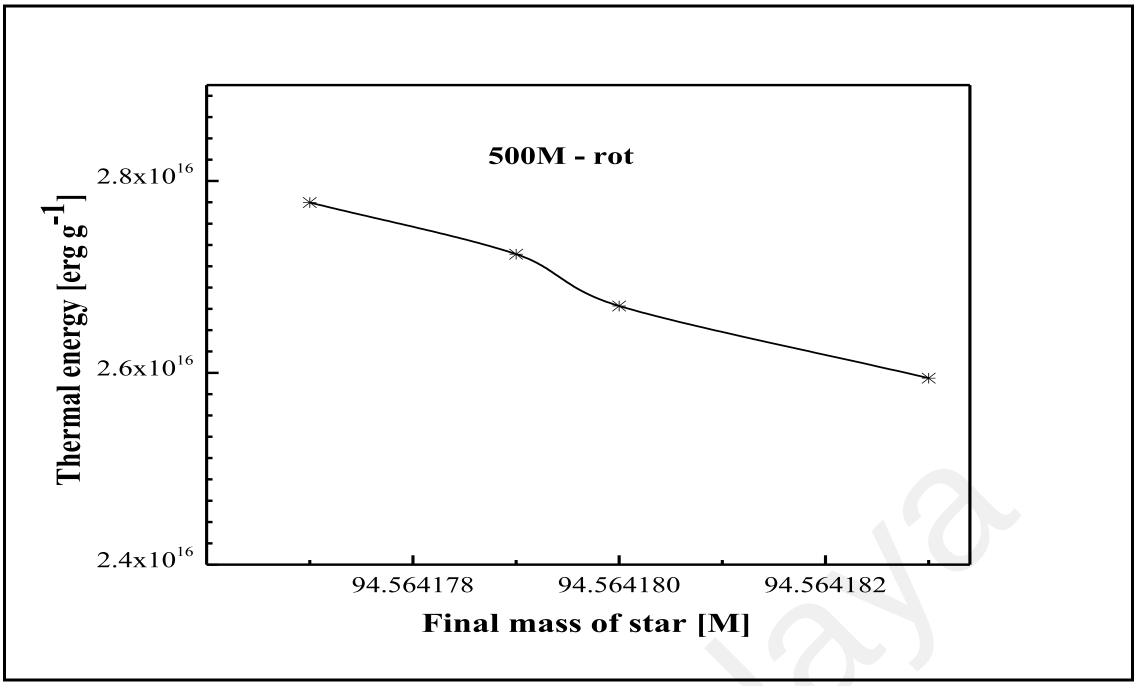

Figure 4.13: Thermal energy of electron-positron pairs with final mass for non-rotating 500 M⊙ model.

It is important to note that, although electron-positron pressure in all models increases at high temperature, it is, however, insignificant in density-temperature range. This is because only electron degeneracy and radiation are important for pressure in the evolution process. The pressure increase within the instability region could only signify the ideal property of the Fermi gas inside the region. The pressure increase, which is arising from increase in temperature of the instability region, is also manifested from increase in nuclear force striking boundaries of the region. In Table 4.4, maximum values of electron-positron pressure from models under consideration are summarized; the first column is initial mass (M⊙), second, third, fourth and fifth columns represents metallicity, critical rotational ratio, maximum central density (g cm^{-3}) and temperature (10^9 K) respectively, while last columns are maximum pressure (erg cm^{-3}) of electron-positron pairs against nuclear abundances in the instability region. The low pressure indicates where temperature and density are relatively inside the instability region of pair- production range near advanced nuclear reactions. This table also shows that electron-positron pressure is also independent of nuclear abundance inside the region.

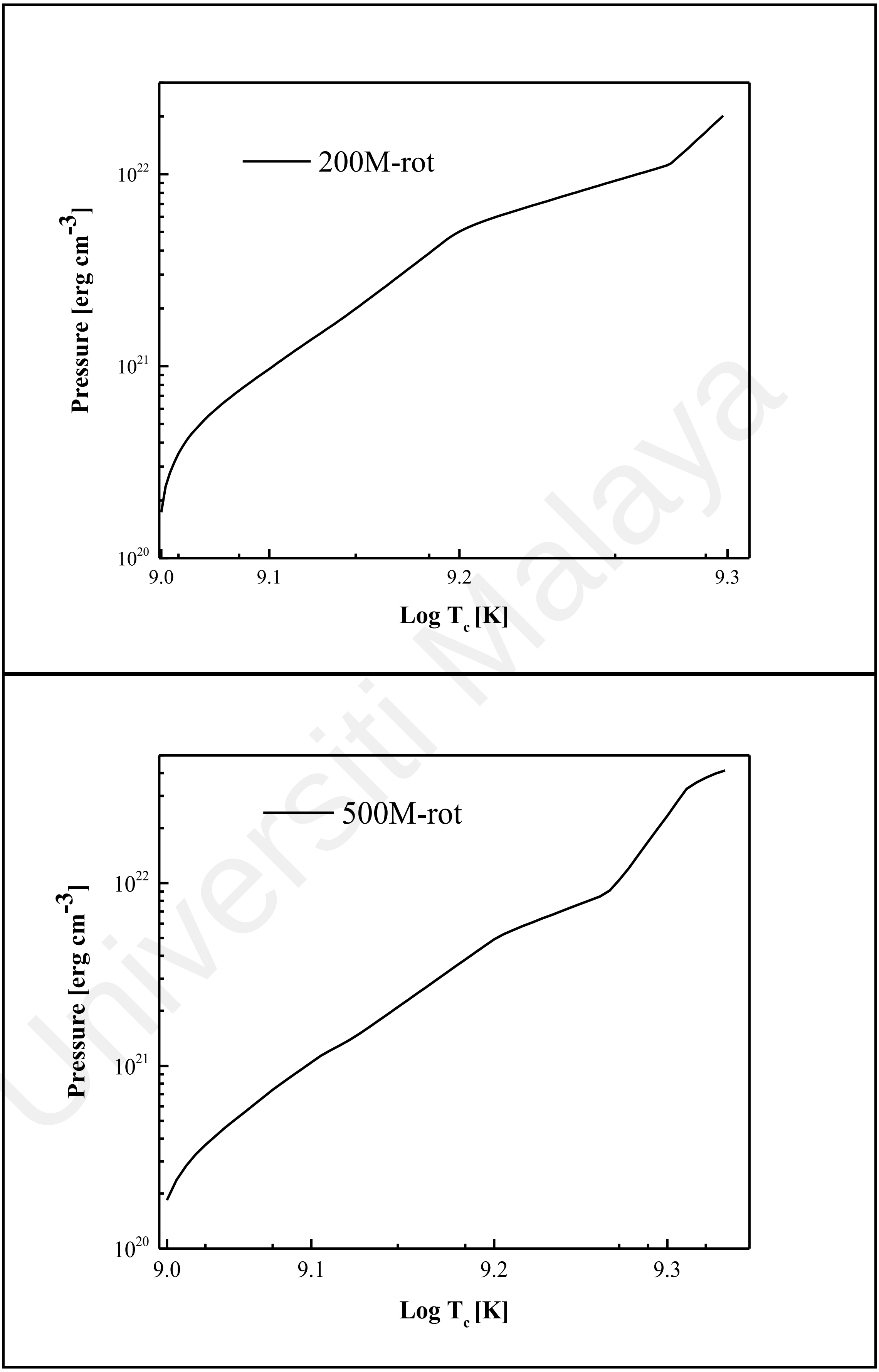

Figure 4.14: Electron-positron pressure with temperature within the instability regions of 200 M⊙ (up) and 500 M⊙ (bottom) rotating progenitor models

4.2.3 Entropy due to Pair-Production from the Instability Regions of Massive Stars

The electron-positron entropy, as presented in Table 4.5, is uniform within the instability regions of the stars irrespective of nuclear abundance. Entropy is the microscopic uncertainties in the nuclei to avoid instability region. There is no steep decrease in density around the centre nor a sharp increase in entropy which is usually associated with oxygen-burning shell. The entropy in the core and its surrounding are unnaturally large and changes by rising in response to burning, but decline when neutrino loss is reached. This pattern is repeated until fuels are exhausted causing mass to reduce below a critical value. The final contraction phase followed, and stellar core settled into stable silicon shell burning with no more instability pulses. However, uncertainties affecting many of the nuclei at early evolution of stars is caused by low thermal energy to reach pair-production limit.

4.2.4 Results Summary

This section discussed electron-positron thermal energies, pressure, and entropy from instability regions of very-massive stars with carbon-oxygen cores in the range of 60 $M_\odot < M_{CO} < 133$ $M_\odot$. Rotating 200$M_\odot$ model recorded highest electron-positron thermal energy of about 3.29×10^{17} [erg g^{-1}] while non-rotating 500$M_\odot$ model almost lose all its electron-positron energy and collapse before reaching the instability region.

Table 4.4: Maximum relativistic electron-positron pressure P_{max} [erg cm^{-3}] recorded against chemical composition within the instability regions of very-massive stars.

Massive stars [M$_\odot$]	Z_{in}	$\Omega/\Omega_{Crit\ rot}$	Density [g cm^{-3}]	T [K]	P_{max} [erg cm^{-3}]					
					He3	**C13**	**O17**	**O18**	**Be7**	**B8**
150	0.002	0.40	3.42E+05	1.94E+09	1.76E+22	1.76E+22	1.76E+22	1.76E+22	1.76E+22	1.76E+22
200	0.002	0.40	3.02E+05	1.99E+09	2.02E+22	2.02E+22	2.02E+22	1.20E+22	2.02E+22	2.02E+22
500	0.006	0.40	8.25E+05	2.25E+09	4.14E+22	4.15E+22	4.14E+22	4.14E+22	4.14E+22	4.14E+22
500	0.006	0.00	3.29E+04	1.02E+09	1.73E+20	1.74E+20	1.73E+20	2.07E+20	1.73E+20	1.73E+20

Table 4.5: Maximum relativistic electron-positron entropy S_{max}[erg g^{-1} K^{-1}] recorded against chemical composition within the instability regions of very-massive stars.

Massive stars[M$_\odot$]	Z_{in}	$\Omega/\Omega_{Crit\ rot}$	Density [g cm^{-3}]	T [K]	S_{max}[erg g^{-1} K^{-1}]					
					He3	**C13**	**O17**	**O18**	**Be7**	**B8**
150	0.002	0.40	3.42E+05	1.94E+09	1.59E+08	1.59E+08	1.59E+08	1.59E+08	1.59E+08	1.59E+08
200	0.002	0.40	3.02E+05	1.99E+09	1.99E+08	1.99E+08	1.99E+08	1.87E+08	1.99E+08	1.99E+08
500	0.006	0.40	8.25E+05	2.25E+09	1.25E+08	1.25E+08	1.25E+08	1.25E+08	1.25E+08	1.25E+08
500	0.006	0.00	3.29E+04	1.02E+09	4.46E+07	4.46E+07	4.46E+07	5.12E+07	4.46E+07	4.46E+07

This energy is needed to overcome contraction of the stars and for complete annihilation of electron-positron into pair neutrinos. The electron-positron pressure is insignificant in density-temperature range because only electron degeneracy and radiation are contributes immensely for pressure during the evolution process.

4.3 Pair Neutrino Energy-Loss from the Instability Regions of Very-Massive Stars

Stellar evolutions and fates are equally and strongly affected by many other physical quantities, such as cooling neutrino energy-loss. The emission of neutrinos from massive stars is an important energy-loss mechanism at high temperature and density. When interior of a massive star is sufficiently hot, nuclear reactions provide energy-loss as radiation and neutrinos, which will modify the composition, such that the structure of the star changes with time (Woosley et al., 2002). Stellar evolution, beyond helium burning, is greatly accelerated by electron-positron pair annihilation, and energy generation by thermonuclear reactions at centre of the star is only balanced by emission of neutrinos mainly from pair-production process (Arnett, 1996). The neutrinos at different flavours sways the remnant gravitational energy of the star and drives its evolution from initially hot to finally cold state (Janka, 2016; Janka, 2017). Neutrinos emission unlocks key issues in the explosion of massive stars and serve as proven sources of information about astrophysical objects and phenomena (Odrzywolek & Plewa, 2011). Irrespective of its mass, a star during its late evolutionary stages lose energy through neutrinos. For instance, large amount of neutrinos and antineutrinos are emitted in proto-neutron star of a core-collapse supernova, and then quickly disperse in ~10s long burst which then carriers most of energies liberated in collapse of the star, and then lead to a neutrino-driven wind that propagates through the star and induces a supernova explosion (Lunardini, 2015). Although, Arnett (1996) argued that neutrino emission from supernovae is negligible in many explosion models due to slow timescale of weak interaction rates compared to hydrodynamic timescales, but on contrary, Odrzywolek and Plewa (2011) suggests that it is possible that certain amount of energy emitted via neutrinos is significant compared to energy produced in thermonuclear burning, and in such case, neutrino energy-loss play an important role in explosion dynamics, and in very-massive star, neutrino signals could unequivocally ascertain its explosion. And hence, in either case, neutrinos provide important insights into supernova explosion mechanism. Pair neutrino emission is the dominant cooling process for massive stars and is very essential in their explosion, and therefore adequate information about neutrinos spectra and energy-loss at endpoints of stellar evolution models would help in addressing supernova research and may allow for distinguishing the triggering mechanisms involve in PISN explosions. The energy-loss rate due to neutrino emission attracts attention from both weak nuclear reactions and thermal processes. This method of cooling differs basically from radiative, convective or conductive cooling in massive stars. The basic differences between them is the fact that neutrino emission from core of stars immediately carries all of its energy completely out of the star. Neutrino emission is just like having a local refrigerator that cools stars' core. In this sections, we present results obtained from numerical calculations of neutrino energy-loss emitted from very-massive stars under consideration.

In Table 4.6, summary of evaluated neutrino energy-loss is presented together with temperature and density from the instability regions of 150 $M_\odot$, 200 $M_\odot$ rotating and 500 $M_\odot$ rotating and non-rotating progenitor models. In this table, first three-columns represent neutrino energy-loss, temperature, and density within the instability regions from 150 $M_\odot$ model respectively. The remaining columns are from 200 $M_\odot$, 500 $M_\odot$ rotating and non-rotating models. In the instability region and after contraction of stars, electron-positron pairs completely annihilate into pair neutrinos, and the star cools by neutrino emission, which ignites its explosion in the end of carbon-oxygen core mass. The dynamic of these annihilation processes with respect to neutrino energy-loss can be seen in Figure 4.15 below. This figure shows that pairs converts their thermal energies into neutrino emissions in rotating models. Non-rotating model which has lowest electron-positron thermal energy is unable to emit many neutrinos, and as such, it collapses before explosion. The neutrino energy-loss within the instability regions of rotating SMC and LMC models increases rapidly with central temperature of the region, as can be seen in Figure 4.16, this is as a result of their high electron-positron thermal energies which is induced by rotation that subsequently reduced mass-loss from the stars. Neutrino energy-loss increase with respect to density in the instability region as can be seen in Figure 4.18, this trend will continue until end of pair neutrino emission range; when density is higher and pair neutrino emission begin to decline. However, this is only depicted in rotating models, non-rotating model differs slightly from this scenario, as can be seen in Figure 4.17. It is found that neutrino energy-loss in non-rotating model stayed almost constant before final collapse of the star. Low metallicity, which suppresses mass loss, coupled with non-rotation effects in 500 $M_{\odot}$ non-rotating models prevents the electron-positron pairs to significantly overcome contraction of the star and to converts pairs into neutrinos. This is also manifested in track of neutrino energy-loss with mass loss, as shown in Figure 4.17 (whereby non-rotating model lacks energy and collapses before neutrinos). On mass-loss effects; recalling that rotating models loses less mass than non-rotating, and electron-positron thermal energies of rotating models are much greater than non-rotating, so also neutrino energy-loss appeared to be in same pattern of evolution. In Figure 4.17, rotating models would emits more neutrinos than non-rotating, and as such, they could be able to explode as PISNe. It should be stressed here that non-rotating models are in-adequate to explode as PISN, and should either die or collapse prior to reaching the instability region.

Table 4.6: Neutrino energy-loss rates from instability regions of 150 M$_\odot$, 200 M$_\odot$ rotating and 500 M$_\odot$ rotating and non-rotating progenitor models arising from electron-positron pair annihilation.

150 M$_\odot$			200 M$_\odot$			500 M$_\odot$-R			500 M$_\odot$-NR		
Log ρ [g cm^{-3}]	**Log T [K]**	Energy-loss [erg cm^{-3} s^{-1}]	**Log ρ [g cm^{-3}]**	**Log T [K]**	Energy-loss [erg cm^{-3} s^{-1}]	**Log ρ [g cm^{-3}]**	**Log T [K]**	Energy-loss [erg cm^{-3} s^{-1}]	**Log ρ [g cm^{-3}]**	**Log T [K]**	Energy-loss [erg cm^{-3} s^{-1}]
4.510363	9.020669	2.71E+09	4.386771	9.007146	2.19E+09	4.600555	9.010304	1.51E+09	4.486165	9.00036	1.35E+09
4.581409	9.038801	4.43E+09	4.448804	9.022925	3.39E+09	4.652342	9.023318	2.16E+09	4.499222	9.003263	1.46E+09
4.629216	9.051245	6.15E+09	4.481885	9.03142	4.28E+09	4.68869	9.03262	2.77E+09	4.508188	9.005278	1.54E+09
4.661907	9.059858	7.69E+09	4.507014	9.037934	5.09E+09	4.718137	9.040263	3.40E+09	4.516695	9.007229	1.63E+09
4.691303	9.067665	9.39E+09	4.529402	9.043764	5.95E+09	4.742177	9.046544	4.02E+09	4.516695	9.007229	1.63E+09
4.71597	9.074245	1.11E+10	4.547442	9.04848	6.74E+09	4.763921	9.052259	4.67E+09	4.516695	9.007229	1.63E+09
4.74083	9.080866	1.31E+10	4.563423	9.052696	7.52E+09	4.785843	9.058022	5.42E+09	4.516695	9.007229	1.63E+09
4.764172	9.087067	1.53E+10	4.577332	9.05637	8.28E+09	4.806014	9.063314	6.21E+09	4.516695	9.007229	1.63E+09
4.788061	9.093374	1.78E+10	4.589417	9.059577	9.00E+09	4.826248	9.068597	7.10E+09	4.516695	9.007229	1.63E+09
4.812978	9.099897	2.08E+10	4.600967	9.062654	9.74E+09	4.846852	9.073935	8.12E+09	4.516695	9.007229	1.63E+09
4.836507	9.105995	2.40E+10	4.61208	9.065621	1.05E+10	4.867887	9.07933	9.28E+09	4.516695	9.007229	1.63E+09
4.860476	9.112145	2.77E+10	4.622823	9.068501	1.13E+10	4.889423	9.084792	1.06E+10	4.516695	9.007229	1.63E+09
4.885395	9.118502	3.21E+10	4.632123	9.071003	1.21E+10	4.909202	9.089754	1.19E+10	4.516695	9.007229	1.63E+09
4.903172	9.123018	3.56E+10	4.641631	9.073558	1.29E+10	4.928962	9.094661	1.34E+10	4.516695	9.007229	1.63E+09
4.918183	9.126825	3.88E+10	4.65088	9.076055	1.37E+10	4.948953	9.099577	1.51E+10	4.516695	9.007229	1.63E+09

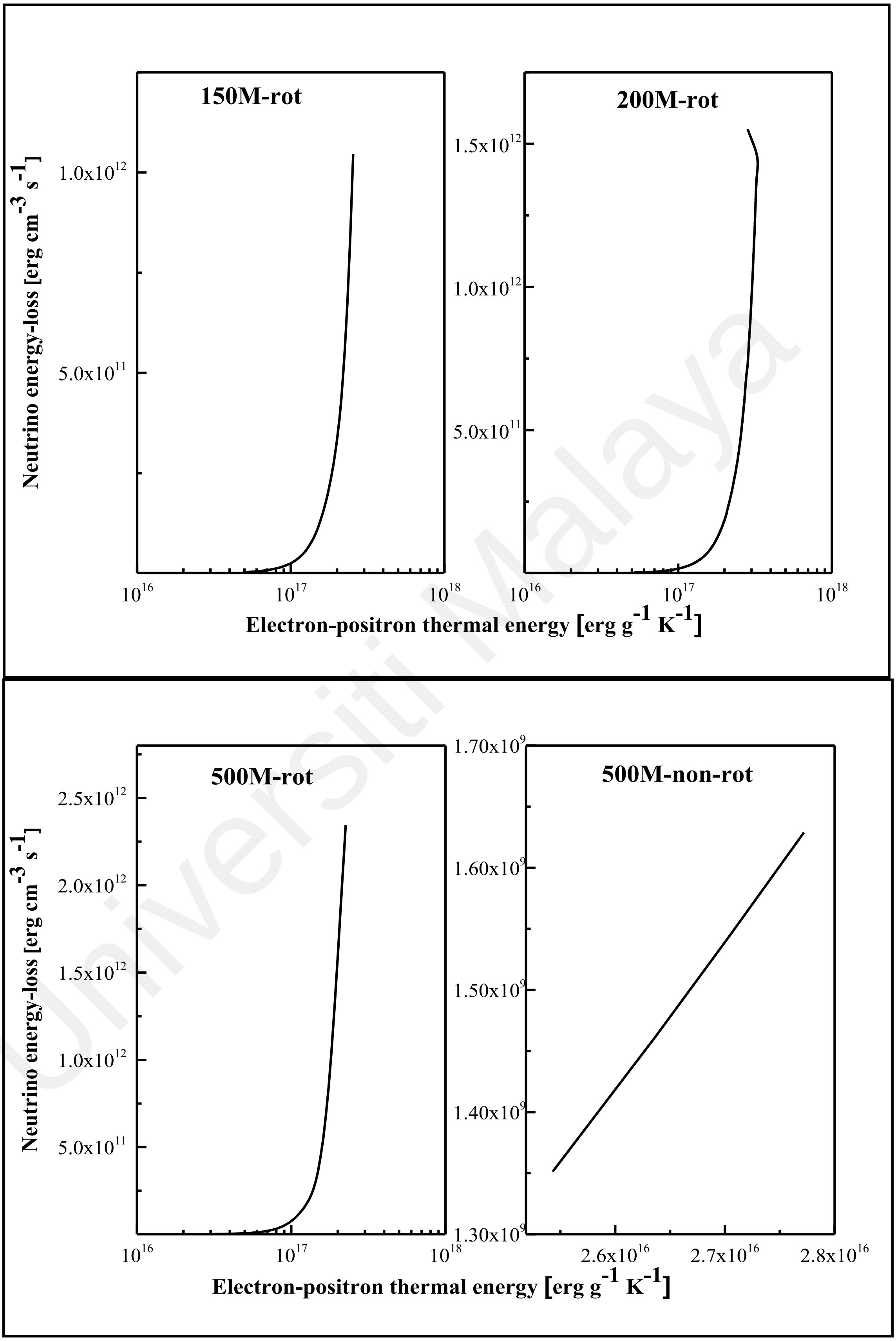

Figure 4.15: Neutrino energy-loss plotted with electron-positron thermal energy in the instability regions of 150 M⊙, 200 M⊙ rotating models (top - left & right) and 500 M⊙ rotating and non-rotating models (down - left & right).

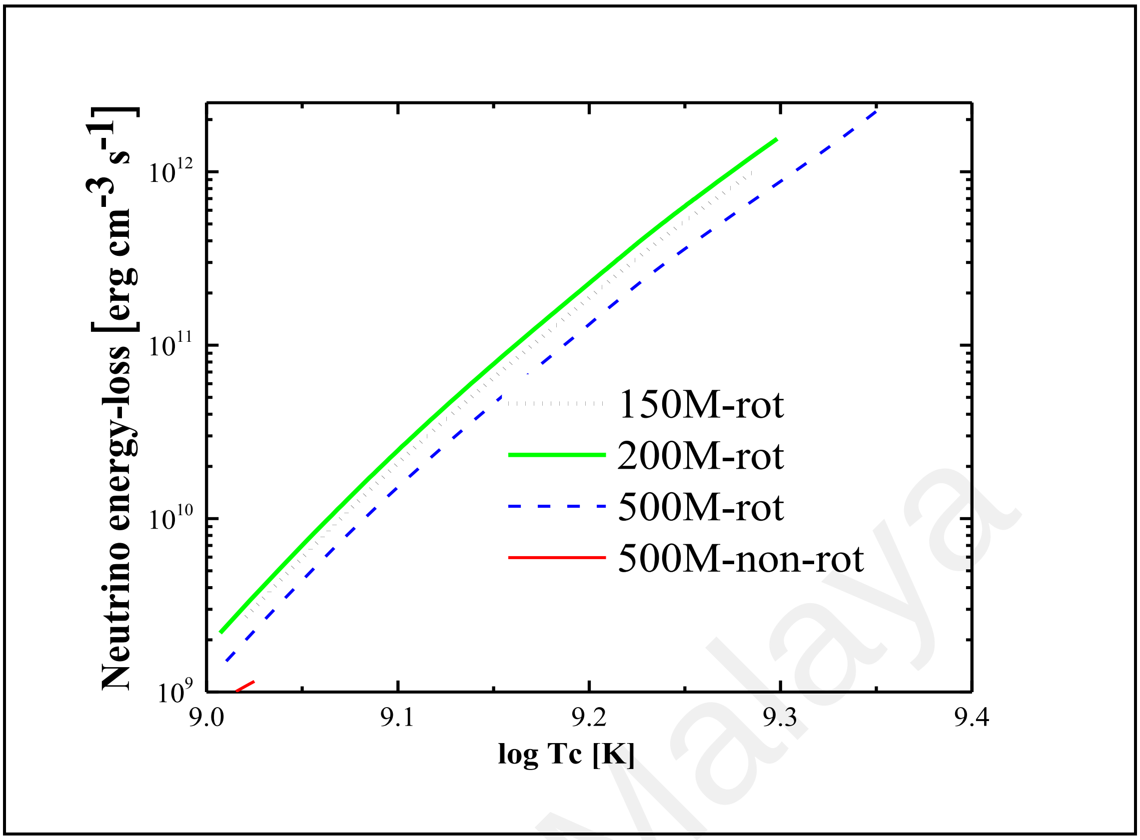

Figure 4.16: Track of neutrino energy-loss with respect to temperature in the pair-instability regions of 150 M⊙ (dotted line), 200 M⊙ (green line), rotating 500 M⊙ (dashed-blue) and non-rotating 500 M⊙ (red line).

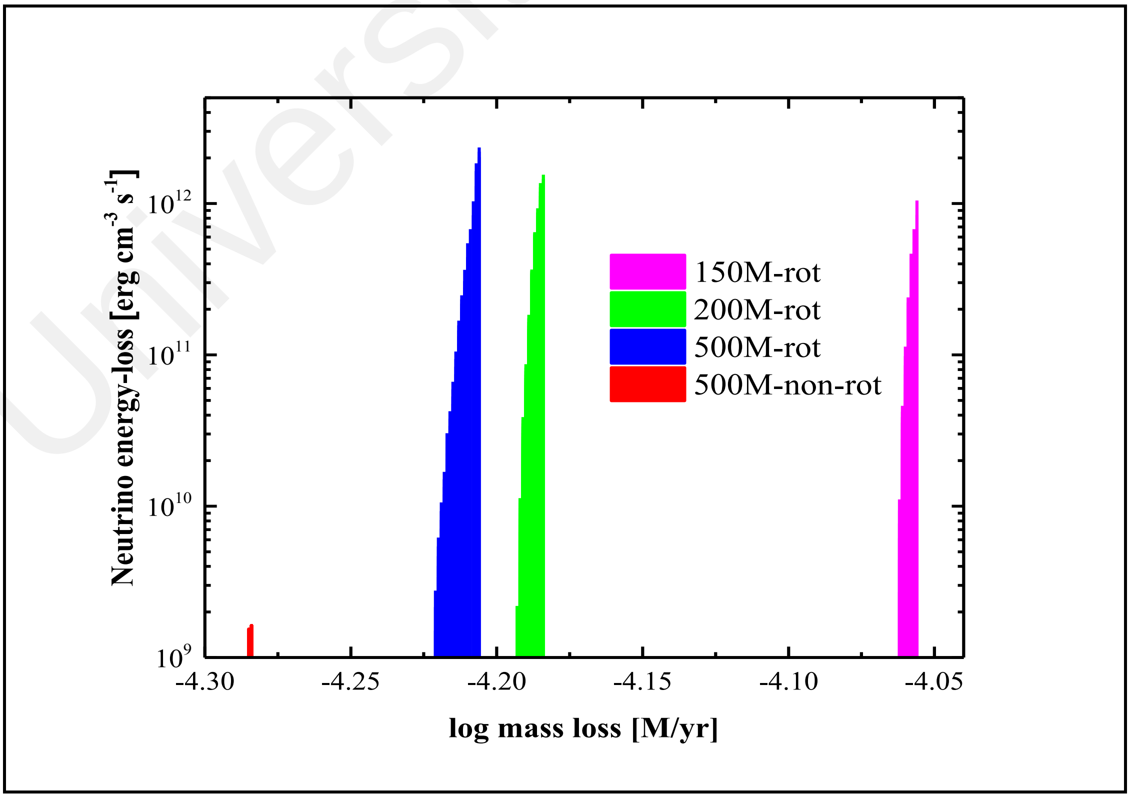

Figure 4.17: Neutrino energy loss against mass loss from 150 M⊙ (magenta), 200 M⊙ (green), 500 M⊙ rotating (blue), and nonrotating (red) models.

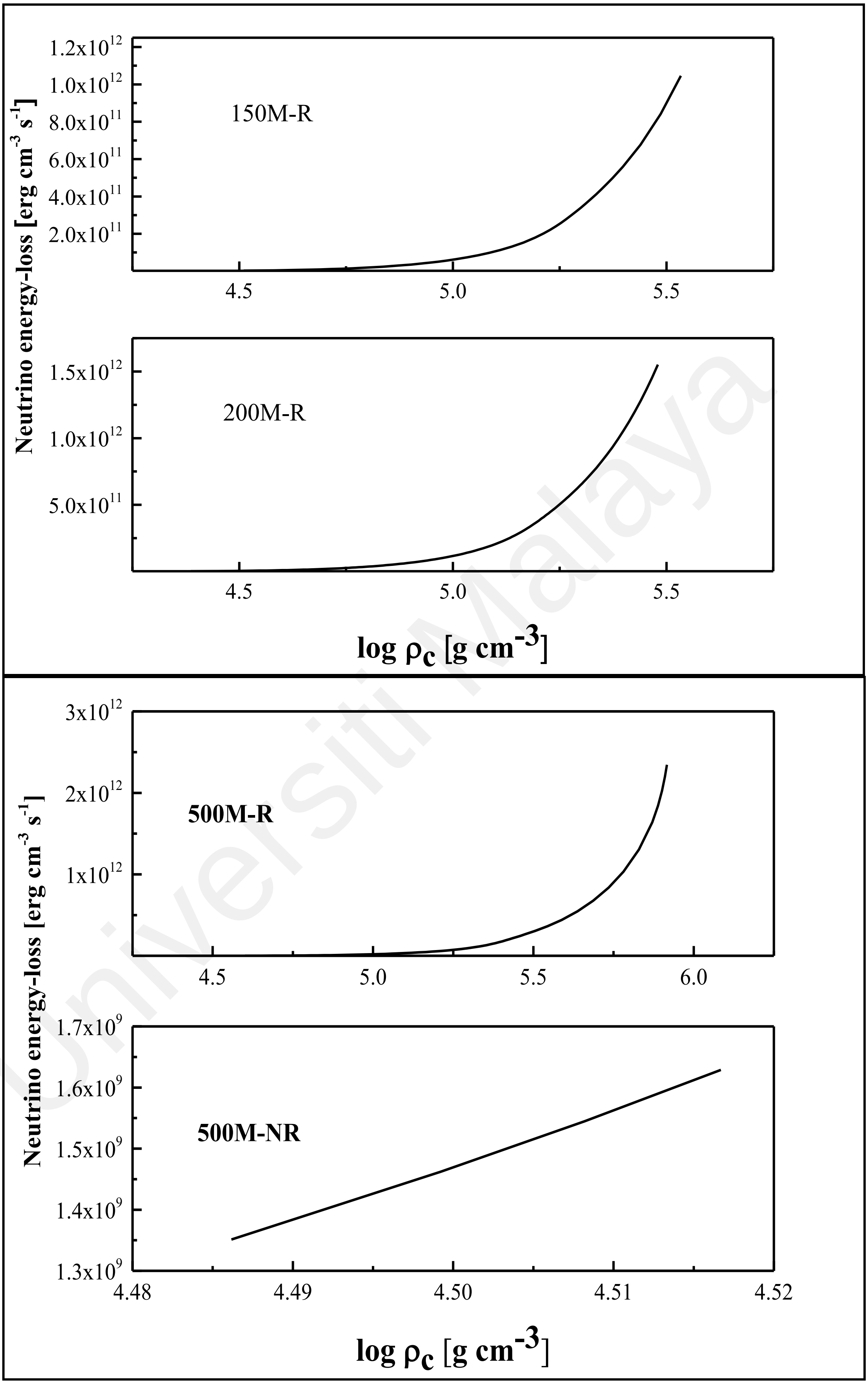

Figure 4.18: Neutrino energy-loss with central density from 150 M⊙ and 200 M⊙ (top-1st & 2nd) and 500 M⊙ rotating and non-rotating (down-1st & 2nd) model.

Figure 4.18, represents dynamics of neutrino energy-loss within the instability regions of the stars. Rotating models show clear instability and explosion process take place before the star die. The density and temperature of the region keep rising until the star is able to turn into explosion when its core has been cooled by neutrino emission. The non-rotating model failed to attain to density and temperature that will enable it to undergo full instability so as to generate enough electron-positron thermal energy needed to trigger annihilation of pairs into neutrinos which cools its core.

4.3.1 Results Summary

This section discussed numerical results obtained from calculations of energy-loss rates due to pair neutrino process in the instability regions of very-massive stars with carbon-oxygen cores within the range of 60 $M_{\odot} < M_{CO} < 133\ M_{\odot}$. High thermal energy of pair-production is needed to overcome contraction of stars and for complete annihilation of electron-positrons into pair neutrinos. The section analyses results found from this calculation, especially as it affects end fates of the stars.

4.4 Temperature and Density profiles for 120, 150, 200, 300 and 500 M⊙ stellar models

The neutrino energy loss from thermal processes is 100% dependent on temperature and density of the star. We must therefore understand the profiles of these two important quantities, especially as it influence production of neutrino flux which is necessary for calculations of energy-loss of neutrinos via oscillations. The density is however, dependent on radius of the star, such that at the surface of the star, the density is low and increases towards the centre of the star for both rotating and non-rotating models. In Figure 4.19, we have shown graphs of temperature and normalised radius of the stars against a normalised mass of the particular star.

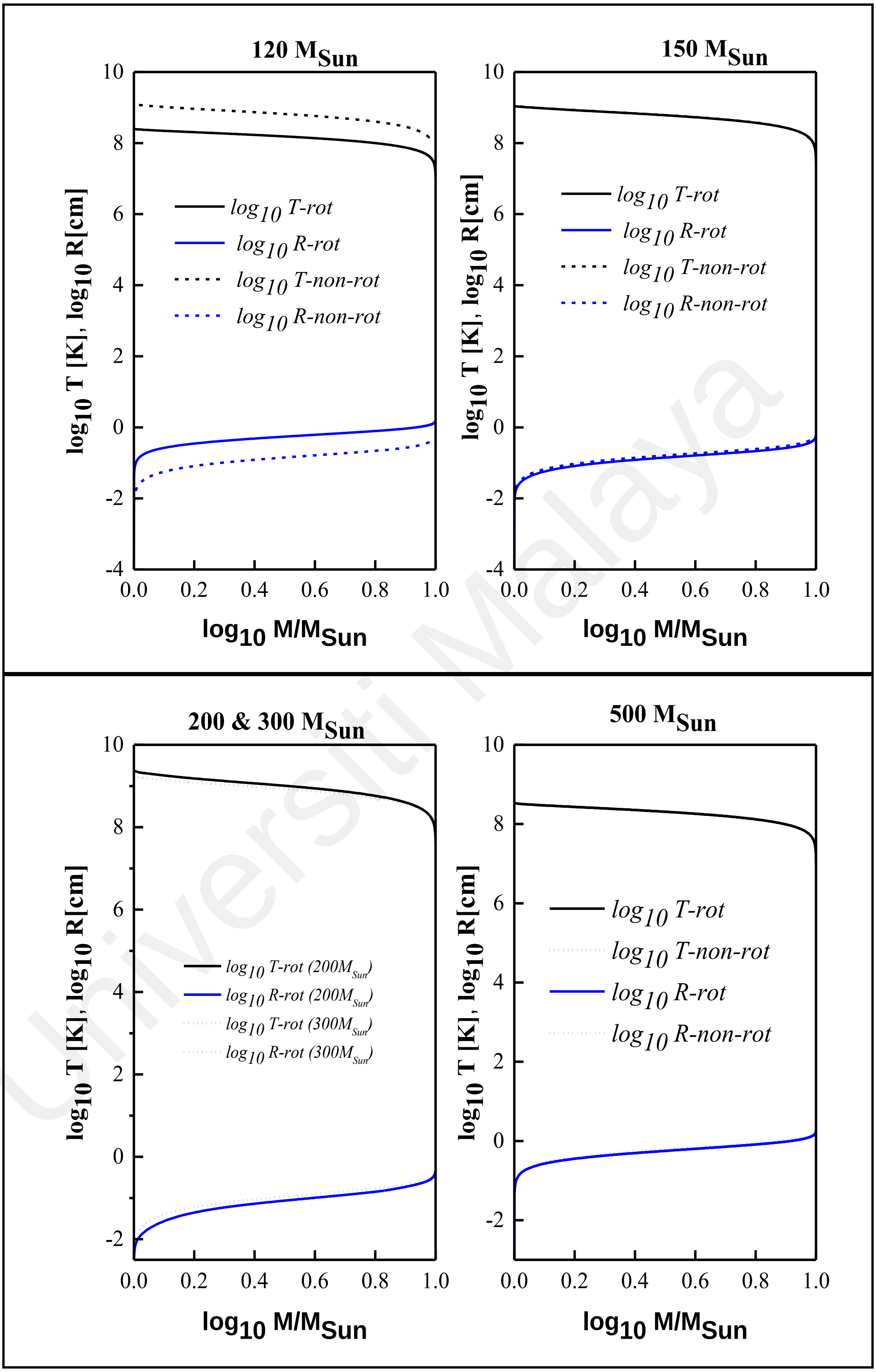

Figure 4.19: Normalised radius (cm) & temperature (K) of star against mass (M/ M⊙) for 120 M⊙ (upper-left), 150 M⊙ (upper-right) and 500 M⊙ (down-right), and 200 M⊙ (down-left) and 300 M⊙ (down-right).

In both rotating and non-rotating models, the dynamics of both temperature and radius profiles are similar in pattern for all models under consideration. In Figure 4.19, the temperature and radius of rotating model 120 M⊙ is higher than the non-rotating. And by implications of high radius in rotating model, the density of the rotating 120 M⊙ model at centre is higher than at the centre of the non-rotating model, and similarly the surface density of this particular model is lower in rotating model than in non-rotating. However, this might be due to recorded high temperature of the rotating model at centre which affect the chemical abundance and subsequently other properties of the star.

4.5 Profiles of electron density from evolution of 120, 150, 200, 300 and 500 M⊙ models

The emissivity and spectra of neutrinos are uniquely determined by temperature and electron density. However, neutrino flavors which are produced from processes of neutrinos are $\nu_e, \bar{\nu}_e, \nu_\mu, \bar{\nu}_\mu, \nu_\tau, \bar{\nu}_\tau$. And from standard theory of electroweak interactions, fluxes for these flavors are similar, but some differences exist between electron and muon/tau flavors. Due to significant contribution of the electron density (n_e) on total energy-loss, we must evaluate its values before we calculate the neutrino energy loss through oscillations. As explained in previous chapters, the existence of different values of electron density and density of matter in massive stars arises due to rotation effect on many quantities, such as mass loss, during the evolution process of massive stars. To examine this effect, we showed, in Figure 4.20, dynamics of electron density with respect to radius of the stars and make comparison with density of matter. The electron density is normalised to Avogadro constant (N_A), according to the relation given by: $n_e = \frac{\rho N_A}{\mu_e}$ where $\mu_e = \sum {A_i}/{X_i Z}$ is the mean molecular weight in unit of electron mass and $N_A = 6.023 \times 10^{23}\ mol^{-1}$ is Avogadro constant. Also, A_i is atomic weight of the atomic charge Z and X_i is its abundance by weight.

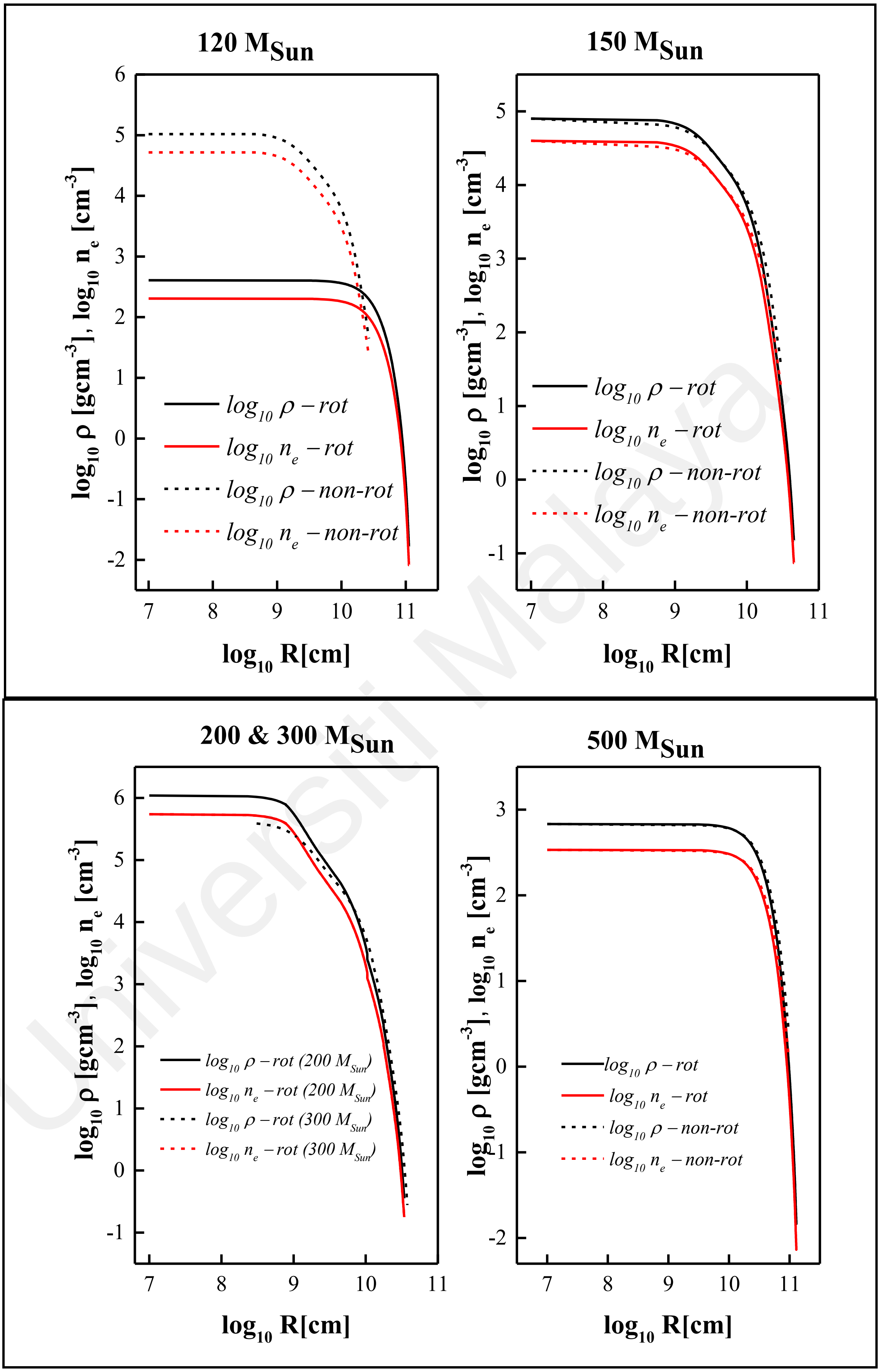

Figure 4.20: Graphs of density of matter ρ, electron density n_e (normalised to Avogadro constant, N_A) with respect to radius (cm) of star, for 120 & 150, 500 M⊙, and 200 & 300 M⊙.

We can see from Figure 4.20, that there are different values of both density of matter and electron density in both rotating and non-rotating model. For example, in 120 $M_\odot$ model, the rotation effect, which caused contraction of the stars, also shrink the values of the two densities of both matter and electrons. The non-rotating models recorded higher values of both density of matter and electron density. Similarly, in both rotating and non-rotating models, the density of matter is higher than electron density, this might not be unconnected with the fact that most electrons are annihilated. In 120 $M_\odot$, the values of density of matter and electron density for non-rotating models are greater than rotating model. The centrifugal force acting on the stars, during rotation, also influenced the densities of matter and electron density.

4.6 Thermal neutrino energy-loss from 120, 150, 200, 300 and 500 $M_\odot$ stellar models

The variations in the evolution track of these models is responsible for different and independent values of thermal neutrino energy, as we can see in Figures 4.21, 4.22, 4.23 and 4.24. In Figure 4.21 the energy-loss from neutrino thermal processes for non-rotating (up) and rotating (down) 120 $M_\odot$ model is shown. In non-rotating model, the total energy is similar to pair neutrino and has the highest value as compared to all other processes. While, plasma neutrino recorded lowest value of neutrino energy-loss. The other two processes (photo and bremsstrahlung) are relatively the same and have greater value than plasma neutrino. However, on the contrary, in rotating model, pair neutrino has lowest value of neutrino energy loss. While total, photo and bremsstrahlung are almost similar and possesses highest values. Plasma neutrino has medium value in the rotating 120 $M_\odot$ model. This shows a major contribution effect of rotation in the energy loss. For both non-rotating and rotating 150 $M_\odot$ model in Figure 4.22, the total and pair neutrino energy are similar and have the highest values compared to other three processes. Photo and bremsstrahlung processes are similar and greater than plasma process. This clearly indicate that the dominant process is pair neutrino.

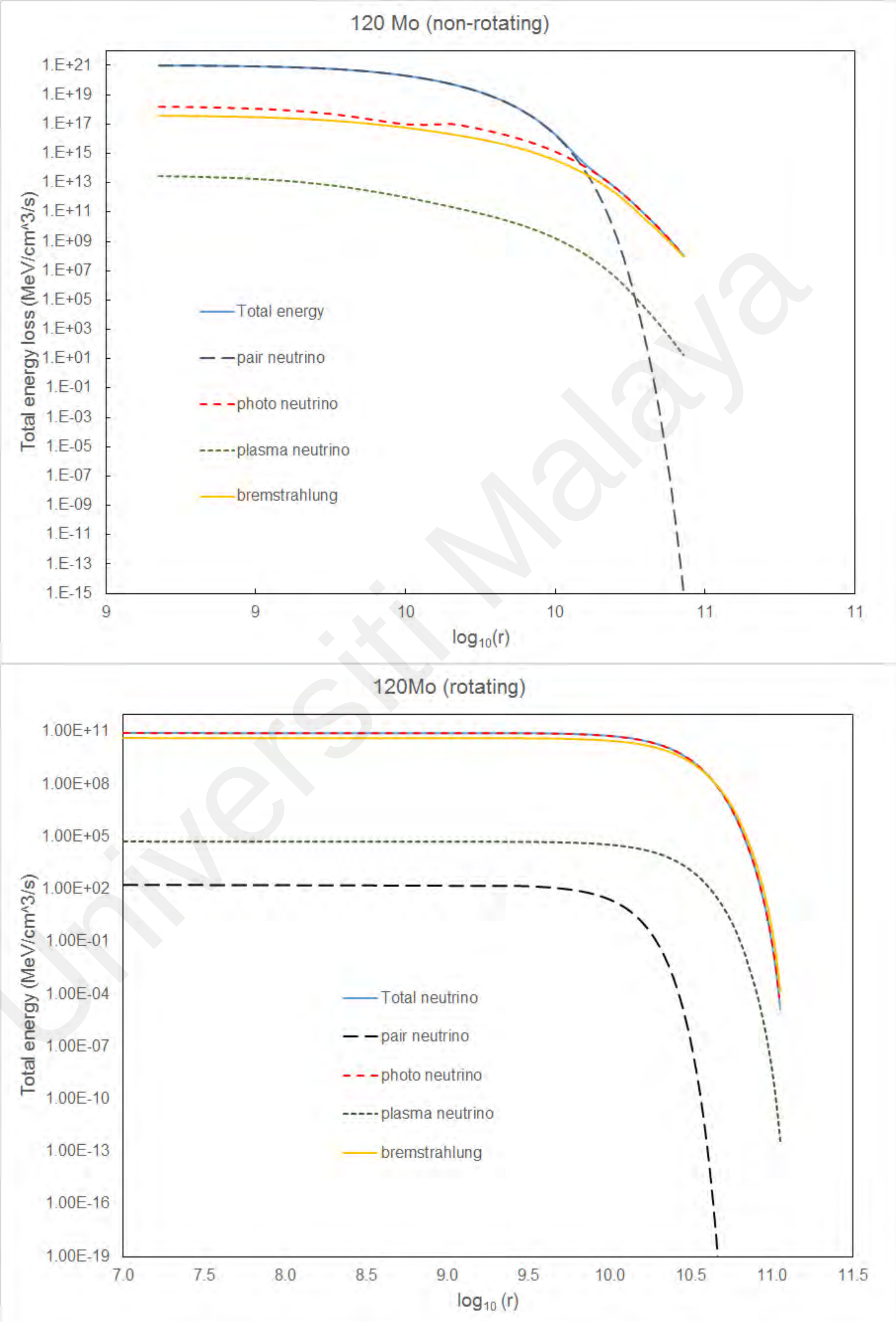

Figure 4.21: The Energy-Loss from neutrino thermal processes against radius (cm) of star for 120 M$_\odot$ non-rotating (up-graph) and rotating (down-graph) model.

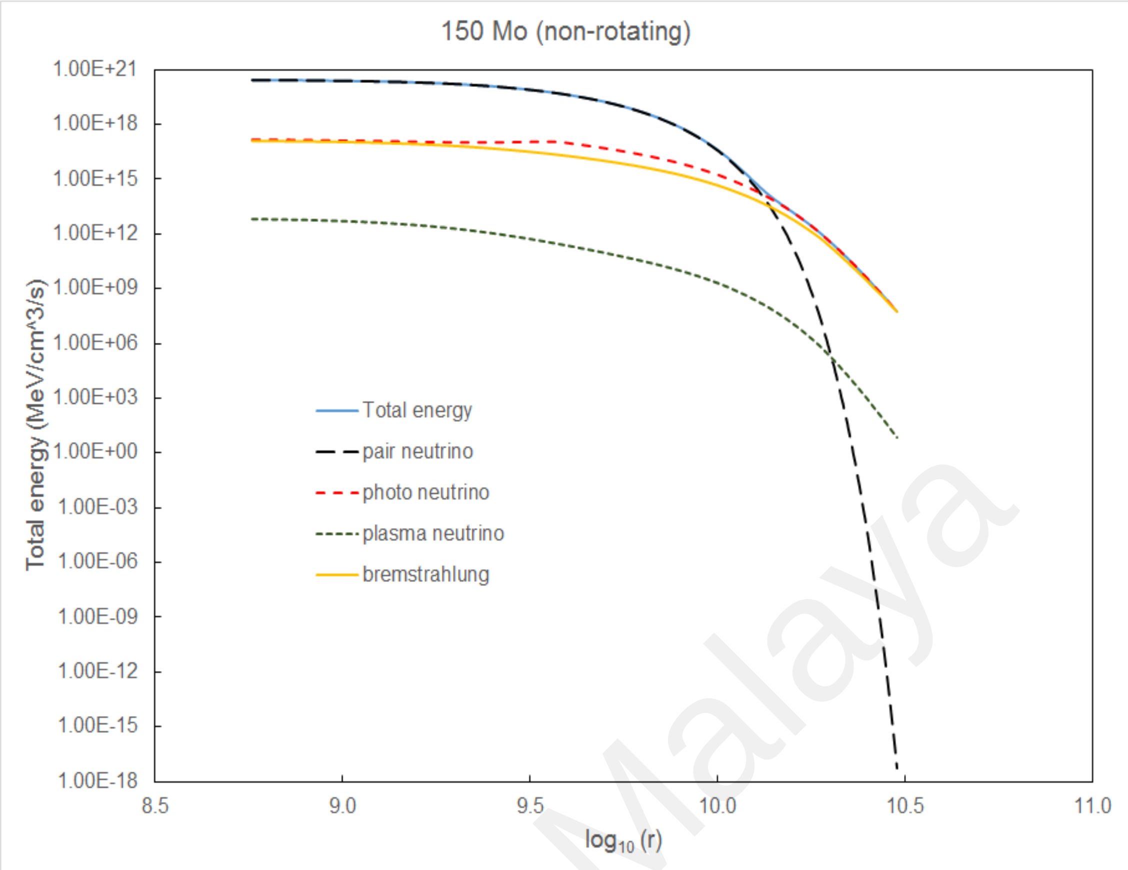

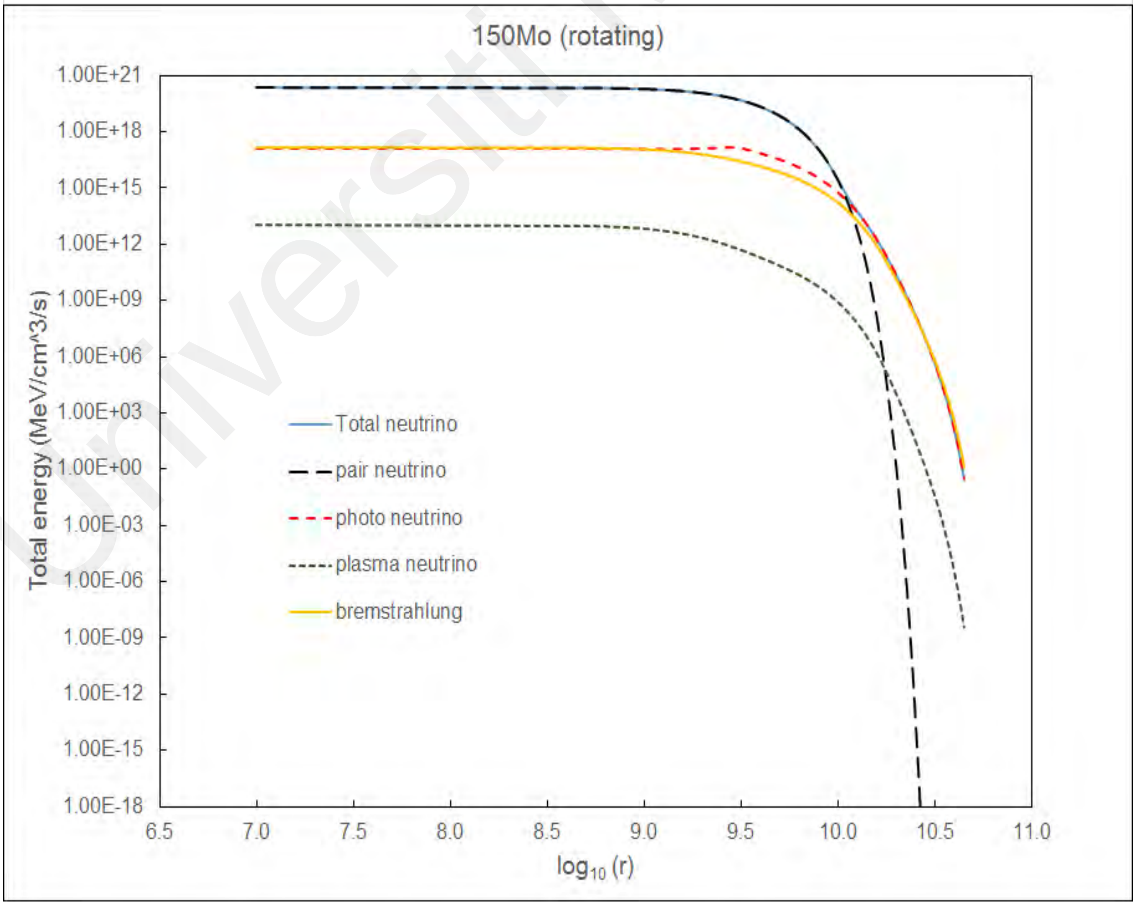

Figure 4.22: The Energy-Loss from neutrino thermal processes against radius (cm) of star for 120 M⊙ non-rotating (up-graph) and rotating (down-graph) model.

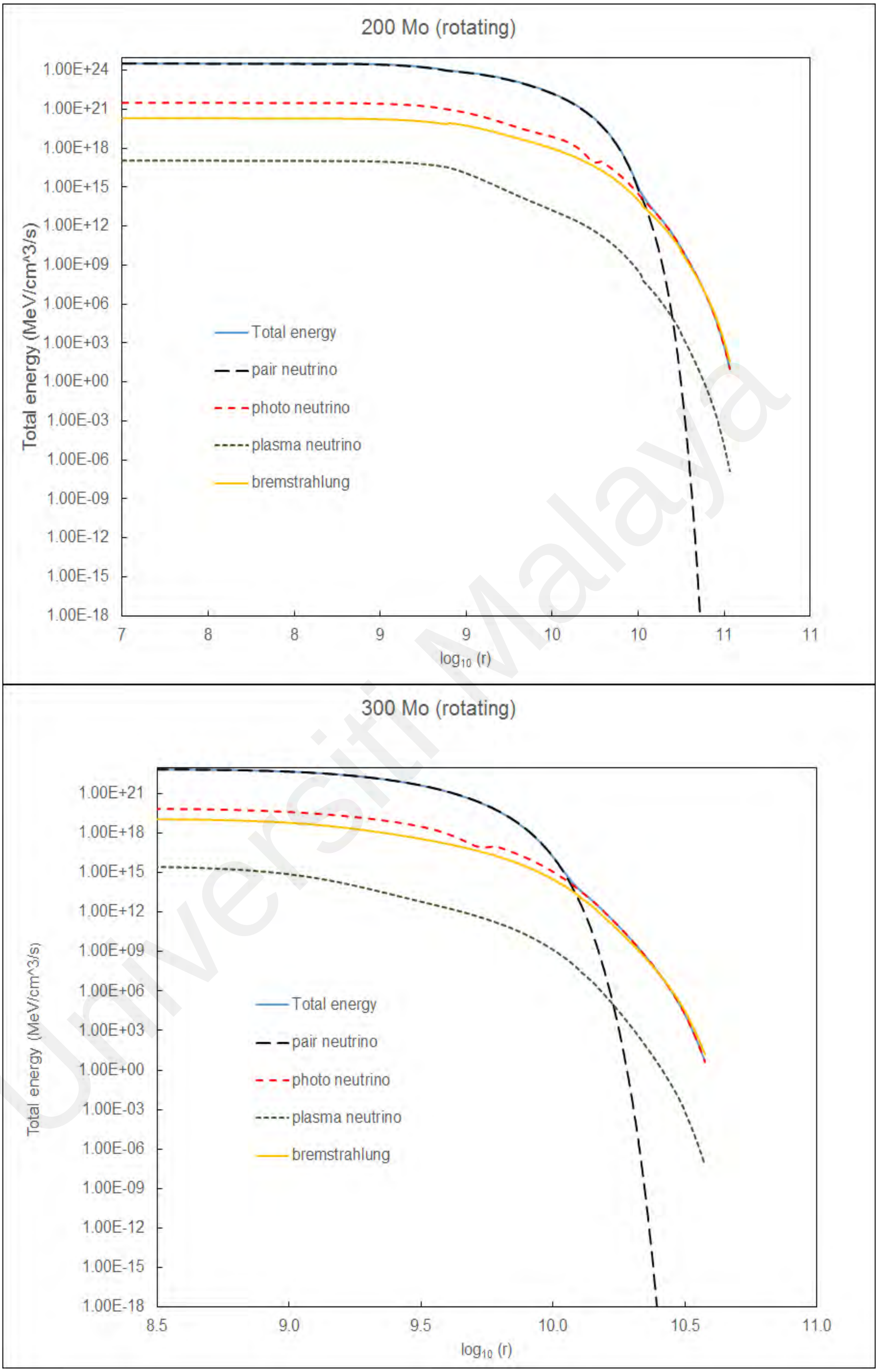

Figure 4.23: The Energy-Loss from neutrino thermal processes against radius (cm) of star for 200 M⊙ (up) and 300 M⊙ (down) rotating models.

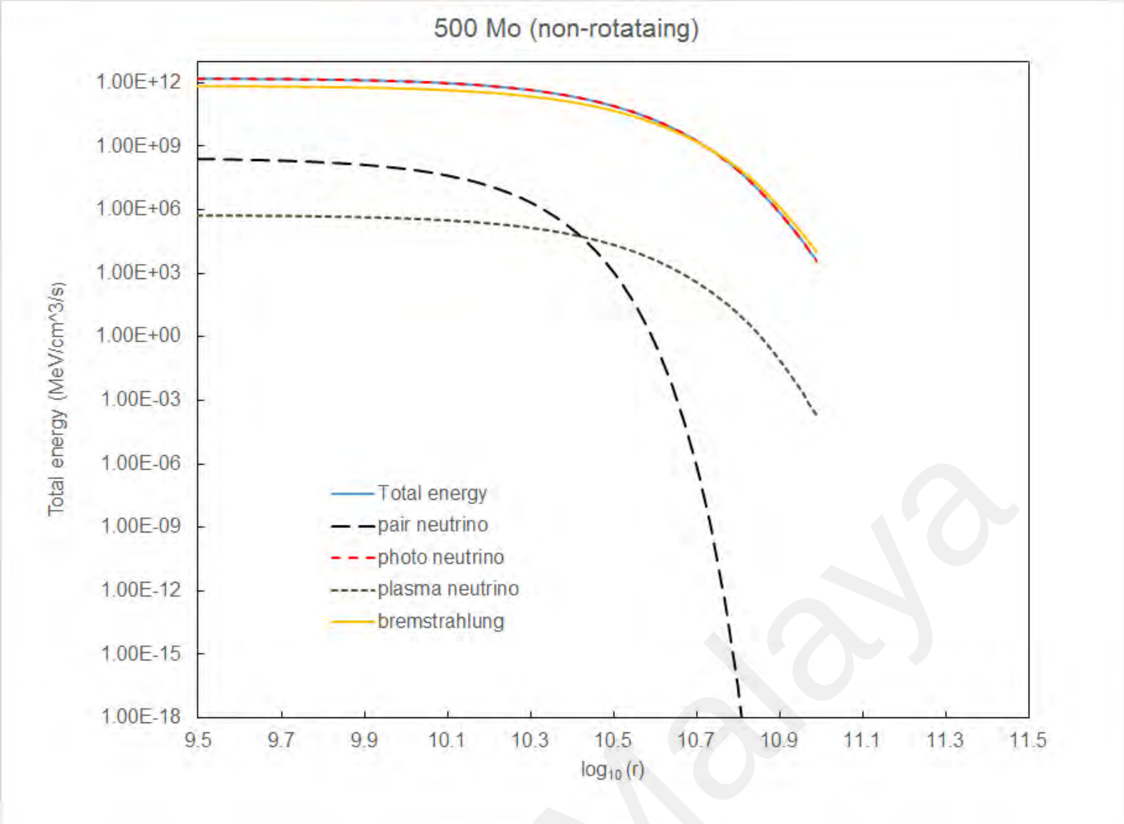

Figure 4.24: The Energy-Loss from neutrino thermal processes against radius (cm) of star for 500 M⊙ non-rotating model.

For both 200 M⊙ and 300 M⊙ rotating models, Figure 4.23 (up-graph & down-graph) respectively, the major contributor of neutrino energy loss is by pair neutrino and is similar to total neutrino energy loss. In these models, we see that plasma neutrino is the lowest thermal neutrino energy loss. Whereas, other processes of thermal neutrino, photo and bremsstrahlung neutrinos, are both less than pair neutrino and greater than plasma process, in both 200 M⊙ and 300 M⊙ rotating models. In Figure 4.24, which showed 500 M⊙ non-rotating model, photo neutrino and bremsstrahlung processes are the major contributors and are similar to total energy loss. The lowest energy loss is by pair neutrino and is greater than plasma neutrino. The plasma neutrino is averagely the lowest thermal neutrino process in this massive star.

On the other hand, since rotation minimizes the effective temperature, we could see that thermal neutrino processes involving lesser temperature range are higher in 120 M⊙ rotating model. The degree of rotation similarly shrink the amount of total neutrino energy loss. The pair neutrino is averagely the dominant process in all the models (except for 120 M⊙ rotating and 500 M⊙ non-rotating models), which is a clear manifestation of the effect of interaction with magnetic field especially for rotating models that also produced higher oxygen cores and more production of pairs that will later annihilate into neutrinos. The total energy loss as a function of radius varies due to contraction of the stars. We know that the stars are contracted more with increase in degrees of rotation, so also the total neutrino energy loss differ as contraction causes change in range of densities. For example, pair neutrino energy loss is dominant at relatively low density when the star contracts, but plasma process requires higher density when the star is free from any effect of contraction.

4.7 Chapter Summary

Generally, this chapter present results obtained from different models constructed into electron-positron equation state and SNEUT4 code. The first part of the chapter addresses objective one of the research. While second and third parts focusses on second and third objectives of this research respectively. We have presented full description of the results obtained. We also discussed effects of these results on end fates of very-massive stars with emphasis on PISN explosion. In the last part of this chapter, the thermal neutrino processes and the total neutrino energy-loss from 120, 150, 200, 300 and 500 M⊙ stellar models is presented.

CHAPTER 5: KINETICS OF NON-EQUILBRIUM PAIR PLASMAS

This chapter is devoted for future work which could be useful in understanding the pair-production processes involved in very-massive stars. A lot of work could be done to investigate the roles of these processes in the evolution and final fates of very-massive stars.

5.1 Introduction

There has been growing evidence for emission of high-energy radiation from many astrophysical objects. An annihilation lines has been observed from galactic centre (Leventhal et al., 1978). Several gamma ray bursts have 400-500keV feature which is probably an annihilation line (Mazets et al., 1982), and Cygnus X-1 may also show one (Nolan & Matteson, 1983). Jets from Active Galactic Nuclei (AGN) shows evidences of existence of relativistic plasmas of electron-positron pair in dense radiation fields of the AGN. These radiation from AGN possesses characteristics properties of non-thermal plasma, when the emitted power is uniform with respect to photon energy within the range of infrared to hard X-rays (Svensson, 1987). Pair production is also confirmed to be important in galactic black hole sources, if the primary radiation mechanism produces more than 1 per cent of an Eddington luminosity above 1 MeV (Guilbert et al., 1983). The annihilation of electrons and anti-electrons (the positron) pair into two photons and its reverse process- the production of positron-electron pair by interaction of two photons- were first studied in the frame work of quantum mechanics by P.A.M. Dirac and by G.Breit and J.A. Wheeler in 1930s respectively. At high temperature and relatively low density electron-positron pair production from cores of massive stars is crucial for evolution, collapse, death and end fates of not only massive stars but many Astrophysical objects, such as in mass-loss from black hole mergers (Belczynski et al., 2016) and in some models of the universe which predicted that first stars at Dark Ages might form massive stars and become subject to pair-instability (Abel et al., 1998; Abel et al., 2000; Bromm et al., 2002; Bromm & Larson, 2004; Chatzopoulos & Wheeler, 2012a). Pairs increase the cooling rates and opacity of the source object, they also affect the radiation transport since annihilation acts as a hard photon source and production as a photon sink. So, to interpret the observed hard spectra of active nuclei, gamma-ray busters and particularly end fates of very-massive stars, we need to understand details of pair production and radiative transfer in very hot plasmas. However, these relativistic pair plasmas which envisage of both thermodynamic equilibria and non-equilibria, have been both investigated thoroughly in literature.

Most of works on this focuses on thermal equilibrium, examples which can be found in Svensson (1982a), while Pilla and Shaham (1997) provides detail information on non-equilibrium case by addressing time evolution of non-equilibrium electron-positron pair plasmas by means of kinetic theory approach (Coppi, 1992; Fabian et al., 1986; Ghisellini, 1987; Svensson, 1987). This time evolution is determined by numerically solving Boltzmann equations of the non-equilibrium pair plasma which contain high-energy photons, and distribution functions of the particles and photons are discretised in energy and spatial coordinates (Pilla & Shaham, 1997). This approach is significantly important due to its good resultant photon statistics at higher energies. However, analysing the non-equilibrium pair plasmas has been having problems due to some computational difficulties, but this difficulty seems to be resolved with the work of Pilla and Shaham (1997), in which the Boltzmann equations are solved based on an adaptive Monte Carlo (MC) sampling scheme. This scheme is, however having two advantages over previous conventional MC methods (like Phase-Space Density PSD, and Large-Particle LP representations). Number one of such advantages is that it is faster than the conventional MC and, two it is more flexible than previously used numerical methods. Meanwhile, it could easily accept anisotropic distributions (Pilla & Shaham, 1997).

5.2 Processes of pair Plasma

The theoretical, experimental and observational evidences originating from pair producing and photon producing processes have extremely synthesized the correlation between Physics and astrophysics in recent years. These processes; initially introduced by Dirac, Breit and Wheeler as well as by Sauter etc., have been continually followed by efforts from experimental verifications on earth-based facilities. Dirac process has been by far most successful and Breit and Wheeler process despite been generally simple, as the reverse of Dirac process, but is one of experimentally toughest to be confirmed, whereas, vacuum process of polarization in strong electromagnetic field, which championed by Sauter et al. proposes the concept of critical electric field. The processes of electron-positron pair production and annihilation has been playing great role in the evolution and decaying of highly energetic astrophysical plasmas, such as supernovae, gamma-ray bursts and early universe (Wolf, 1974). However, the physical processes of heating and cooling mechanisms, thermal equilibrium and ionization equilibrium occurring in tenuous astrophysical plasmas are well understood (Svensson, 1982a). Observations of properties like gamma-ray emission from various object indicate that astrophysical plasma may achieve relativistic temperatures. At this relativistic temperature, a number of threshold processes appear associated with creation of electron-positron pairs. The electron-positron pairs are produced through photo-photon, photon-particle and particle-particle interactions. The created pairs either annihilate into photons or participate in other photon and pair producing process. The Quantum Electrodynamical processes occurring in relativistic plasma are listed in table below. The photon and pair generating processes treated here are pair annihilation and pair production processes, which are very relevant microscopic processes in a pair plasma. Adopting the model developed by (Pilla & Shaham, 1997), for a stationary, neutral un-magnetised pair plasma of protons(P), electrons(e^-), Positrons (e^+) and Photons (γ) with densities

$N, n_-, n_+ \ and \ n_\gamma$ respectively. n_γ Represents the density of Photons with energy$\epsilon(in\ mc^2)$. In the following subsections, we will presents the physical quantities of the kinetic equations of this processes.

5.2.1 Electron-Positron Pair Annihilation

The existence of positive and negative energy states in theoretical account of relativistic quantum theory was predicted by Dirac. The electron was considered under the concurrent influence of two incident beams of radiation which induce modulation of electron to the state of negative energy. This self-generated process occur independently of the energy for any pair of electron and positron. Meanwhile, this procedure may not need an existing radiation before it take place. The process of an electron-positron pair annihilation into two photons is given in a reaction equation as

$$e^+ + e^- \rightarrow \gamma + \gamma \tag{5.1}$$

And there are two Feynman diagrams for this process, as can be shown in the figure below;

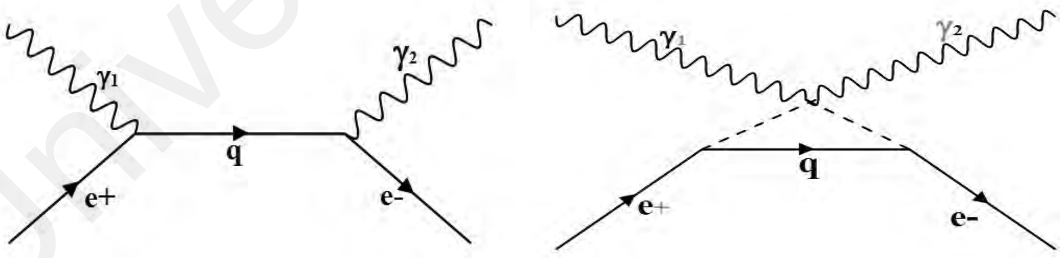

Figure 5.1: Feynman diagram for electron-positron pair annihilation.

The annihilation of an electron with four-momentum P_- and spin S_- and a positron with four-momentum P_+ and spin S_+ into two photons with four-momenta and polarisations K_1 and K_2 could have a transition amplitude for the accelerated transition process given by;

$$M_{e^+ + e^- \rightarrow \gamma + \gamma} = \frac{16e^2|a_1|^2|a_2|^2}{|\varepsilon'|m_e c} K_{1,2} \frac{1-\cos\left(\delta\varepsilon'/\hbar\right)}{(\delta\varepsilon')^2} \tag{5.2}$$

Where $\epsilon' = m_e c^2 - \nu_1 - \nu_2$ and ν_1, ν_2 are the photon frequencies.

$$K_{1,2} = -(m_1.m_2)^2 + \frac{1}{4}[1 - (m_1.m_2)(n_1.n_2) + (m_1.n_2)(m_1.n_2)]\frac{\nu_1+\nu_2}{m_e c^2} \quad (5.3)$$

is a dimensionless number which depend on the unit vectors in the directions of the two photons polarization vectors m_1 and m_2. n_1& n_2 are respectively defined by $n_{1,2} = I_{1,2}m_{1,2}$. And the intensities of the photons is $I_{1,2} = \frac{{\nu_{1,2}}^2}{2\pi c}\left|K_{1,2}\right|^2$.

Table 5.1: Quantum electro dynamical processes in pair plasmas.

Basic two body Interactions	**Radiative Variant**	**Pair Production Variant**
Moller and Bhaba Scattering $ee \to ee$	Bremsstrahlung $ee \leftrightarrow ee\gamma$	$ee \leftrightarrow eee^+e^-$
Compton Scattering $\gamma e \to \gamma e$	Double Compton scattering $\gamma e \leftrightarrow \gamma e\gamma$	$\gamma e \leftrightarrow ee^+e^-$
Pair annihilation $e^+e^- \to \gamma\gamma$	Three Quantum annihilation $e^+e^- \leftrightarrow \gamma\gamma\gamma$	*Not available*
Photon-photon Pair production $\gamma\gamma \to e^+e^-$	Radiative pair production $\gamma\gamma \leftrightarrow e^+e^-\gamma$	*Not available*
Processes Involving Protons		
Coulomb scattering $ep \to ep$	Bremsstrahlung $ep \leftrightarrow ep\gamma$	$ep \leftrightarrow epe^+e^-$ $\gamma p \leftrightarrow pe^+e^-$

5.2.2 Electron-Positron Pair Production

The electron-positron pair production is an important cooling mechanism for plasmas at relativistic temperature. The pair production in the interaction of two photons was given by Breit-Wheeler, which according to Dirac's theory of electron, is influenced by a transition of an electron from negative energy state to a positive energy state under the influence of two light quanta on a vacuum. In contrary to Dirac's process, the pair production of electron-positron has a threshold because of its non-zero mass nature. This implies that ample amount of energy is required to create electron-positron pair at centre of mass of the system, the energy must be twice greater than the electron mass energy. The reaction equation can be written as

$$\gamma + \gamma \to e^+ + e^- \tag{5.4}$$

And the two Feynman diagrams for the two photon pair production as depicted in the figure below:

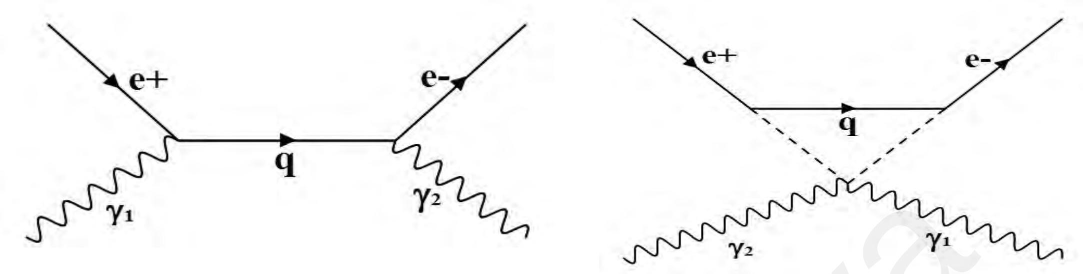

Figure 5.2: Feynman diagram for electron-positron pair production.

The transition amplitude of this important process is given by;

$$M_{\gamma+\gamma\to e^+ + e^-} = \left(\frac{\alpha\hbar}{m_e c}\right)^2 2|a_1|^2|a_2|^2 K_{1,2} \frac{\left|1-\cos\left({\delta\epsilon'}/{\hbar}\right)\right|^2}{(\delta\epsilon')^2} \tag{5.5}$$

where $K_{1,2}$ is the dimensionless number obtained by Dirac. The squared amplitudes $|a_1|^2$ and $|a_2|^2$ are determined by intensities $I_{1,2}$ of the two photons as

$$\left|a_{1,2}\right|^2 = \frac{2\pi c}{{\omega_{1,2}}^2} I_{1,2} \tag{5.6}$$

$\delta\varepsilon$ is energy difference between initial light states and final electron-positron states.

$$\epsilon_1 = -c\left({P_1}^2 + {m_e}^2 c^2\right)^{\frac{1}{2}} \tag{5.7}$$

$$\epsilon_2 = -c\left({P_2}^2 + {m_e}^2 c^2\right)^{\frac{1}{2}} \tag{5.8}$$

where P_1, P_2 are the four-momentum of the positron and electron respectively. Therefore,

$$d(\delta\epsilon) = c\left({P_2}^2 + {m_e}^2 c^2\right)^{\frac{1}{2}} + \epsilon_1 - \hbar\omega_1 - \hbar\omega_2 \tag{5.9}$$

where $P_2 = -P_1 + K_1 + K_2$ the final momentum of the electron. Thus, from the energy and momentum conservations, we get;

$$d(\delta\epsilon) = c^2 \left[\frac{|P_1|}{\epsilon_1} - \frac{P_1 P_2}{(|P_1|\epsilon_2)}\right] dP_1 \tag{5.10}$$

The effective collision area (cross section area) for the head-on collision of two light quanta was shown by Bret-Wheeler to be

$$\sigma_{\gamma\gamma} = 2\left(\frac{\alpha\hbar}{m_e c}\right)^2 \int \frac{c|P_1|^2}{\hbar\omega_1 \hbar\omega_2} K_{1,2} \left[\frac{|P_1|}{\epsilon_1} - \frac{P_1 P_2}{(|P_1|\epsilon_2)}\right]^{-1} d\Omega_1 \tag{5.11}$$

where Ω_1 is the solid angle matching the total energy conservation $\delta\epsilon = 0$. In the centre-of-mass of the system, the momenta of the electron and the positron are equal and opposite $P_1 = -P_2$ also the momenta of the photons are $K_1 = -K_2$. Corollary, the energies of the electron and the positron are equal: $\epsilon_1 = \epsilon_2 = \epsilon$ and so, the energies of the photons: $\hbar\omega_1 = \hbar\omega_2 = \epsilon_\gamma = \epsilon$.

5.2.3 Compton Scattering

This process involves an incoming photon absorption by an electron with four-momentum and polarisation vector. The Feynman diagram of this process can be shown in the figure below:

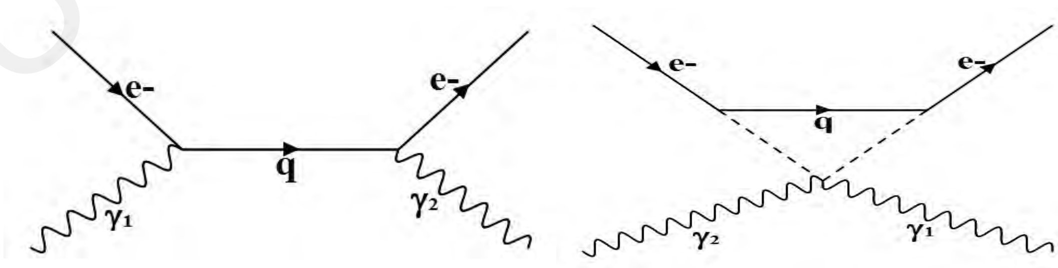

Figure 5.3: Feynman diagram for Compton scattering.

5.3 Kinetic theory equations

In general description of kinetic theory approach, energy can be added or subtracted by means of absorption and/or emission of the ray passing through matter and will therefore change the specific intensity of the ray. Meanwhile, photons scattered into or out of the beam may also cause effects on the intensity. In the next sub-sections, we generally defined the physical quantities due to any form of radiation transfer.

5.3.1 Emission coefficient

The emission coefficient j is the energy emitted per unit time per unit solid angle per unit volume $j = \frac{dE}{dtdVd\Omega}$, While the monochromatic emission coefficient can be given as;

$$j_v = \frac{dE}{dtdVd\Omega dv} \tag{5.12}$$

Therefore the coefficient of emission is dependent on the direction of the emission. In the case of anisotropic emitter, for which most astrophysical object are, when randomly distributed, then

$$j_v = \frac{1}{4\pi} P_v \tag{5.13}$$

P_v is the radiation power per unit volume per unit frequency. If the spontaneous emission is defined by the (angle integrated) emissivity ϵ_v, which is defined as emitted energy per unit frequency per unit time per unit mass, then the isotropic emission is

$$dE = \epsilon_v \rho dV dt dv \frac{d\Omega}{4\pi} \tag{5.14}$$

ρ is the mass density of the emitting medium and the last factor takes into account the fraction of energy radiation into $d\Omega$. Hence, the relation between ϵ_v and j_v for isotropic emission, is $j_v = \frac{\epsilon_v \rho}{4\pi}$.

This shows that the beam propagation in distance ds and cross sectional area dA through a volume$dV = dAds$, has an additional intensity to the beam by spontaneous emission given as;

$$dI_v = j_v ds \tag{5.15}$$

5.3.2 Absorption Coefficient

When a beam as it travels a distance ds, the loss of intensity is given by;

$$a_v = \frac{-dI_v}{I_v ds} \tag{5.16}$$

The absorption coefficient $a_v(cm^{-1})$ is positive when energy is taken out of the beam. In a microscopic model, particles with density n each present an effective absorbing area, or cross section, of magnitude$\sigma_v(cm^2)$. These absorbers are may be randomly distributed. Now, considering the effect of these absorbers on radiation through dA within solid angle $d\Omega$, the elemental number of absorbers equals $ndAds$. The total absorbing area presented by absorbers equals to $n\sigma_v dAds$. And the absorbed energy out of the beam is;

$$-dI_v dAd\Omega \mathrm{dtdV} = I_v(n\sigma_v dAds)d\Omega \mathrm{dtdV} \tag{5.17}$$

And hence,

$$dI_v = -n\sigma_v I_v ds \tag{5.18}$$

which is the above phenomenological law, where $a_v = n\sigma_v$ or $a_v = \rho O_v$. Where $O_v(cm^2 g^{-1})$ is the mass absorption coefficient or the opacity. However, the paramount conditions of validity for this microscopic picture are;

I. The linear scale of the cross section must be small in comparison to the inter-particle distance

II. The absorbers are independent and randomly distributed.

Fortunately, these conditions are always met for Astrophysical problems.

5.3.3 Radiative transfer equation

Incorporating the two equations above, that is the effect of absorption and emission into one single equation, we have $\frac{dI_\nu}{ds} = j_\nu = -a_\nu I_\nu$

$$\Rightarrow \frac{dI_\nu}{ds} = j_\nu - a_\nu I_\nu \tag{5.19}$$

This provides a useful way for solving the intensity in an emitting and absorbing medium. In the case of emission only, $\alpha_\nu = 0$ the above equation has solution given by;

$$I_\nu(s) = I_\nu(s_0) + \int_{s_0}^{s} j_\nu(s')ds' \tag{5.20}$$

Which shows that the increase in brightness is equal to the emission coefficient integrated along the line of sight. However, for absorption only, $j_\nu = 0$;

$$I_\nu(s) = I_\nu(s_0)e^{\left(-\int_{s_0}^{s} a_\nu(s')ds'\right)} \tag{5.21}$$

And the brightness decrease on the ray by absorption coefficient exponential integrated along the line of sight.

5.3.4 Optical depth

The optical depth is defined by $d\tau_\nu = a_\nu ds$

$$\Rightarrow \tau_\nu(s) = \int_{s_0}^{s} a_\nu(s')ds' \tag{5.22}$$

This optical depth is measured along the path of a traveling ray, occasionally, τ_ν can be measured backward along the ray and a minus sign appear. In the above equation, the point s_0 is arbitrary, which set the zero point for the optical depth scale. Optically thick medium or opaque is when τ_ν, integrated along a typical path through the medium, satisfies $\tau_\nu > 1$. On the other hand, when $\tau_\nu < 1$, the medium is said to be optically thin or transparent. Essentially, an optically thin medium is one in which the typical photon of frequency ν can traverse the medium without being absorbed, whereas, an optically thick medium is one in which the average photon of frequency ν cannot traverse the entire medium without being absorbed.

5.3.5 Mean free path

This is the average distance a photon can travel through an absorbing material without being absorbed. It is sometimes related to the absorption coefficient of a homogeneous material. From the exponential absorption law, the probability of a photon travelling at least an optical depth τ_ν, is simply $e^{-\tau_\nu}$. The mean optical depth travelled is equal to unity.

$$\langle \tau_\nu \rangle = \int_0^\infty \tau_\nu e^{-\tau_\nu} d\tau_\nu = 1 \tag{5.23}$$

The mean physical distance travelled in a homogeneous medium is defined as the mean free path l_ν and is determine by $\langle \tau_\nu \rangle = a_\nu l_\nu = 1$;

$$\Rightarrow l_\nu = \frac{1}{a_\nu} = \frac{1}{n a_\nu} \tag{5.24}$$

Therefore, the mean free path l_ν is the reciprocal of the absorption coefficient for homogeneous material.

5.3.6 Radiation force

When a medium absorbs radiation, then the radiation must have exerted a force on the medium since radiation carries momentum. The radiation flux vector is $F_\nu = \int I_\nu \boldsymbol{n} d\Omega$. Where n is a unit vector along the direction of the ray. Since photon has momentum $\frac{E}{c}$, the vector momentum per unit area per unit time per unit length absorbed by the medium is $f = \frac{1}{c}\int a_\nu F_\nu dV$. Where$dV = dAds$, f is the force per unit volume imparted onto the medium by the radiation field. Hence, the force per unit mass of the material is given by

$$F = \frac{f}{\rho} = \frac{1}{c}\int O_\nu F_\nu dV \tag{5.25}$$

These two equations are based on the assumptions that; the absorption coefficient is isotropic and no momentum is imparted by the emission of the radiation as is true for isotropic emission.

5.4 General Kinetic equations of Plasma

In an un-magnetized, non-equilibrium, neutral and stationary pair plasma, which has number densities of photons, electrons and positrons given by: $n_\gamma, n_-, and\, n_+$ respectively, and assuming homogeneous and isotropic plasma, the distribution functions is energy and time dependant. the equilibrium spectral functions for photons, which are independent of time given by Pilla and Shaham (1997) is;

$$F_\gamma(\epsilon) = \frac{1}{2\xi(3)\vartheta^3}\frac{\epsilon^2}{exp(\epsilon/\vartheta)-1} \tag{5.26}$$

This equation resulted from Planck function for photons, and ξ is Riemann zeta function. However, an equilibrium density of photons given by the expression is used;

$$n_\gamma = 16\pi\xi(3)\left(\frac{mc}{h}\vartheta\right)^3 \tag{5.27}$$

Assuming that electrons and positrons have equal spectral functions, the relativistic electron Maxwell-Boltzmann distribution can be given by;

$$F_e(\gamma) = \frac{1}{\vartheta K_2(1/\vartheta)}\beta\gamma^2 exp\left(-\gamma/\vartheta\right) \tag{5.28}$$

In this equation K_2 is modified Bessel function of second kind of order 2, and $\beta = \frac{\sqrt{(\gamma^2-1)}}{\gamma}$ is velocity in unit of c, ε is the photon energy. The dimensionless temperature of the plasma is defined by $\vartheta = k_B T/mc^2$. Where T is the temperature and k_B is Boltzmann constant. The plasma charge neutrality condition is $n_- = N + n_+$. Similarly, m and c are electron rest mass and speed of light respectively. While h is Planck's' constant. The photons could be studied from radiative transfer equation, while the pairs proceeds from relativistic Boltzmann equations. However, due to homogeneity and isotropy of the plasma, the Boltzmann equation will turn to simple rate equations in co-moving frame and can be expressed as;

$$\frac{\partial f_j}{\partial t} = \sum_x \left(\eta_j - f_j \chi_j\right)_x \tag{5.29}$$

where *t* is coordinate for the co-moving time and *j* represents either photons or electrons and x is the collision process (which could be pair process, bremsstrahlung, Compton scattering or coulomb collisions). η_j is the emission coefficients for production of particle j and χ_j is the corresponding absorption coefficient. These three parameters; f_j, η_j *and* $\chi_j$are energy and time dependant. Binary reaction rates in relativistic plasma is required in order to find the collision kernels; emissivity (η_j) and absorption χ_j of the collision process. However, after several physical and mathematical assumptions, the emission coefficient for electrons or photons, which has been used previously by many authors, can be expressed as;

$$\eta(\epsilon) = \int \prod_{i=1}^{2} [d\epsilon_i F_i(\epsilon_i)] R(\epsilon_1, \epsilon_2) P(\epsilon_1, \epsilon_2; \epsilon) \tag{5.30}$$

Where $R(\epsilon_1, \epsilon_2)$ is total reaction rate between two particles of energies ϵ_1 *and* ϵ_2 and P is probability which is integrated over all incident and emergent angles of the particles.

Meanwhile, the absorption coefficient of particles $i\ and\ j$ can be expressed in terms of spectral functions, given by;

$$\chi_i(\epsilon_i) = \frac{cn_j}{4\pi(1+\delta_{ij})} \int d\epsilon_j d\Omega_j F_j(\epsilon_j) g_{ij} \sigma_{total} \tag{5.31}$$

where σ_{total} is total scattering cross section for the process under consideration, g_{ij} is kinetic factor for a binary collision. From this equation, the region of integration is determined by energy momentum conservation. The above method of writing emission and absorption coefficients can be conveniently used in Monte Carlo evaluations (Pilla & Shaham, 1997).

5.5 Photon Collision Integrals

In this section, the integral expressions for emission, absorption and cross section coefficients of photons due to pair plasma processes is presented.

5.5.1 Photons emissivity due to pair annihilation:

The emission of photons arising from relativistic electron-positron pair annihilation has been studied by many authors(Pilla & Shaham, 1997). This has been explicitly derived by Svensson (1982b) and the final result, as presented by Pilla and Shaham (1997), can be expressed as;

$$\eta(\epsilon) = \frac{cn_+n_-}{4\pi\epsilon^2} \int d\mu d\phi \prod_{i=1}^{2} [F_e(\gamma_i) d\gamma_i] \frac{\beta_{cm}\gamma_{cm}}{\beta_c\gamma_c\gamma_1\gamma_2} \left(\frac{d\phi}{d\Omega}\right)_{cm} \tag{5.32}$$

the domain of this integration is under the $\gamma_{min} \leq \gamma_{1,2} \leq \gamma_{max}$, $-1 \leq \mu \leq 1$ and $0 \leq \phi \leq 2\pi$ which is subject to condition $-1 \leq z \leq 1$.

5.5.2 Photons cross sections due to pair annihilation:

The differential cross section in the centre of mass frame can be expressed by;

$$\left(\frac{d\phi}{d\Omega}\right)_{cm} = \frac{r_e^2}{4\beta_{cm}\gamma_{cm}^2}\left[\frac{3-\beta_{cm}{}^4}{2}(\xi_+ + \xi_-) - \frac{1}{2\gamma_{cm}^4}(\xi_+^2 + \xi_-^2) - 1\right] \quad (5.33)$$

where $\xi_\pm = 1/(1 \pm \beta_{cm}x)$ and $= yz + \sqrt{(1-y^2)(1-z^2)\cos\phi}$.

5.5.3 Photons absorption coefficient due to pair creation

When an electron-positron pair is created (or produced), the electron Lorentz factor in the centre-of-mass frame becomes $\gamma_{cm} = \sqrt{[(1-\mu)\epsilon\epsilon'/2]}$ where μ is the cosine of the angle between the two vectors. The absorption coefficient of the pairs can be expressed in form of spectral function as follows;

$$\chi(\epsilon) = \frac{cn_\gamma}{4}\int d\mu d\epsilon' F_\gamma(\epsilon')\sigma_{total}(\gamma_{cm})(1-\mu) \quad (5.34)$$

The domain of this integration is $-1 \le \mu \le 1$ and $\epsilon^* \le \epsilon' \le \epsilon_{max}$ such that ϵ^* is defined as the pair production threshold energy $\epsilon^* = 2/[(1-\mu)\epsilon]$, and ϵ_{max} is the plasma maximum photon energy.

5.5.4 Photons cross section due to pair creation

The photon scattering cross section due to pair creation can be found by integrating that of pair annihilation. This is related as $\sigma(\gamma\gamma \to ee) = 2\beta_{cm}^2\sigma(ee \to \gamma\gamma)$. And therefore the total photon cross section due to pair production can be expressed by;

$$\sigma_{total}(\gamma_{cm}) = \frac{\pi r_e^2\beta_{cm}}{\gamma_{cm}^2}\left[\frac{(3-\beta_{cm}{}^4)}{\beta_{cm}} ln\left(\frac{1+\beta_{cm}}{1-\beta_{cm}}\right) - 2\left(1 - \frac{1}{\gamma_{cm}^2}\right)\right] \quad (5.35)$$

5.5.5 Photons emission, absorption and cross section coefficients due to Compton scattering

The integral expressions for photons emissivity, absorption and cross section arising from comptonization are respectively presented as follows;

$$\eta(\epsilon) = \frac{c(n_+ + n_-)r^2{}_e}{8\pi\epsilon^2}\int F_\gamma(\tilde{\epsilon}_1)F_e(\gamma)\left(\frac{\Delta}{2\gamma^2 a\xi}\right)(d\gamma d\mu d\mu' d\phi) \quad (5.36)$$

$$\chi(\epsilon) = \frac{c(n_+ + n_-)}{2}\int F_e(\gamma)(1-\beta\mu)\sigma_{total}(x)d\mu d\gamma \quad (5.37)$$

And the total cross section can be expressed as;

$$\sigma_{total}(x) = 2\pi {r_e}^2\left[\frac{1+x}{x^3}\left(\frac{2x(1+x)}{1+2x} - ln(1+2x)\right) + \frac{ln(1+2x)}{2x} - \frac{1+3x}{(1+2x)^2}\right] \quad (5.38)$$

In both equations, the domain of integration is between$\gamma_{min} \le \gamma \le \gamma_{max}$, $0 \le \phi \le 2\pi$ and $-1 \le \mu \le 1$. where $\Delta = \xi^2 - \xi sin^2\theta' + 1$, θ' is the scattering angle of photons in the rest frame of incident electron, such that $\xi = {}^{a_1\gamma}/_{(a_1\gamma - b\epsilon)}$, while classical radius of the electron is ${r_e}^2$. The γ_{min} and γ_{max} denote the electron/positron limiting energies in the plasma.

5.5.6 Photons emission coefficients due to Bremsstrahlung

For pair-proton bremsstrahlung, assuming that the protons are at rest, can be given as;

$$\eta_{proton}(\epsilon) = \frac{cn_p(n_+ + n_-)}{4\pi\epsilon^2}\int_{1+\epsilon}^{\gamma_{max}} d\gamma F_e(\gamma)\beta\left(\frac{d\sigma}{d\epsilon}\right)_{proton} \quad (5.39)$$

5.6 Pairs Collision Integrals

Collision integrals of pairs can be determined in same way as for the photons collision integrals. In the following sub-sections, integrals for emission, absorption and cross sections coefficients of pairs due to the pair processes is presented.

5.6.1 Pair emissivity due to pair production

Adopting similar analogous to that for the pair annihilation emissivity presented in section 5.3.3.1, the pair creation emissivity due to electron-positron pair production can be expressed as;

$$\eta(\gamma) = \frac{cn_\gamma^2}{16\pi\beta\gamma^2} \int d\mu d\phi \prod_{i=1}^{2} \left[F_\gamma(\epsilon_i) d\epsilon_i\right] \frac{1-\mu}{\Delta} \left(\frac{d\sigma}{d\Omega}\right)_{cm} \tag{5.40}$$

where $\Delta = \beta_c \beta_{cm} \gamma_c \gamma_{cm}$.

5.6.2 Pair cross section due to pair creation

The differential cross section of the electron-positron pairs due to pair creation can be determined by multiplying equation (5.33) by β_{cm}^2. This can be expressed as;

$$\left(\frac{d\phi}{d\Omega}\right)_{cm} = \frac{r_e^2}{4\beta_{cm}\gamma_{cm}^2} \left[\frac{3-{\beta_{cm}}^4}{2}(\xi_+ + \xi_-) - \frac{1}{2\gamma_{cm}^4}(\xi_+^2 + \xi_-^2) - 1\right] \times \beta_{cm}^2 \tag{5.41}$$

The domain of integration remain same with the previous one.

5.6.3 Pair cross section due to pair annihilation

The pair cross section due to pair annihilation is related to the photon cross section due to pair creation by $\sigma(\gamma\gamma \to ee) = 2\beta_{cm}^2 \sigma(ee \to \gamma\gamma)$ (Pilla & Shaham, 1997), Therefore total pair cross section due pair annihilation can be given by dividing the photon cross section due to pair creation with $2\beta_{cm}^2$. This can be expressed as;

$$\sigma_{total}(\gamma_{cm}) = \frac{\pi r_e^2 \beta_{cm}}{\gamma_{cm}^2} \left[\frac{(3-{\beta_{cm}}^4)}{\beta_{cm}} ln\left(\frac{1+\beta}{1-\beta}\right) - 2\left(1 - \frac{1}{\gamma_{cm}^2}\right)\right] \times \frac{1}{2\beta_{cm}^2} \tag{5.42}$$

5.6.4 Pair absorption coefficient due to pair creation

The absorption coefficient due to pair creation can be found by considering an electron momentum $p' = \gamma(1, \beta)$ which annihilate with a positron of momentum$p' = \gamma(1, \beta')$. In the centre-of-mass frame, their Lorentz factor is given by; $\gamma_{cm} = \sqrt{[\gamma\gamma'(1 - \beta\beta'\mu)/2]}$. Therefore, the absorption coefficient is expressed as;

$$\chi_{\pm}(\gamma) = \frac{cn_{\mp}}{2} \int d\gamma' d\mu F_e(\gamma') \frac{\beta_{cm}\gamma_{cm}^2}{\gamma\gamma'} \sigma_{total}(\gamma_{cm}) \tag{5.43}$$

Here, also the domain of integration is over the range $\gamma_{min} \leq \gamma' \leq \gamma_{max}$ and $-1 \leq \mu \leq 1$ but here is without any restriction.

5.6.5 Pair emission, absorption and cross sections coefficients due Compton Scattering

The pair emission coefficient due to Compton scattering is defined by;

$$\eta(\gamma) = cn_{\gamma}(n_{+} + n_{-})r^2{}_e \int F_{\gamma}(\tilde{\epsilon}_1)F_e(\gamma_1) \times \frac{a+Y}{16\pi\epsilon\gamma\rho_1} \left| \frac{d\tilde{\epsilon}_1/d\gamma}{1+d\epsilon/d\gamma} \right| (d\mu d\mu' d\phi d\gamma_1) \tag{5.44}$$

In this equation,

$$Y = \frac{\rho_1}{\rho_2} + \frac{\rho_2}{\rho_1} + 2\left(\frac{1}{\rho_1} - \frac{1}{\rho_2}\right) + \left(\frac{1}{\rho_1} - \frac{1}{\rho_2}\right)^2 \tag{5.45}$$

Such that $\rho_1 = a_1\tilde{\epsilon}_1\gamma_1$ and $\rho_2 = a\tilde{\epsilon}_1\gamma$ and the region of integration is $\gamma_{min} \leq \gamma_1 \leq \gamma_{max}$ and $-1 \leq \mu, \mu' \leq 1$ and $0 \leq \phi \leq 2\pi$. However, this only holds when $\epsilon_{min} \leq \epsilon_1 \leq \epsilon_{max}$. On the other hand, the absorption coefficient of pairs due to Compton scattering is defined by;

$$\chi(\gamma) = \frac{cn_{\gamma}}{2} \int F_e(\epsilon)(1 - \beta\mu)\sigma_{total}(x) d\mu d\epsilon \tag{5.46}$$

The cross section σ_{total} is similar to the total photon cross section due to Compton scattering, which is given in Equation 5.35. In the above integrations (Equation 5.43 & 5.44), the region of integration is $-1 \leq \mu \leq 1$ and $\epsilon_{min} \leq \epsilon_1 \leq \epsilon_{max}$.

5.7 Cooling functions for Bremsstrahlung processes

The nature of the Bremsstrahlung process necessitate that, this process be treated as continuous in momentum and energy by using the common continuity equation (Pilla & Shaham, 1997). After some physical assumptions, the average cooling rate of these processes takes the following form;

$$|\dot{\gamma}| = E_{ep}(\gamma) + \int_1^{\infty} [E_{ee}(\gamma,\gamma') + E_{e\bar{e}}(\gamma,\gamma')] d\gamma' F_e(\gamma') \qquad (5.47)$$

The radiated energy per unit time (cooling rates) involved in this equation, is given as follows;

5.7.1 Electron (or positron)-proton collisions (E_{ep}):

The cooling rates for colliding electron (positron-proton) process, assuming proton at rest, can be expressed as function of energy ϵ of the emitted photons and cross section $\frac{d\sigma}{d\epsilon}$, as follows;

$$E_{ep}(\gamma) = cn_p \int_0^{\gamma-1} \epsilon \left(\frac{d\sigma}{d\epsilon}\right)_{proton} d\epsilon \qquad (5.48)$$

5.7.2 Positron-positron collision (E_{ee}):

The cooling rate for process is given by;

$$E_{ee}(\gamma,\gamma') = \frac{c({n_-}^2+{n_+}^2)(\gamma+\gamma')}{2n_e\gamma\gamma'} \int_{-1}^{1} p_c Q_{ee}(\epsilon_c, p_c) d\mu \qquad (5.49)$$

The cosine angle of this collision is; $\mu.\ p_c = \sqrt{\left(\xi - 1/_2\right)}$ And the energy of the emitted photons is $\epsilon_c = \sqrt{\xi + 1/_2}$ such that $\xi = \gamma\gamma'(1 - \beta\beta'\mu)$. However this process will have the following cooling function;

$$Q_{ee} \approx 8\alpha r_e{}^2 \frac{p_c{}^2}{\epsilon_c}\left[1 - \frac{4}{3}\frac{p_c}{\epsilon_c} + \frac{2}{3}\left(2 + \frac{p_c{}^2}{\epsilon_c{}^2}\right) ln(\epsilon_c + p_c)\right] \tag{5.50}$$

5.7.3 Positron (electron)-electron (positron) collision process ($E_{e\bar{e}}$):

The cooling rate for this interaction is given by;

$$E_{e\bar{e}}(\gamma,\gamma') = \frac{cn_+n_-(\gamma+\gamma')}{2n_e\gamma\gamma'}\int_{-1}^{1} p_c Q_{e\bar{e}}(\epsilon_c, p_c) d\mu \tag{5.51}$$

And the cooling function of this process is expressed as;

$$Q_{e\bar{e}} = \begin{cases} \frac{32}{2}\alpha r_e{}^2 \sum_{i=0}^{4} a_i p_c{}^i \text{ , } for\ E_c \leq 300KeV \\ 16\alpha r_e{}^2\left[\epsilon_c ln(\epsilon_c + p_c) - \frac{1}{6}\epsilon_c + \sum_{i=0}^{2} b_i \epsilon_c{}^{-i}\right] \quad \text{, } elsewhere \end{cases} \tag{5.52}$$

where $E_c = mc^2\epsilon_c$, and the values of a's are given in Pilla and Shaham (1997).

5.8 Collision integral for Coulomb collision

The combine effect of Moller and Bhabha collisions which collectively referred to Coulomb collision on the spectrum has been proposed by many researchers. Let the electrons has two different distribution functions; $f_1\ and\ f_2$. The corresponding distribution equation (Boltzmann) for f_1 is given by;

$$\frac{\partial f_1(p)}{\partial t} = -\frac{\partial S^i{}_1(p)}{\partial p^i} \tag{5.53}$$

The momentum space flux vector $S^i{}_1$ can be given as;

$$S^i{}_1(p) = \sum_{s=1}^{2}\int\left[f_1(p)\frac{\partial}{\partial p^{ij}} f_s(p^i) - f_s(p^i)\frac{\partial}{\partial p^i} f_1(p)\right] B^{ij} d^3p^i \tag{5.54}$$

where i, j are three-vector or tensor components. However, substituting this equation into the rate equations (Equation 2.8 of (Pilla & Shaham)), we get;

$$[\eta(\gamma) - \chi(\gamma)f(\gamma)]_1 = C_{11}(\gamma) + C_{12}(\gamma) \tag{5.55}$$

Such that C_{1s} is defined as;

$$C_{1s}(\gamma) = 4\pi^2 c r^2{}_e ln\Lambda_C B \frac{\partial}{\partial \gamma} \int \beta\beta'\gamma'^2 Q(\gamma,\gamma') d\gamma' \tag{5.56}$$

However, C_{11} is due to electrons collision for f_1 distribution and C_{12} is responsible for collision of electrons for f_1 distribution with f_2. And the cooling function is given by:

$$Q(\gamma,\gamma') = \left[f_1(\gamma)\frac{\partial f_s(\gamma')}{\partial \gamma'} - f_s(\gamma')\frac{\partial}{\partial \gamma} f_1(\gamma)\right] \int_{-1}^{1} B_0(\gamma,\gamma',\mu) d\mu \tag{5.57}$$

Where;

$$B_0 = \frac{\xi^2}{\gamma\gamma'(\xi^2-1)^{3/2}} (\xi^2 - 1 - \beta^2\gamma^2 - \beta'^2\gamma'^2\mu^2 + 2\beta\beta'\gamma\gamma'\mu\xi) \tag{5.58}$$

After many physical and mathematical assumptions and substitutions, Equation 5.53 becomes;

$$\frac{\partial}{\partial t} f_1(\gamma) = -\beta \frac{\partial}{\partial \gamma} \int 2\pi\beta\beta'\gamma'^2 B \mathfrak{D}_1(\gamma,\gamma') d\mu d\gamma' \tag{5.59}$$

Such that;

$$\mathfrak{D}_1(\gamma,\gamma') = \sum_{s=1}^{2} \left[f_1(\gamma)\frac{\partial}{\partial \gamma'} f_s(\gamma') - f_s(\gamma')\frac{\partial}{\partial \gamma} f_1(\gamma)\right] \tag{5.60}$$

5.9 Kinetic and Thermal equilibria of pair plasma: The Temperature and Densities

The description of the analytical expressions for the pair plasma equilibrium states can be derive from boundary conditions presented in previous sections. Assuming an isotropic, stationary, non-magnetized and homogeneous system of pair plasma with zero hydrodynamic and radiative transfer effects; the kinetics can be derive from the simple rate equations, given by Equation 5.18, assuming that the system is on a short timescales given by;

$$t \approx t_{Th} = \frac{1}{(n_+ \sigma_{Th} c)} \tag{5.61}$$

To determine the time evolution of the distributions, let assume a system of pair plasma consisting of protons(P), electrons(e^-), Positrons (e^+) and Photons (γ) with densities $n_p, n_-, n_+ \; and \; n_\gamma$ respectively, and having time-dependent spectral functions $F_e(\gamma) \; and \; F_\gamma(\epsilon)$. Here the number density of the electron takes the form; $n_- = n_+ + n_p$. However, for simplified kinetic equations, we assume that the particle number is conserved, such that $n_- = n_+ = n_e$ and $F_-(\gamma) = F_+(\gamma) = F_e(\gamma)$. The photons, positron and electron spectral functions are generally defined by;

$$F_\gamma(\epsilon) = \frac{4\pi\epsilon^2}{n_\gamma} f_\gamma(\epsilon) \text{ and } F_\pm(\gamma) = \frac{4\pi\beta\gamma^2}{n_\pm} f_\pm(\gamma) \tag{5.62}$$

The initial state of the system is defined at $t = 0$, and the total particle density and total energy density can be, respectively, given by;

$$\tilde{n} = n_\gamma + 2n_+ + n_p \text{ and } \tilde{u} = u_\gamma + u_- + u_+ \tag{5.63}$$

where $u_\gamma = n_\gamma \int_0^\infty \epsilon F_\gamma(\epsilon) d\epsilon$ and $u_\pm = n_\pm \int_1^\infty \gamma F_\pm(\gamma) d\gamma$, such that the average energy per particle is $\bar{\epsilon} = {}^{\tilde{u}}/_{\tilde{n}}$. This system of pair plasma will approach equilibrium state in two different phases(Pilla & Shaham, 1997), which are discussed as follows;

5.9.1 Kinetic equilibrium phase:

The Compton scattering, pair annihilation and creation operates on a shorter timescales (faster phase), such that both total particle density $\tilde{\boldsymbol{n}}$ and total energy density $\tilde{\boldsymbol{u}}$ are constants. This will lead to a Kinetic equilibrium which is achieved by separate disappearance of the total reaction rates for the Compton scattering and the pair annihilation. This equilibrium phase is defined by a temperature $\tilde{\Theta}$ and the chemical potentials $\tilde{\mu}_\gamma$ and $\tilde{\mu}_\pm$.

The total reaction rate for Compton scattering which disappears, we can then have;

$$f(\gamma) f_\gamma(\epsilon) \left[1 + \frac{{\lambda_0}^3}{2} f_\gamma(\epsilon')\right] = f(\gamma') f_\gamma(\epsilon') \left[1 + \frac{{\lambda_0}^3}{2} f_\gamma(\epsilon)\right] \tag{5.64}$$

where γ and ϵ and $\gamma'$and ϵ' are electron and photon energies before and after scattering respectively. And $\lambda_0 = {}^{h}/_{mc}$. However, the distribution functions are defined by;

$$f_\pm(\gamma) = \frac{2}{{\lambda_0}^3} e^{\left(\mu_\pm - \gamma /_{\Theta_\pm}\right)} \text{ and } f_\gamma(\epsilon) = \frac{2}{{\lambda_0}^3 e^{\left(\epsilon - \mu_\gamma /_{\Theta_\gamma}\right)} - 1} \tag{5.65}$$

Similarly, the total reaction rate for the pair creation and annihilation should disappear and hence, we get;

$$f_\gamma(\epsilon_1) f_\gamma(\epsilon_2) = f_+(\gamma_+) f_-(\gamma_-) \left[1 + \frac{{\lambda_0}^3}{2} f_\gamma(\epsilon_1)\right] \left[1 + \frac{{\lambda_0}^3}{2} f_\gamma(\epsilon_2)\right] \tag{5.66}$$

where $\epsilon_{1,2}$ and $\gamma_{1,2}$ are the photons and pairs energies respectively. And the distribution functions in the kinetic equilibrium becomes;

$$f_\gamma(\epsilon) = \frac{2}{{\lambda_0}^3} exp\left(\frac{\tilde{\mu}_\gamma - \epsilon}{\widetilde{\Theta}}\right) \text{ and } f_\pm(\gamma) = \frac{2}{{\lambda_0}^3} exp\left(\frac{\tilde{\mu}_\pm - \gamma}{\widetilde{\Theta}}\right) \tag{5.67}$$

In this equation, we assume that $\Theta_+ = \Theta_\gamma = \Theta_-$ which is represented by $\widetilde{\Theta}$, and $\check{\mu}_- + \check{\mu}_+ = 2\check{\mu}_\gamma$. The photon density would therefore become;

$$\tilde{n}_\gamma = \int_0^\infty 4\pi\epsilon^2 f_\gamma(\epsilon) d\epsilon = 16\pi \left(\frac{\widetilde{\Theta}}{\lambda_0}\right)^3 \exp\left(\frac{\tilde{\mu}_\gamma}{\widetilde{\Theta}}\right) \tag{5.68}$$

And

$$\tilde{n}_\pm = \int_1^\infty 4\pi\gamma\sqrt{\gamma^2 - 1} f_\pm(\gamma) d\gamma = \frac{8\pi}{{\lambda_0}^3} \widetilde{\Theta} K_2\left(\frac{1}{\widetilde{\Theta}}\right) \exp\left(\frac{\tilde{\mu}_\pm}{\widetilde{\Theta}}\right) \tag{5.69}$$

where K_2 is the second-order modified Bessel function. However, in the absence of ions in the plasma $n_p = 0$, we have $\tilde{\mu}_- = \tilde{\mu}_+ = \tilde{\mu}_\gamma$ such that;

$$\tilde{n}_- = \tilde{n}_+ = \frac{K_2\left({}^1/_{\widetilde{\Theta}}\right)}{2\left[\widetilde{\Theta}^2 + K_2\left({}^1/_{\widetilde{\Theta}}\right)\right]} \tilde{n} \tag{5.70}$$

And

$$\tilde{n}_\gamma = \frac{\widetilde{\Theta}^2}{\widetilde{\Theta}^2 + K_2\left({}^1/_{\widetilde{\Theta}}\right)} \tilde{n} \tag{5.71}$$

However, the energy equations will be required in the temperature relations. These different energies are given by;

$$\tilde{\mu}_\gamma = \int_0^\infty 4\pi\epsilon^3 f_\gamma(\epsilon) d\epsilon = 3\widetilde{\Theta}\tilde{n}_\gamma \tag{5.72}$$

And

$$\tilde{\mu}_{\pm} = \int_1^{\infty} \gamma^2 \sqrt{\gamma^2 - 1} f_{\pm}(\gamma) d\gamma = \frac{3\tilde{\Theta} K_2\left(1/_{\tilde{\Theta}}\right) + K_1\left(1/_{\tilde{\Theta}}\right)}{K_2\left(1/_{\tilde{\Theta}}\right)} \tilde{n}_{\pm} \tag{5.73}$$

Thus, for non-ion plasma ($n_p = 0$), using conservation of energy ($\tilde{\mu} = \tilde{\mu}_{\gamma} + \tilde{\mu}_{-} + \tilde{\mu}_{+}$), Equations 5.72 and 5.73, becomes;

$$\tilde{\mu}_{\gamma} = \frac{3\tilde{\Theta}^3}{\tilde{\Theta}^2 + K_2\left(1/_{\tilde{\Theta}}\right)} \tilde{n} \tag{5.74}$$

And

$$\tilde{\mu}_{+} + \tilde{\mu}_{-} = \frac{3\tilde{\Theta} K_2\left(1/_{\tilde{\Theta}}\right) + K_1\left(1/_{\tilde{\Theta}}\right)}{\tilde{\Theta}^2 + K_2\left(1/_{\tilde{\Theta}}\right)} \tilde{n} \tag{5.75}$$

The temperature relations as function of total energy and density, can be given as;

$$3\tilde{\Theta}^3 + 3\tilde{\Theta} K_2\left(1/_{\tilde{\Theta}}\right) + K_1\left(1/_{\tilde{\Theta}}\right) = \tilde{\epsilon}\left(\tilde{\Theta}^2 + K_2\left(1/_{\tilde{\Theta}}\right)\right) \tag{5.76}$$

Equation 5.76 describes the temperature equation in Kinetic equilibrium phase of pair plasma which is applicable to all ranges of energy (both relativistic and otherwise) and density (but only for non-degenerate plasma). Where $\boldsymbol{\tilde{\epsilon}}$ stands for average energy per particle and can be determined by the initial conditions.

5.9.2 Thermal equilibrium phase:

Processes that operates on a longer timescales (slower phase) $t \approx {}^{t_{Th}}/_{\alpha}$ (α is constant) such that only the total energy density $\tilde{u}$ is constant, but the total particle density $\tilde{n}$ changes. This is primarily due to Bremsstrahlung and other radiative processes, and the system is finally in thermal equilibrium which is defined by a density n_0 and a temperature Θ_0. For $\Theta_0 < \tilde{\Theta}$, the density is $\mathrm{n}_0 > \tilde{n}$, and the system is cooled by plasma by means of Bremsstrahlung and other similar processes. But when $\Theta_0 > \widetilde{\Theta}$, then the system is heated up by a plasma process consisting only of inverse Bremsstrahlung and other radiative processes. In this phase, we have $\mu_- + \mu_+ = 2\mu_\gamma$ such that $\mu_- = \mu_+ = \mu_0$, and let $x = \exp\left({}^{\mu_0}/{}_{\Theta_0}\right)$, hence, the densities becomes;

$$n_\pm = \frac{8\pi}{{\lambda_0}^3}\Theta_0 K_2\left(\frac{1}{\Theta_0}\right)x^\pm \quad \text{and} \quad n_\gamma = \frac{16\pi{\Theta_0}^3}{{\lambda_0}^3} \tag{5.77}$$

However, the sum of the electron and positron densities, assuming$n_- = n_p + n_+$, can be given as;

$$n_- + n_+ = \frac{16\pi}{{\lambda_0}^3}\Theta_0 K_2\left(\frac{1}{\Theta_0}\right)\sqrt{1+y^2} \tag{5.78}$$

This is the relativistic pair density equation, such that $y = {}^{{\lambda_0}^3 n_p}\Big/{}_{\left[16\Theta_0 K_2\left(\frac{1}{\Theta_0}\right)\right]}$.

whereas, for non-relativistic limit, this equation becomes;

$$n_- + n_+ = \frac{4}{{\lambda_0}^3}(2\pi\Theta_0)^{3/2}\exp(-1/\Theta_0) \times \left[1 + \frac{15}{8}\Theta_0 + \frac{105}{128}{\Theta_0}^2\right]\sqrt{1+y^2} \tag{5.79}$$

However, the energy density of the pairs is given by;

$$u_- + u_+ = \frac{16\pi}{{\lambda_0}^3}\left[3{\Theta_0}^2 K_2\left({}^1/{}_{\Theta_0}\right) + \Theta_0 K_1\left({}^1/{}_{\Theta_0}\right)\right]\sqrt{1+y^2} \tag{5.80}$$

And with the conservation of energy, we get the analytical expression for the thermal equilibrium phase, as follows;

$$ {\lambda_0}^3\tilde{\mu} = 16\pi\left[3{\Theta_0}^2 K_2\left({}^1/{}_{\Theta_0}\right) + \Theta_0 K_1\left({}^1/{}_{\Theta_0}\right)\right]\sqrt{1+y^2} + \frac{8\pi^5{\Theta_0}^4}{15} \tag{5.81}$$

The second term on the right-hand side of this equation is the contribution due to photons effect. This method is exact and applicable for energies, both relativistic and otherwise, and for all non-degenerate plasma densities.

CHAPTER 6: CONCLUSIONS AND RECOMMENDATIONS

The goal of this chapter is to appraise on conclusive summary and contributions of this work as well as provide possible recommendations (in addition to Chapter 5) for future work.

6.1 Conclusion

In this work, models are constructed into two different routines (namely Helm-EoS and SNEUT4 code). These models are used to post-process already established grids of stellar evolution models which are predicted to explode as PISN. Specifically these routines are; first, a thermodynamically consistent equation of state table (Helm-EoS) which is used to addressed number one and two objectives of this research. And secondly, an SNEUT4 code for calculations of neutrino energy-loss rates. The progenitor models considered are those predicted to be within carbon-oxygen cores, in the range of 60 $M_{\odot} < M_{CO} < 130$ $M_{\odot}$. These Grids of models are applied into a constructed model of HELM-EoS routine for calculation of first and second objectives, namely;

1. The electron-positron adiabatic properties, such as heat capacities and adiabatic indices
2. The thermal energies, pressure, and entropy of the electron-positron pairs.

These calculations were carried out within the instability regions of the progenitor models. Furthermore, the third objective is addressed by calculating neutrino energy-losses due to pair neutrino process from same progenitor models using model constructed into the SNEUT4 code. The last objective was to evaluate the neutrino energy loss from 120, 150, 200, 300, 500 $M_{\odot}$, with rotation and 120, 150 and 500 $M_{\odot}$ with no rotation, with $Z = 0.006$ at LMC.

It is interesting to note that pair-productions' adiabatic quantities show similar dynamics in all rotating models within the instability regions, while non-rotating model possess different pattern of instability. The amount of heat required to raise central temperature high, which is necessary for PISN explosion is found to decrease. Moreover, effects of electron-positron thermal energies, pressure, and entropy on endpoints of the progenitor models under consideration are evaluated and analysed. Rotating 200 $M_\odot$ model showed highest electron-positron thermal energy of about 3.29×10^{17} [erg g^{-1}] while non-rotating 500 $M_\odot$ model almost lose its electron-positron thermal energy and die before reaching the instability region. This energy is needed to overcome contraction of the stars and for complete annihilation of electron-positron pairs. Finally, neutrino energy-loss rates from same progenitors is calculated and its effect is analysed as it affects end fates of the progenitor models.

6.2 Implication of the Research

The implication of this work is that; it provides additional information which could help for better understanding of final fates of the selected massive star models. Furthermore, the energy loss through neutrino processes is important, especially when the determination of the impacts of these energies in high mass stars is still on going.

6.3 Contributions to Knowledge

Summarily, the current study showed that effects of electron-positron pair-production and neutrino cooling serves as main triggering processes for understanding end fates of very-massive stars and are significantly imperative for better predictions of the fates of any massive star. However, these two mechanisms which are paramount in explosion of massive stars are particularly ongoing in astrophysics community and in neutrino physics. Our results would, therefore, contribute in search for full understanding of end fates of the selected stellar models.

6.4 Limitations of the Research

This work is limited to post-processing the already established grids of stellar models which were predicted to explode as PISN. Specifically, those progenitors that are within carbon-oxygen cores, in the range of 60 $M_{\odot} < M_{CO} < 130$ $M_{\odot}$. Only stellar evolution properties within the instability regions of those progenitor models are post-processed using thermodynamically consistent Helm-EoS. In the last part of the work, dominant neutrino energy-loss (which is pair neutrino energy-loss rate) within the instability regions is calculated using SNEUT4 code. All other neutrino energy-loss rates of less important in the instability region is ignored. We also evaluated neutrino energy loss from stellar models of 120, 150, 200, 300, 500 $M_{\odot}$, with rotation and 120, 150 and 500 $M_{\odot}$ with no rotation, for $Z = 0.006$ at LMC.

6.5 Recommendations for Further Work

Chapter five is for full recommendation of future work. Meanwhile, in this work, production of electron-positron pairs and neutrino cooling from the instability regions of very-massive stars have been examined for better understanding of their end fates. The calculation for energy loss through thermal neutrino processes is also investigated for the selected stellar models. Based on the results obtained, further works could be suggested as follows:

1. For complete understanding of final fates of massive stars, thermal energy, pressure and entropy contributions from fundamental species; photons, nuclei, electrons, and positron could be very important.
2. Considering effects of convective stability of these massive stars, contribution of the convective instability could give more information about the stability and fates of these massive stars.

3. Complete investigations of Chapter 5 is recommended. The overall effects of all plasma processes in massive stars will contribute in understanding the exact final fates of these very-massive stars.
4. Finally, in case of 120, 150, 200, 300 and 500 M⊙ models, as we have shown in section (2.5.3) that neutrino energy-loss by neutrino oscillations could be calculated by considering the modified stopping power equation and using other properties of the stellar evolution involved, such as electron density and temperature of the star. The electron density, in particular, is significantly important due to its effect on total energy-loss. For example, the following cases of three survival probabilities of electron neutrinos for neutrino transformations, could be chosen, in order to calculate the energy-loss through neutrino oscillations. These probabilities are:
    a. Case I ($P_{\nu_e \to \nu_e} = 0.0$): In this case, electron neutrinos are completely transformed into another flavour; either muon or tau neutrinos.
    b. Case II ($P_{\nu_e \to \nu_e} = 0.5$): This is where only half of electron neutrino will be transformed into another flavour.
    c. Case III ($P_{\nu_e \to \nu_e} = 1.0$): Here none of electron neutrino is transformed into another. All electron neutrinos in this case will remain as electron neutrinos.

In all of these cases, the calculated energy-loss per neutrino is measured in (MeV) while the total energy-loss ΔE_{ν} is in ($MeV/cm^3/s$).

REFERENCES

Aartsen, M., Abraham, K., Ackermann, M., Adams, J., Aguilar, J., Ahlers, M., . . . Anderson, T. (2017). All-sky search for time-integrated neutrino emission from astrophysical sources with 7 yr of IceCube data. *The Astrophysical Journal, 835*(2), 151-166.

Abel, T., Anninos, P., Norman, M. L., & Zhang, Y. (1998). First structure formation. I. Primordial star-forming regions in hierarchical models. *The Astrophysical Journal, 508*(2), 518-529.

Abel, T., Bryan, G. L., & Norman, M. L. (2000). The formation and fragmentation of primordial molecular clouds. *The Astrophysical Journal, 540*(1), 39-44.

Andriesse, C. (2000). On the relation between stellar mass loss and luminosity. *The Astrophysical Journal, 539*(1), 364-365.

Angulo, C., Arnould, M., Rayet, M., Descouvemont, P., Baye, D., Leclercq-Willain, C., . . . Rolfs, C. (1999). A compilation of charged-particle induced thermonuclear reaction rates. *Nuclear Physics A, 656*(1), 3-183.

Arnett, D. (1996). *Supernovae and nucleosynthesis : an investigation of the history of matter, from the big bang to the present*. Princeton, N.J. : Princeton University Press, 1996.

Arnett, W. D. (1972). Advanced evolution of massive stars. I. Helium burning. *The Astrophysical Journal, 176*, 681-698.

Barkat, Z., Rakavy, G., & Sack, N. (1967). Dynamics of supernova explosion resulting from pair formation. *Physical Review Letters, 18*(10), 379-381.

Barniske, A., Oskinova, L., & Hamann, W.-R. (2008). Two extremely luminous WN stars in the Galactic center with circumstellar emission from dust and gas. *Astronomy & Astrophysics, 486*(3), 971-984.

Beaudet, G., Petrosian, V., & Salpeter, E. (1967). Energy losses due to neutrino processes. *The Astrophysical Journal, 150*, 979-999.

Belczynski, K., Heger, A., Gladysz, W., Ruiter, A., Woosley, S., Wiktorowicz, G., . . . Holz, D. (2016). The effect of pair-instability mass loss on black-hole mergers. *Astronomy & Astrophysics, 594*, A97-A107.

Bestenlehner, J. M., Gräfener, G., Vink, J. S., Najarro, F., de Koter, A., Sana, H., . . . Herrero, A. (2014). The VLT-FLAMES Tarantula Survey-XVII. Physical and wind properties of massive stars at the top of the main sequence. *Astronomy & Astrophysics, 570*, A38-A129.

Bestenlehner, J. M., Vink, J. S., Gräfener, G., Najarro, F., Evans, C., Bastian, N., . . . Doran, E. (2011). The VLT-FLAMES Tarantula Survey-III. A very massive star in apparent isolation from the massive cluster R136. *Astronomy & Astrophysics, 530*, L14-L19.

Bethe, H. A. (1986). Possible explanation of the solar-neutrino puzzle. *Physical Review Letters, 56*(12), 1305-1308.

Beule, D., Ebeling, W., & Förster, A. (1997). Adiabatic equation of state and ionization equilibrium of dense plasma. *Physica A: Statistical Mechanics and its Applications, 241*(3-4), 719-728.

Bilenky, S., & Pontecorvo, B. (1976). Again on Neutrino Oscillations. *Lettere al Nuovo Cimento, 17*, 569-571.

Bilenky, S. M., Giunti, C., & Grimus, W. (1999). Phenomenology of neutrino oscillations. *Progress in Particle and Nuclear Physics, 43*, 1-86.

Bilenky, S. M., & Pontecorvo, B. (1978). Lepton mixing and neutrino oscillations. *Physics Reports, 41*(4), 225-261.

Blinnikov, S. I., Dunina-Barkovskaya, N., & Nadyozhin, D. (1996). Equation of state of a Fermi gas: approximations for various degrees of relativism and degeneracy. *The Astrophysical Journal Supplement Series, 106*, 171-203.

Bond, J., Arnett, W., & Carr, B. (1984). The evolution and fate of very massive objects. *The Astrophysical Journal, 280*, 825-847.

Bromm, V. (2005). Formation of the First Stars. *Proceedings of the International Astronomical Union, 1*(S228), 121-128.

Bromm, V., Coppi, P. S., & Larson, R. B. (2002). The formation of the first stars. I. The primordial star-forming cloud. *The Astrophysical Journal, 564*(1), 23-51.

Bromm, V., & Larson, R. B. (2004). The first stars. *Annual Review Astronomy Astrophysics, 42*, 79-118.

Callen, H. B. (1985). *Thermodynamics and an introduction to thermostatistics*. Canada: John Wiley & Sons, Inc.

Carr, B., Bond, J., & Arnett, W. (1984). Cosmological consequences of Population III stars. *The Astrophysical Journal, 277*, 445-469.

Chabrier, G., & Potekhin, A. Y. (1998). Equation of state of fully ionized electron-ion plasmas. *Physical Review E, 58*(4), 4941-4949.

Chatzopoulos, E., & Wheeler, J. C. (2012a). Effects of Rotation on the Minimum Mass of Primordial Progenitors of Pair-instability Supernovae. *The Astrophysical Journal, 748*(1), 42-52.

Chatzopoulos, E., & Wheeler, J. C. (2012b). Hydrogen-Poor Circumstellar Shells from Pulsational Pair-Instability Supernovae with Rapidly Rotating Progenitors. *Astrophysical Journal, 760*(2), 154-159.

Cherry, J. F. (2012). *Neutrino flavor transformation in core-collapse supernovae.* UC San Diego.

Cooke, J., Sullivan, M., Gal-Yam, A., Barton, E. J., Carlberg, R. G., Ryan-Weber, E. V., . . . Díaz, C. G. (2012). Superluminous supernovae at redshifts of 2.05 and 3.90. *Nature, 491*(7423), 228-231.

Coppi, P. S. (1992). Time-dependent models of magnetized pair plasmas. *Monthly Notices of the Royal Astronomical Society, 258*(4), 657-683.

Crowther, P. A., Caballero-Nieves, S. M., Bostroem, K. A., Apellániz, J. M., Schneider, F. R. N., Walborn, N. R., . . . Vink, J. S. (2016). The R136 star cluster dissected with Hubble Space Telescope/STIS. I. Far-ultraviolet spectroscopic census and the origin of He ii λ1640 in young star clusters. *Monthly Notices of the Royal Astronomical Society, 458*(1), 624-659.

Crowther, P. A., Schnurr, O., Hirschi, R., Yusof, N., Parker, R. J., Goodwin, S. P.,…… Kassim, H. A. (2010). The R136 star cluster hosts several stars whose individual masses greatly exceed the accepted 150 M⨀ stellar mass limit. *Monthly Notices of the Royal Astronomical Society, 408*(2), 731-751.

De Becker, M., Rauw, G., Manfroid, J., & Eenens, P. (2006). Early-type stars in the young open cluster IC 1805-II. The probably single stars HD 15570 and HD 15629, and the massive binary/triple system HD 15558. *Astronomy & Astrophysics, 456*(3), 1121-1130.

Duan, H., Fuller, G. M., Carlson, J., & Qian, Y.-Z. (2006). Simulation of coherent nonlinear neutrino flavor transformation in the supernova environment: Correlated neutrino trajectories. *Physical Review D, 74*(10), 105014-1-22.

Duan, H., Fuller, G. M., & Qian, Y.-Z. (2010). Collective Neutrino Oscillations. *Annual Review of Nuclear and Particle Science, 60*, 569-594.

Duan, H., & Kneller, J. P. (2009). Neutrino flavour transformation in supernovae. *Journal of Physics G: Nuclear and Particle Physics, 36*, 113201 (43pp).

Eggenberger, P., Meynet, G., Maeder, A., Hirschi, R., Charbonnel, C., Talon, S.,…….. Ekström, S. (2009). The Geneva stellar evolution code. *Evolution and Seismic Tools for Stellar Astrophysics*, 43-54.

Ekström, S., Georgy, C., Eggenberger, P., Meynet, G., Mowlavi, N., Wyttenbach, A., . . . Frischknecht, U. (2012). Grids of stellar models with rotation-I. Models from 0.8 to 120 M⨀ at solar metallicity (Z= 0.014). *Astronomy & Astrophysics, 537*, A146-A164.

El Eid, M., & Hilf, E. (1977). Equation of state for hot and dense n, p, e-mixture with zero charge density. *Astronomy and Astrophysics, 57*, 243-249.

El Eid, M. F., Fricke, K. J., & Ober, W. (1983). Evolution of massive pregalactic stars. I-Hydrogen and helium burning. II-Nucleosynthesis in pair creation supernovae and pregalactic enrichment. *Astronomy and Astrophysics, 119*, 54-68.

Eliezer, S., & Swift, A. R. (1976). Experimental consequences of νe− νμ mixing in neutrino beams. *Nuclear Physics B, 105*(1), 45-51.

Esposito, S., Mangano, G., Miele, G., Picardi, I., & Pisanti, O. (2002). Radiative corrections to neutrino energy loss rate in stellar interiors. *Modern Physics Letters A, 17*(08), 491-502.

Esposito, S., Mangano, G., Miele, G., Picardi, I., & Pisanti, O. (2003). Neutrino energy loss rate in a stellar plasma. *Nuclear Physics B, 658*(1-2), 217-253.

Fabian, A., Blandford, R., Guilbert, P., Phinney, E., & Cuellar, L. (1986). Pair-induced spectral changes and variability in compact X-ray sources. *Monthly Notices of the Royal Astronomical Society, 221*(4), 931-945.

Fantini, G., Rosso, A. G., Vissani, F., & Zema, V. (2018). The formalism of neutrino oscillations: an introduction. *arXiv preprint arXiv:1802.05781.*

Fowler, W. A. (1966). The stability of supermassive stars. *The Astrophysical Journal, 144*, 180-200.

Fowler, W. A., & Hoyle, F. (1964). Neutrino Processes and Pair Formation in Massive Stars and Supernovae. *The Astrophysical Journal Supplement Series, 9*, 201-319.

Fraley, G. S. (1968). Supernovae explosions induced by pair-production instability. *Astrophysics and Space Science, 2*(1), 96-114.

Fritsch, H., & Minkowski, P. (1976). Vectorlike weak currents, massive neutrinos, and neutrino beam oscillations. *Physics Letters B, 62*(1), 72-76.

Gal-Yam, A., Mazzali, P., Ofek, E., Nugent, P., Kulkarni, S., Kasliwal, M., . . . Chornock, R. (2009). Supernova 2007bi as a pair-instability explosion. *Nature, 462*(7273), 624-627.

Garmany, C. D., & Massey, P. (1981). HD 15558: An Extremely Luminous O-Type Binary Star. *Publications of the Astronomical Society of the Pacific, 93*(554), 500-503.

Ghisellini, G. (1987). Pair production in synchrotron self-Compton models: the case of one generation of pairs. *Monthly Notices of the Royal Astronomical Society, 224*(1), 1-12.

Giunti, C., Kim, C., & Lee, U. (1998). When do neutrinos cease to oscillate? *Physics Letters B, 421*(1-4), 237-244.

Giunti, C., & Kim, C. W. (2007). *Fundamentals of neutrino physics and astrophysics*: Oxford university press.

Guilbert, P., Fabian, A., & Rees, M. (1983). Spectral and variability constraints on compact sources. *Monthly Notices of the Royal Astronomical Society, 205*(3), 593-603.

Hainich, R., Ruehling, U., Todt, H., Oskinova, L. M., Liermann, A., Gräfener, G., . . . Hamann, W.-R. (2014). The Wolf-Rayet stars in the Large Magellanic Cloud-A comprehensive analysis of the WN class. *Astronomy & Astrophysics, 565*, A27-A89.

Hansen, C. J., Kawaler, S. D., & Trimble, V. (2004). Structure and evolution of the sun: Stellar Interiors (pp. 431-465): Springer.

Heger, A., Fryer, C., Woosley, S., Langer, N., & Hartmann, D. H. (2003). How massive single stars end their life. *The Astrophysical Journal, 591*(1), 288-300.

Heger, A., & Woosley, S. E. (2002). The nucleosynthetic signature of population III. *The Astrophysical Journal, 567*(1), 532-543.

Humphreys, R. (1983). The brightest stars as extragalactic distance indicators. *The Astrophysical Journal, 269*, 335-351.

Itoh, N., Adachi, T., Nakagawa, M., Kohyama, Y., & Munakata, H. (1989). Neutrino energy loss in stellar interiors. III-Pair, photo-, plasma, and bremsstrahlung processes. *The Astrophysical Journal, 339*, 354-364.

Itoh, N., Hayashi, H., Nishikawa, A., & Kohyama, Y. (1996). Neutrino energy loss in stellar interiors. VII. Pair, photo-, plasma, bremsstrahlung, and recombination neutrino processes. *The Astrophysical Journal Supplement Series, 102*, 411-424.

Itoh, N., & Kohyama, Y. (1983). Neutrino-pair bremsstrahlung in dense stars. I-Liquid metal case. *The Astrophysical Journal, 275*, 858-866.

Itoh, N., Kohyama, Y., Matsumoto, N., & Seki, M. (1984). Neutrino-pair bremsstrahlung in dense stars. IV-Phonon contributions in the crystalline lattice phase. *The Astrophysical Journal, 285*, 304-311.

Janka, H.-T. (2016). Neutrino Emission from Supernovae. *Handbook of Supernovae*, 1-30.

Janka, H.-T. (2017). Neutrino Emission from Supernovae. *arXiv preprint arXiv:1702.08713*.

Jing-Jing, L., & Zhi-Quan, L. (2009). The Pair Neutrino Energy Loss for Nuclei 56Fe at the Late Stages of Stellar Evolution. *Romanian Journal of Physics, 54*(1-2), 157-164.

Johns, S., Ellis, P. J., & Lattimer, J. (1996). Numerical approximation to the thermodynamic integrals. *The Astrophysical Journal, 473*(2), 1020-1028.

Kasen, D., Woosley, S., & Heger, A. (2011). Pair instability supernovae: light curves, spectra, and shock breakout. *The Astrophysical Journal, 734*(2), 102-125.

Kippenhahn, R., Weigert, A., & Weiss, A. (1990). *Stellar structure and evolution* (Vol. 282): Springer-Verlag Berlin Heidelberg.

Kirzhnits, D., Losyakov, V., & Chechin, V. (1990). Neutrino energy losses in matter. *Zhurnal Ekspermentalnoi I Teoreticheskoi Fiziki, 97*(4), 1089-1102.

Kohyama, Y., Itoh, N., Obama, A., & Hayashi, H. (1994). Neutrino energy loss in stellar interiors. 6. Axial vector contribution to the plasma neutrino energy-loss rate for strongly degenerate electrons. *The Astrophysical Journal, 431*, 761-766.

Kotake, K., Sato, K., & Takahashi, K. (2006). Explosion mechanism, neutrino burst and gravitational wave in core-collapse supernovae. *Reports on Progress in Physics, 69*(4), 971-1143.

Kozyreva, A. (2014). *Pair instability supernovae: Evolution, explosion, nucleosynthesis.* (Doctor of Philosophy), University of Bonn, Bonn, Germany.

Kozyreva, A., Blinnikov, S., Langer, N., & Yoon, S. C. (2014). Observational properties of low-redshift pair instability supernovae. *Astronomy & Astrophysics,* 565, A70-A83.

Kozyreva, A., Gilmer, M., Hirschi, R., Fröhlich, C., Blinnikov, S., Wollaeger, R. T., . . . Even, W. P. (2016). Fast evolving pair-instability supernova models: evolution, explosion, light curves. *Monthly Notices of the Royal Astronomical Society, 464*(3), 2854-2865.

Kozyreva, A., Yoon, S.-C., & Langer, N. (2014). Explosion and nucleosynthesis of low-redshift pair-instability supernovae. *Astronomy & Astrophysics, 566*, A146-A156.

Kunugise, T., & Iwamoto, K. (2007). Neutrino emission from type Ia supernovae. *Publications of the Astronomical Society of Japan, 59*(6), L57-L61.

Langer, N., Norman, C., de Koter, A., Vink, J., Cantiello, M., & Yoon, S.-C. (2007). Pair creation supernovae at low and high redshift. *Astronomy & Astrophysics, 475*(2), L19-L23.

Ledoux, P. (1946). On the Dynamical Stability of Stars. *The Astrophysical Journal, 104*, 333-346.

Leventhal, M., MacCallum, C., & Stang, P. (1978). Detection of 511 keV positron annihilation radiation from the galactic center direction. *The Astrophysical Journal, 225*, L11-L14.

Limongi, M., Straniero, O., & Chieffi, A. (2000). Massive Stars in the Range 13-25 M$\odot$: Evolution and Nucleosynthesis. II. The Solar Metallicity Models. *The Astrophysical Journal Supplement Series, 129*(2), 625-664.

Lunardini, C. (2015). *Theory and phenomenology of supernova neutrinos.* AIP Conference Proceedings 1666, 070001, paper presented at 26TH International conference on Neeutrino Physics and Astrophysics, June 2014, Boston, Massachusetts, USA.

Lunnan, R., Chornock, R., Berger, E., Milisavljevic, D., Jones, D., Rest, A., . . . Drout, M. (2016). PS1-14bj: A Hydrogen-poor Superluminous Supernova with a long rise and slow decay. *The Astrophysical Journal, 831*(2), 144-159.

Maeder, A. (2008). *Physics, formation and evolution of rotating stars*: Springer Science & Business Media.

Maeder, A., & Meynet, G. (2011). Rotating massive stars through the ages, with applications to WR stars, Pop III stars and Gamma Ray Bursts. *arXiv preprint arXiv:1109.6171.*

Maeder, A., & Meynet, G. (2012). Rotating massive stars: From first stars to gamma ray bursts. *Reviews of Modern Physics, 84*(1), 25-63.

Martins, F. (2015). *Empirical Properties of Very Massive Stars*. Astrophysics and Space science Library, Vol, 412, Springer, Cham.

Maurizio, S., & Santi, C. (2005). *Evolution of Stars and Stellar Populations*. The Atrium, Southern Gate, Chichester, West Sussex, England: John Wiley & Sons Ltd.

Mazets, E., Golenetskii, S., Ilyinskii, V., Guryan, Y. A., Aptekar, R., Panov, V., . . . Kharitonova, T. (1982). Cosmic gamma-ray burst spectroscopy. *Astrophysics and Space Science, 82*(2), 261-282.

Mikheyev, S., & Smirnov, A. Y. (1986). Resonant amplication of neutrino oscillations in matter and solar-neutrino spectroscopy. *Nuovo Cimento C, 9*, 17-26.

Mirizzi, A., Tamborra, I., Janka, H.-T., Saviano, N., Scholberg, K., Bollig, R.,…. Chakraborty S. (2016). Supernova neutrinos: production, oscillations and detections. *Rivista del Nuovo Cimento, 39*, 1-2.

Montero, P. J., Janka, H.-T., & Müller, E. (2012). Relativistic collapse and explosion of rotating supermassive stars with thermonuclear effects. *The Astrophysical Journal, 749*(1), 37-51.

Munakata, H., Kohyama, Y., & Itoh, N. (1985). Neutrino energy loss in stellar interiors. *The Astrophysical Journal, 296*, 197-203.

Munakata, H., Kohyama, Y., & Itoh, N. (1987). Neutrino-pair bremsstrahlung in dense stars. V-Partially degenerate electrons. *The Astrophysical Journal, 316*, 708-715.

Nolan, P., & Matteson, J. (1983). A feature in the X-ray spectrum of Cygnus X-1-A possible positron annihilation line. *The Astrophysical Journal, 265*, 389-392.

Ober, W., El Eid, M., & Fricke, K. (1983). Evolution of massive pregalactic stars-part two-nucleosynthesis in pair creation supernovae and pregalactic enrichment. *Astronomy and Astrophysics, 119*, 61-68.

Odrzywolek, A., Misiaszek, M., & Kutschera, M. (2004). Detection possibility of the pair-annihilation neutrinos from the neutrino-cooled pre-supernova star. *Astroparticle Physics, 21*(3), 303-313.

Odrzywolek, A., & Plewa, T. (2011). Probing thermonuclear supernova explosions with neutrinos. *Astronomy & Astrophysics, 529*, A156-A171.

Pantaleone, J. (1992). Neutrino oscillations at high densities. *Physics Letters B, 287*(1-3), 128-132.

Pantaleone, J. (1995). Neutrino flavor evolution near a supernova's core. *Physics Letters B, 342*(1-4), 250-256.

Paxton, B., Bildsten, L., Dotter, A., Herwig, F., Lesaffre, P., & Timmes, F. (2010). Modules for experiments in stellar astrophysics (MESA). *The Astrophysical Journal Supplement Series, 192*(1), 3-38.

Phillips, A. C. (2013). *The Physics of Stars* (Vol. 2nd ed). Hoboken: Wiley.

Pilla, R. P., & Shaham, J. (1997). Kinetics of electron-positron pair plasmas using an adaptive Monte Carlo method. *The Astrophysical Journal, 486*(2), 903-918.

Pols, O. (2011). Stellar Structure and Evolution. *Astronomical Institute Utrecht.*

Potekhin, A. Y., & Chabrier, G. (2010). Thermodynamic functions of dense plasmas: analytic approximations for astrophysical applications. *Contributions to Plasma Physics, 50*(1), 82-87.

Rakavy, G., & Shaviv, G. (1967). Instabilities in highly evolved stellar models. *The Astrophysical Journal, 148*, 803-816.

Rakavy, G., Shaviv, G., & Zinamon, Z. (1967). Carbon and oxygen burning stars and pre-supernova models. *The Astrophysical Journal, 150*, 131-162.

Renshaw, A., Abe, K., Hayato, Y., Iyogi, K., Kameda, J., Kishimoto, Y., . . . Nakano, Y. (2014). First indication of terrestrial matter effects on solar neutrino oscillation. *Physical Review Letters, 112*(9), 091805-1-6.

Seitenzahl, I. R., Herzog, M., Ruiter, A. J., Marquardt, K., Ohlmann, S. T., & Röpke, F. K. (2015). Neutrino and gravitational wave signal of a delayed-detonation model of type Ia supernovae. *Physical Review D, 92*(12), 124013-1-9.

Smith, N. (2014). Mass loss: its effect on the evolution and fate of high-mass stars. *Annual Review of Astronomy and Astrophysics, 52*, 487-528.

Smith, N., Li, W., Foley, R. J., Wheeler, J. C., Pooley, D., Chornock, R., . . . Bloom, J. S. (2007). SN 2006gy: discovery of the most luminous supernova ever recorded, powered by the death of an extremely massive star like η Carinae. *The Astrophysical Journal, 666*(2), 1116-1128.

Spergel, D. N., Piran, T., Loeb, A., Goodman, J., & Bahcall, J. N. (1987). A Simple-Model for Neutrino Cooling of the Large Magellanic Cloud Supernova. *Science, 237*(4821), 1471-1473.

Stringfellow, G., & Woosley, S. (1988). Origin and distribution of the elements, ed. G.J. Mathews: Singapore: World Scientific Publishing.

Sulaksono, A., & Simanjuntak, H. P. (1994). Stopping power of matter and energy losses of solar neutrinos. *Solar Physics, 151*(2), 205-212.

Svensson, R. (1982a). Electron-positron pair equilibria in relativistic plasmas. *The Astrophysical Journal, 258*, 335-348.

Svensson, R. (1982b). The pair annihilation process in relativistic plasmas. *The Astrophysical Journal, 258*, 321-334.

Svensson, R. (1987). Non-thermal pair production in Compact X-ray sources: first-order compton cascades in soft radiation fields. *Monthly Notices of the Royal Astronomical Society, 227*(2), 403-451.

Swesty, F. D. (1996). Thermodynamically consistent interpolation for equation of state tables. *Journal of Computational Physics, 127*(1), 118-127.

Takahashi, K., Yoshida, T., Umeda, H., Sumiyoshi, K., & Yamada, S. (2016). Exact and approximate expressions of energy generation rates and their impact on the explosion properties of pair instability supernovae. *Monthly Notices of the Royal Astronomical Society, 456*(2), 1320-1331.

Timmes, F., & Arnett, D. (1999). The accuracy, consistency, and speed of five equations of state for stellar hydrodynamics. *The Astrophysical Journal Supplement Series, 125*(1), 277-294.

Timmes, F. X., & Swesty, F. D. (2000). The accuracy, consistency, and speed of an electron-positron equation of state based on table interpolation of the helmholtz free energy. *The Astrophysical Journal Supplement Series, 126*(2), 501-516.

Vink, J. S., de Koter, A., & Lamers, H. (2001). Mass-loss predictions for O and B stars as a function of metallicity. *Astronomy & Astrophysics, 369*(2), 574-588.

Vink, J. S., Muijres, L., Anthonisse, B., de Koter, A., Gräfener, G., & Langer, N. (2011). Wind modelling of very massive stars up to 300 solar masses. *Astronomy & Astrophysics, 531*, A132-143.

Walborn, N. R., Morrell, N. I., Howarth, I. D., Crowther, P. A., Lennon, D. J., Massey, P.,…… Arias, J. I. (2004). A CNO dichotomy among O2 giant spectra in the magellanic clouds. *The Astrophysical Journal, 608*(2), 1028-1038.

Weaver, T., Zimmerman, G., & Woosley, S. (2017). KEPLER: General purpose 1D multizone hydrodynamics code. *Astrophysics Source Code Library.*

Whalen, D. J., Even, W., Frey, L. H., Smidt, J., Johnson, J. L., Lovekin, C. C., . . . Hungerford, A. L. (2013). Finding the first cosmic explosions. I. pair-instability supernovae. *Astrophysical Journal, 777*(2), 110-125.

Whalen, D. J., Smidt, J., Even, W., Woosley, S. E., Heger, A., Stiavelli, M.,……. Fryer, C. L. (2014a). Finding the first cosmic explosions. III. pulsational pair-instability supernovae. *Astrophysical Journal, 781*(2), 106-114.

Whalen, D. J., Smidt, J., Heger, A., Hirschi, R., Yusof, N., Even, W., . . . Joggerst, C. C. (2014b). Pair-instability supernovae in the local universe. *Astrophysical Journal, 797*(1), 9-25.

Wheeler, J. C. (1977). Final evolution of stars in the range 10 3–10 4 M$\odot$. *Astrophysics and Space Science, 50*(1), 125-131.

Wolf, R. (1974). Calculations of magnetospheric electric fields. *Magnetospheric Physics* (vol. 44, pp. 167-177). R. Reidel publishing company, Springer, Dordrecht-Holland.

Wolfenstein, L. (1978). Neutrino oscillations in matter. *Physical Review D, 17*(9), 2369-2374.

Wolfenstein, L. (1987). Effects of matter oscillations on supernova neutrino flux. *Physics Letters B, 194*(2), 197-199.

Woosley, S. (2017). Pulsational Pair-instability Supernovae. *The Astrophysical Journal, 836*(2), 244-280.

Woosley, S. E., & Heger, A. (2015). The Deaths of Very Massive Stars. In J. S. Vink (Ed.), *Very Massive Stars in the Local Universe* (pp. 199-225). Cham: Springer International Publishing.

Woosley, S. E., Heger, A., & Weaver, T. A. (2002). The evolution and explosion of massive stars. *Reviews of Modern Physics, 74*(4), 1015-1071.

Wright, W. P., Gilmer, M. S., Fröhlich, C., & Kneller, J. P. (2017a). Neutrino signal from pair-instability supernovae. *Physical Review D, 96*(10), 103008-1-22.

Wright, W. P., Kneller, J. P., Ohlmann, S. T., Röpke, F. K., Scholberg, K., & Seitenzahl, I. R. (2017b). Neutrinos from type Ia supernovae: The gravitationally confined detonation scenario. *Physical Review D, 95*(4), 043006-1-26.

Wright, W. P., Nagaraj, G., Kneller, J. P., Scholberg, K., & Seitenzahl, I. R. (2016). Neutrinos from type Ia supernovae: The deflagration-to-detonation transition scenario. *Physical Review D, 94*(2), 025026-1-25.

Wu, M.-R., Duan, H., & Qian, Y.-Z. (2016). Physics of neutrino flavor transformation through matter–neutrino resonances. *Physics Letters B, 752*, 89-94.

Yang, Y. (2018). *Neutrino flavor transformations in supernovae : the Role of Turbulence, Gravity, and Nonstandard Neutrino Self-interactions.* (Doctor of Philosophy), North Carolina State University, Raleigh, North Carolina, USA.

Yang, Y., & Kneller, J. P. (2018). Neutrino flavor transformation in supernovae as a probe for nonstandard neutrino-scalar interactions. *Physical Review D, 97*(10), 103018-1 -15.

Yorke, H. W. (2004). Theory of formation of massive stars via accretion. *Proceedings of the Symposium-International Astronomical Union*, 221, 141-154.

Yusof, N., Hirschi, R., Meynet, G., Crowther, P. A., Ekström, S., Frischknecht, U., . . . Schnurr, O. (2013). Evolution and fate of very massive stars. *Monthly Notices of the Royal Astronomical Society*, 433(2), 1114-1132.

Zwart, S. F. P., Pooley, D., & Lewin, W. H. (2002). A dozen colliding-wind X-ray binaries in the star cluster R136 in the 30 Doradus region. *The Astrophysical Journal, 574*(2), 762-770.